SURFACE REACTIONS AND ULTRAFAST DYNAMICS IN NANO- AND MICRO-SIZED MATERIALS

A Dissertation
Submitted to
the Temple University Graduate Board

In Partial Fulfillment
of the Requirements for the Degree
DOCTOR OF PHILOSOPHY

---

by
Bolei Xu
July 2016

Examining Committee Members:

Prof. Hai-lung Dai, Supervisor of Dissertation, Department of Chemistry
Prof. Robert J. Stanley, Committee Chair, Department of Chemistry
Prof. Robert J. Levis, Department of Chemistry
Prof. Yi Rao, Department of Chemistry
Prof. Shenqiang Ren, External Member, Department of Mechanical Engineering

ABSTRACT

In this dissertation, the laser spectroscopic methods, second harmonic generation (SHG) and ultrafast transient absorption, have been employed to study the reactions and dynamics in two different types of materials, namely, silver nanoparticles and micro-sized ultrathin crystalline oligoacenes. These two materials, although both are in small dimensions, represent two distinct types of systems with divergent characteristics: 1) systems in which interactions at the surface/interface are dominant, and 2) systems in which bulk interactions are dominant.

Silver nanoparticles are an important member of the class of noble metal nanoparticles, and possess unique optical and chemical properties due to their ultrafine size and high surface-to-volume ratio. Strong SHG signal has been observed from silver nanoparticles dispersed in aqueous colloidal solution, in which the SHG signal is enhanced due to a resonance with the localized surface plasmon of silver nanoparticles. Further experiments proved that the SHG signal predominantly originates from the particle surface, in full agreement with the intrinsically interface-sensitive properties of SHG. With the surface origin of the signal now well established, SHG can be used to probe the adsorption and reactions of thiol molecules at the nanoparticle surface *in situ* and in real time. It is experimentally demonstrated that the free energy change, activation energy, as well as adsorption density of the reactions of a variety of neutral and anionic thiols at the particle surface can be measured by means of SHG. The reaction mechanisms at the molecular level have been deduced, and the neutral vs anionic thiols are found to exhibit qualitatively

different reaction mechanisms that reflect the effect of their molecular interactions with the particle surface.

Oligoacenes, such as pentacene and hexacene, constitute a family of organic semiconductors that exhibit remarkable optoelectronic properties. In contrast to the nanoparticles in which surface interactions are dominant, as the sizes of materials become larger, the bulk characteristics become more deterministic. Therefore, polarized linear absorption and transient absorption spectroscopies have been applied to study the excitonic properties of crystalline pentacene and the mechanism of singlet fission in crystalline hexacene, respectively. The polarized absorption spectra of crystalline pentacene have been obtained by measuring transmitted light normal to the *ab* herringbone plane of micro-sized ultrathin single crystals. The significant deviations between the spectral line shapes polarized along the *b*-axis and orthogonal to the *b*-axis provide detailed information on the anisotropic mixing nature of the Frenkel/charge-transfer excitons responsible for the pronounced Davydov splitting between the lowest-energy singlet states. Additionally, both singlet and triplet Davydov splittings were also observed from the linear and transient absorption experiments in micrometer-sized ultrathin hexacene single crystals. A two-step process of anisotropic singlet fission was uncovered from the kinetic data, in which singlet fission at different rates were deduced along the *a*- and *b*-axes. Both the spectral and kinetic features indicate that singlet fission in crystalline hexacene is an anisotropic and charge-transfer mediated many-molecule process.

ACKNOWLEDGMENTS

There are many wonderful people to whom I would like to express my deepest appreciation.

First, my sincere gratitude is given to my advisor, Professor Hai-lung Dai for his invaluable support and constant guidance. He is not only a knowledgeable scientist, but also a great mentor. Under his supervision, I have received rigorous scientific training, and learnt the spirit of critical thinking, and more importantly, the philosophy of life.

I would love to give my great thanks to Dr. Yi Rao. Although only two years he has been instructing me, I have already learnt countless from him. His passion and eager for science as well as the spirits of creative thinking and hardworking have always inspired me in the research. I am so lucky to have such a great mentor.

I am really grateful to my committee members: Professor Robert J. Stanley, Professor Robert J. Levis, and Professor Shenqiang Ren for their priceless time and guidance. Their questions and comments have helped improve my research.

Special thanks goes to my collaborators, Professor Francis C. Spano and his student Nicholas Hestand. It is a great pleasure working with them for the pentacene project, from which I have deepened my understanding for the organic crystalline system. Dr. Dezheng Sun is another collaborator I would like to appreciate. He has helped me a lot for the development of the microscopic setups. I would not forget the days and nights we worked together in the laboratory, especially in the weekends.

I also like to acknowledge Dr. Wei Gan and Dr. Grazia Gonella for introducing me to the study of silver nanoparticles. Without their kind and patient help, it would not be

possible for me to finish my first project. I like also to appreciate other former and current Dai Group members, Dr. Min Zhang, Dr. Jianqiang Ma, Dr. Jia Zeng, and Dr. Michael Wilhelm, Dr. Jonathan Smith, Dr. Jun Han, Yajing Wu, Hui Fang, Yuhao Wu, Xia Li, Mohammad Sharifin. They have contributed their assistance and discussion in my projects, especially for Michael, who helped me a lot for the thesis.

Last but the most important, I would love to thank my family for their forever love and continued support in my life. Words cannot be enough to express my gratitude.

TABLE OF CONTENTS

Page

LIST OF TABLES

LIST OF FIGURES

CHAPTER 1

INTRODUCTION

1.1 Colloids

A colloidal suspension is a mixture of two or more phases that are finely separated by a well-defined interface, in which a dispersed phase (that is generally microscopic in size) is suspended in a dispersing phase.[1-4] Colloids cover a variety of systems in which each phase (dispersed or dispersing) can be gas, liquid, or solid as listed in Table 1.1.[3-4] As an ubiquitous system, colloids played an important role in human life long before the scientific definition emerged. In fact, colloidal pigments were used in stone age paintings, and are the earliest known example of the human usage of colloids. Nowadays, colloids are everywhere in our highly industrialized society, spanning from our daily life to the industrial productions.[1-4]

The birth of Colloid Chemistry dates back to the 19th century when Thomas Graham first coined the term "colloid", which stems from the Greek word for glue-like.[3-4] In a typical colloidal system, the sizes of the dispersed phase typically range from 1 nm to 1 μm.[1-4] Due to the high surface-to-volume ratio, a significant portion of the molecules or atoms lie within or close to the inhomogeneous region associated with the interface separating the dispersed and the dispersing phases. A high free energy excess, as well as high curvature, leads to thermodynamic instability of the interface, which in turn initiates various physical and chemical processes (e.g., surface adsorption of molecules) aiming to decrease the surface energy.[1-2] For this reason, Colloid Chemistry or, alternatively, Colloid

and Surface Science is often devoted to the investigation of the dispersed phase with particular attention to the interfacial phenomena.

Table 1.1 Typical colloidal systems in human life

Phases		
Dispersed	Dispersing	Systems
Liquid	Gas	Liquid aerosol (fog), spray
Liquid	Liquid	Emulsion (milk), butter, cream
Liquid	Solid	Solid emulsion (toothpaste)
Solid	Liquid	Sols, photography films, cement, coal slurry
Solid	Gas	Solid aerosol (dust, smoke)
Solid	Solid	Solids in plastics, pearl, stained glass, pigment
Gas	Solid	Solid foam (Insulating foam)

1.1.1 Nanoparticles in Colloids

Suspensions of nanoparticles with particle sizes ranging from 1 nm to 100 nm can be seen as a subset of colloidal systems.[5-6] Ever since the first scientific description of gold nanoparticles by Michael Faraday in the 19th century,[7-8] nanoparticles have attracted tremendous attention as they behave as an intermediate bridge between the bulk materials and the isolated atoms or molecules.[5] As a bulk material, both physical and chemical

properties should be constant regardless of the size. However, as the dimensions approach the nano-scale, size-dependent properties begin to emerge. A great number of materials exhibit unexpected physical and chemical properties as their sizes fall into the nanoparticle range.[8-12] In this dissertation, we focus on one particular type of nanoparticle composed of a noble metal, namely, silver nanoparticles.

There have been a large number of applications spanning in fields from optics to energy, catalysis, and biomedicine, which are based on the use of bare silver nanoparticles or particles with surfaces chemically modified with specific functional groups.[5-6, 9-14] The surface characteristics become more deterministic as the particle size decreases, and therefore, to realize the potential of silver nanoparticles requires a better understanding of the structure and the functionalization of the particle surface.

1.1.2 Study of Nanoparticles by Second Harmonic Generation

Despite the importance, studies of nanoparticles face a great challenge due to the lack of experimental techniques that are able to directly characterize the colloidal surface. As for a suspension of silver nanoparticles, the particle surface is deeply buried in the colloidal solution. Many powerful surface technologies, such as atomic force microscopy (AFM), x-ray scattering (XRS), or scanning tunneling microscopy (STM),[15] are not applicable for characterizing colloidal suspensions due to the presence of the solvent (i.e., dispersing phase). On the other hand, optical methods, such as ultraviolet-visible (UV-Vis) or infrared (IR) spectroscopy, although readily capable of penetrating the dispersing phase, suffer a distinct lack of surface sensitivity and selectivity, and are therefore likewise unable to probe the colloidal surface. This limitation stems from the fact that the signal in linear

optical spectroscopy is often dominated by contributions from molecules in the bulk phase. It is only in very rare cases that the linear spectral shifts resulting from atoms or molecules at the interface are sufficient to be differentiated.[16-18] This method, however, is not universal and is limited to a small number of systems.

For this reason, nonlinear optical spectroscopy, such as second harmonic generation (SHG), has been chosen in our interfacial studies of silver nanoparticles. Thanks to the modern development of ultrafast laser technology, nonlinear optical signal is sufficient enough to be observed in the laboratory. The intrinsically symmetric requirement of the nonlinear optics allows us to overcome the main obstacle of conventional linear optical techniques.[19-21] As a second-order nonlinear optical spectroscopy, SHG is diminished in centrosymmetric systems, and is all but unmeasurable. Conversely, the inhomogeneous interface between two colloidal phases, however, breaks the centrosymmetry, and produces the sole source of SHG in the system. In this sense, the measured SHG signal from a nanoparticle colloidal suspension directly reflects the response of the nanoparticle surface.

The unique optical properties of metal nanoparticles originate from the localized surface plasmon that is a collective oscillation of many electrons in the material.[6, 10] Linear optical behaviors of silver nanoparticles have long been discovered and explained by Mie theory, such as linear light absorption or scattering.[6, 10] As for second-order nonlinear optics, however, it was once believed that SHG was forbidden in small colloids, given the particles sizes are in close proximity to one another or smaller than the wavelength of the visible light.[22] It wasn't until 1996 when Ken Eisenthal's group reported the first observation of SHG from dye molecules that adsorbed at the surface of spherical polystyrene particles.[23] Further studies have demonstrated that SHG is accessible from

particles as small as tens of nanometers.[24-26] Therefore, it is expected that SHG from silver nanoparticles with 80 nm average diameter can be detectable, especially considering the fact that the localized surface plasmon is in resonance with the second harmonic wavelength of the most-commonly used Ti-Sapphire femtosecond laser.[10] A detailed discussion about the SHG signal from silver nanoparticles will be presented at Chapter 2. The effectiveness of SHG for the interfacial studies of the adsorption and reactions of various thiol molecules will also be demonstrated in the following chapters.

1.2 Organic Semiconductors

The unique properties of silver nanoparticles come from their ultrafine size and therefore high surface-to-volume ratio. On the other hand, we are also interested in characterizing materials in which the bulk contribution plays a more significant role, such as organic semiconductors. Organic semiconductors are a class of semiconductors that consist of π-conjugated organic molecules, such as oligoacenes and poly(thiophenes).[27-31] The history of the organic semiconductor can be traced back to the 1960s when the conductivities of organic crystals were studied.[32-35] Unlike the classical inorganic semiconductors such as silicon, in which atoms are held together with strong covalent or ionic bonds, organic semiconductors are composed of individual molecules that are weakly bounded together through van der Waals, hydrogen-bonding, or π-π interactions.[27-29, 31] In a molecular solid, the molecular orbitals are superimposed and form band structures analogous to the valence and conduction bands in inorganic semiconductor. The weak overlap between the wavefunctions, however, leads to much narrower bandwidths typically up to 200mV, in stark contrast to those on the order of electron volts that are typically

observed in inorganic semiconductors.[36] The narrow bandwidth indicates that the electron and hole are more localized, and therefore, the bands in organic semiconductor are often referred to as highest occupied molecular orbital (HOMO) and lowest unoccupied molecular orbital (LUMO) bands.[27, 31, 36]

Another fundamental difference between organic and inorganic semiconductors lies in the significance of excitons in their electronic and photovoltaic properties. An exciton is an electrically neutral quasi-particle in which an electron and a hole are bound together by the Coulombic force. Since organic semiconductor possesses smaller dielectric constant ($\varepsilon \approx 4$) than that of inorganic semiconductor ($\varepsilon > 11$), the Coulombic attraction is much less screened, leading to higher binding energies for excitons in organic semiconductors (0.1-1 eV) compared to that in inorganic semiconductors which are on the order of 0.01 eV.[28, 32, 36] Therefore, both charge excitation and charge transport exhibit strong excitonic properties in organic semiconductors.

Organic semiconductors possess a number of properties that are in some ways fundamentally different from that of inorganic semiconductors. Current and potential applications of organic semiconductors have formed an industry of billions of dollars, such as organic light-emitting diodes (OLED), organic field-effect transistor (OFET), and organic solar cells (OSC).[27-31, 36-37] To further realize the potential of organic semiconductors requires fundamental understanding of the physical, chemical, electronic, and photovoltaic properties. In this dissertation, we will discuss the excitonic property and the singlet fission mechanism from oligoacenes, a particular family of organic semiconductors.

1.2.1 Excitons in Organic Semiconductors

Excitons play an important role in the optoelectronic properties of organic semiconductors. Their significance can be revealed by the bandgap structure shown in Fig. 1.1A.[36] There are two types of bandgaps: the transport gap, E_t, and the optical gap, E_{opt}. In an organic semiconductor, the transport gap, E_t, is the energy to generate spatially well-separated electrons and holes, namely, the free carriers, while the optical gap, E_{opt}, is the energy required for the formation of bound electron-hole pairs, known as excitons. The energy difference between E_t and E_{opt} corresponds to the binding energy of excitons, E_b. As for organic semiconductors, due to the large value of E_b, the photo-induced carrier is excited to the exciton states, and thus the carrier mobility of organic semiconductors relies on the diffusion of neutral excitons.

There are two distinct kinds of excitons in organic semiconductors: i.e., Frenkel excitons and charge transfer (CT) excitons.[32, 36, 38] A Frenkel excition, named after Yakov Frenkel, is often found in materials with small dielectric constants. The Coulombic interaction between an electron and a hole is so strong that the exciton is small with a radius of about 10 Å. With respect to a molecular crystal, the exciton often resides within one single molecule. On the other hand, a CT exciton is sufficiently large that the electron and the hole occupy two adjacent molecules, respectively, in which one molecule appears to be cationic and the other anionic. A schematic example of a Frenkel exciton and a CT exciton is given in Fig. 1.1B based on the *ab* plane of a pentacene single crystal.

The existence of both Frenkel and CT excitons makes a great impact upon the optical properties of organic semiconductors. It is generally believed that the mixture of

Frenkel and CT excitons are responsible for the anisotropic optical features observed in crystalline oligoacenes.

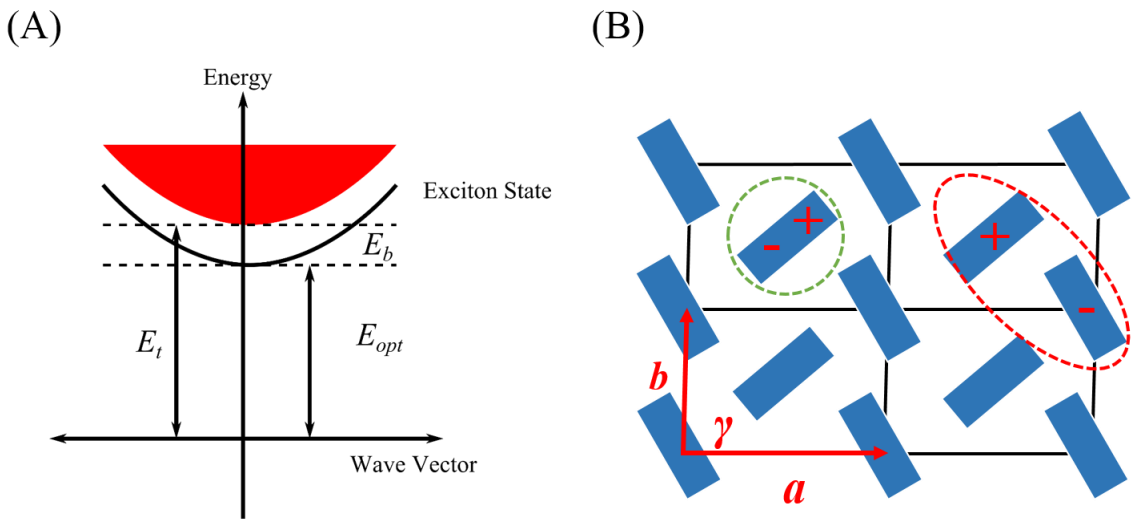

Figure 1.1 (A) Bandgaps of organic semiconductors. (B) Schematic representations of Frenkel (green dashed line) and CT (red dashed line) excitons in the *ab* plane of a pentancene single crystal.

1.2.2 Singlet Fission

Singlet fission is a phenomenon that was first discovered in 1965 from the photophysical study of crystalline anthrancene, a member of the oligoacene group.[37] Considerable efforts have been made in the study of the singlet fission phenomenon due to its extraordinary nature (see Fig. 1.2): one organic chromophore, after being photoexcited to an excited singlet state, interacts with an adjacent ground-state molecule and eventually converts both molecules into triplet states. Subsequently, singlet fission can have a quantum yield as high as 200%, and it is expected to be one of the potential methods to break the Shockley-Queisser limit for single p-n junctions in solar cells.[37, 39-41]

Unlike the ubiquitous intersystem crossing between singlet and triplet states within one single molecule, singlet fission has been observed only in a small number of organic systems that satisfy the spatial and energetic requirements:[37] 1) singlet fission only occurs in two neighboring molecules that are close enough to possess strong coupling, 2) favorable energetics ought to be encountered in which the singlet excitation energy $E(S_1)$ must exceed or at least be close to twice the triplet excitation energy $2E(T_1)$. For this reason, oligoacenes, such as tetracene, pentacene, and hexacene, have been intensively studied as they give rise to high efficiency singlet fission.[37] Fig. 1.3 illustrates the energy levels of tetracene, pentacene, and hexacene, where $E(S_1)$ of tetracene is slightly lower than $2E(T_1)$, while $E(S_1)$ of the others exceed $2E(T_1)$.[37, 42]

At present, due to the lack of knowledge regarding the singlet fission mechanism, the proposed use of singlet fission is still at the stage of fundamental research. Thus, a deeper understanding of singlet fission is required for not only the fundamental science, but also practical applications of organic semiconductors.

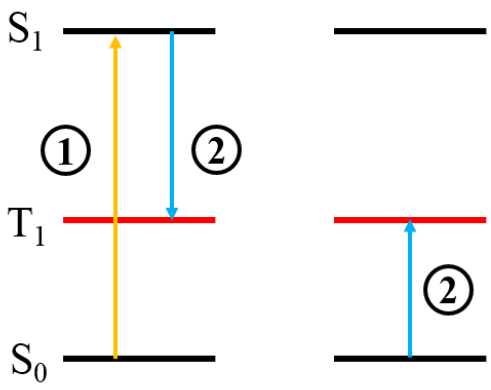

Figure 1.2 Schematic of singlet fission: (1) photoexcitation of one molecule to lowest excited singlet state, S_1, (2) singlet fission between the two adjacent molecules, generating two triplet states, T_1.

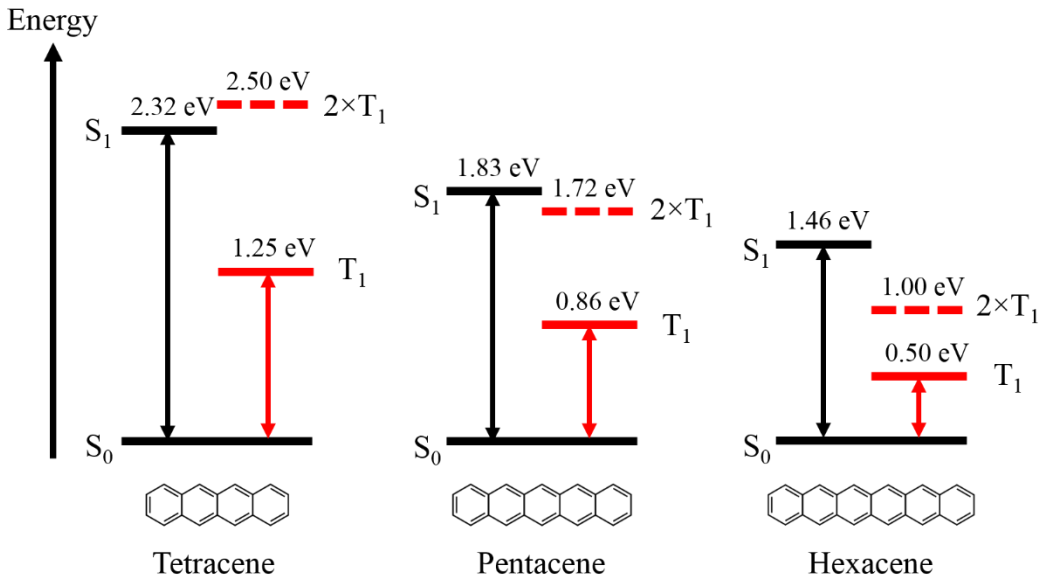

Figure 1.3 Energy levels of oligoacene series. From left to right: tetracene, pentacene, and hexacene.

1.2.3 Crystalline Oligoacenes

Organic semiconductors in the form of single crystal have been central in our studies of the excitonic properties and the mechanism of singlet fission. Despite the weak bonding between organic molecules, oligoacenes, such as pentacene and hexacene, are still able to crystallize into a herringbone structure.[28, 32] The crystal structure of pentacene is displayed in Fig. 1.4. In the *ab* plane, the inequivalent molecules at (0,0) and (1/2, 1/2) adopt an edge-to-face arrangement to minimize π-orbital repulsion. The special molecular ordering of the oligoacene single crystal, in return, gives rise to some important features, such as the anisotropic excitonic properties and anisotropic singlet fission, providing us a great opportunity to uncover the sophisticated mechanism of singlet fission.

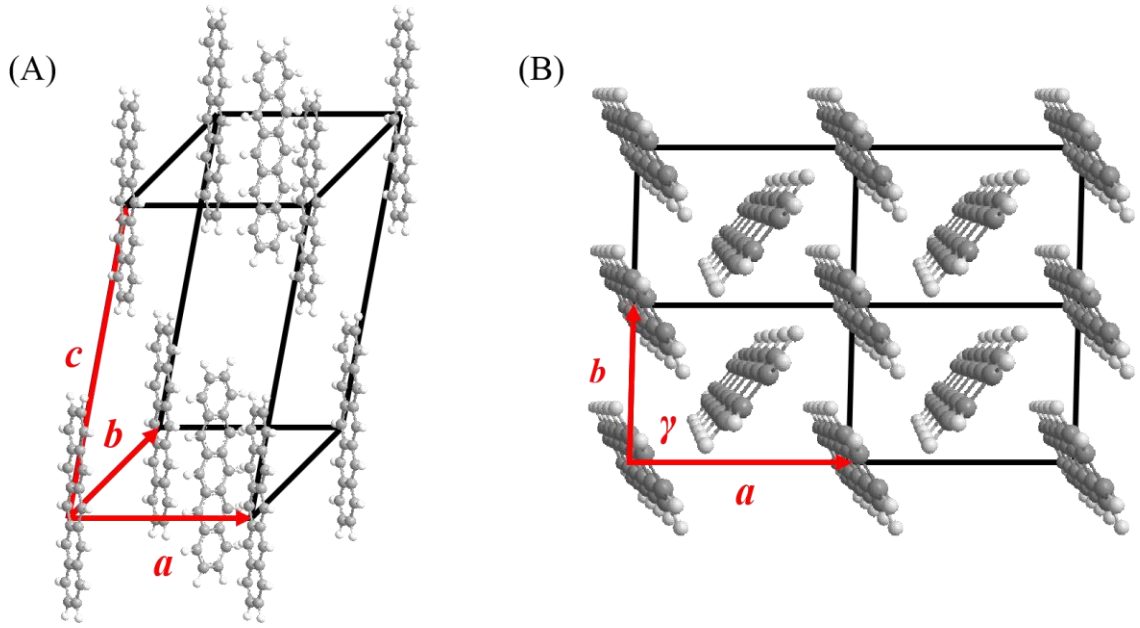

Figure 1.4 (A) Triclinic crystal structure of pentacene and (B) the *ab* herringbone plane of pentacene.

1.2.4 Study of Micro-Sized Ultrathin Oligoacene Single Crystals

Compared to nanoparticles for which the surface contribution is deterministic, studies of crystalline oligoacenes often focus on the bulk contribution as the percentage of molecules at the surface is comparatively insignificant. Therefore, odd-order optical spectroscopies, such as linear absorption and transient absorption techniques, have been applied in our studies: linear absorption provides us information associated with the steady state of excitons in the single crystal, and transient absorption enables us to study the ultrafast evolution of the singlet and triplet excitons in the singlet fission process.

Although both linear and transient absorption spectroscopies have been well-developed, a relatively small number of optical spectroscopic studies have been reported with respect to crystalline oligoacenes.[43-46] A direct optical measurement in the transmission geometry still remains an experimental challenge due to the high absorption coefficients of pentacene and hexacene. The optimal thickness of a single crystal for the transmitted absorption experiment is about 100-500nm, and therefore micrometer-sized ultrathin single crystals have to be prepared. Conventional setups for linear and transient absorptions are designed for large samples, usually with dimensions on the millimeter-scale. Therefore, we have built a linear and transient absorption spectrometer coupled with an optical microscope to study micrometer-sized ultrathin single crystals.

1.3 Scope and Objective of the Dissertation

There are two major aspects in this dissertation. In the first part, from Chapter 2 to Chapter 4, we report strong SHG signal observed from silver nanoparticles in colloidal solution. The surface origin of the SHG signal was experimentally demonstrated, which, in return, allows us to exploit the adsorption and reactions of neutral and anionic thiol molecules on silver nanoparticles. The second part includes chapter 5 and 6, where microscopic linear and transient absorption have been used to study the micrometer-sized ultrathin pentacene and hexacene single crystals, respectively. The excitonic compositions of a pentacene single crystal as well as the singlet fission mechanism in crystalline hexacene are discussed.

In detail, Chapter 2 first presents a brief theoretical treatment of SHG from the planar interface as well as the nanoparticle surface. It provides a prediction that SHG signal from silver nanoparticles with an average diameter of 80 nm can be observed in a large scattering angle, which was later proved by an angle-resolved experiment. Strong SHG signal has been observed using a Ti-Sapphire laser oscillator. To investigate the origin of the SHG signal, ethanethiol was introduced in silver colloids to quench the surface second-order susceptibility through the silver-sulfur covalent bonding. As ethanthiols saturated the particle surface, a majority of the SHG signal was attenuated, proving that the surface contribution dominates the total SHG signal.

Given the facts that SHG signal mainly originates from the surface of silver nanoparticles and the silver-sulfur covalent bonding quenches SHG signal, SHG can be applied as an optical probe to monitor the adsorption and reactions of thiol molecules on silver nanoparticles. In Chapter 3, the adsorption of a neutral thiol molecule i.e., 1,2-

benzenedithiol, was exploited by performing both concentration-dependent and temperature-controlled time-resolved experiments. The adsorption was found to follow the Langmuir process, enabling the acquisition of the maximum number density of the bonding sites as well as the Gibbs free energy change from the adsorption isotherm. In addition, the activation energy has also been obtained based on the Arrhenius equation. The magnitude of the deduced activation energy indicates that the adsorption is not a diffusion-limited process. Instead, chemical reaction between the thiol molecule and silver atoms is rate-determining in the adsorption process.

To examine how charge affects the molecular adsorption onto silver nanoparticles, anionic thiol molecule with a sulfonate endgroup i.e., 3-mercaptopropanesulfonate (MPS), was used in Chapter 4. The chemisorption of an anionic thiol was found to occur in two different regimes of concentration, in contrast to the neutral thiols which display only monotonic concentration dependence. This two-step adsorption is primarily a result of the charge-charge repulsion among the anionic thiols adsorbed on the surface: at low MPS concentration, a low coverage of the anionic thiol possess negligible molecular interaction, while, as the surface coverage increases, the inter-thiol repulsion builds up to obstruct further adsorption. The activation energy acquired from the temperature-dependent experiment agrees with such a two-step model: the activation energy at the first step is close to that in the neutral thiol adsorption, while the second step has a much higher activation energy containing both the silver-sulfur chemical bonding and the intermolecular repulsions.

In Chapter 5, we present polarized linear absorption spectra of the micro-sized ultrathin crystalline pentacene utilizing direct transmission measurements. Compared to

the unpolarized absorption spectrum of monomer pentacene in solution, the polarized spectra of crystalline pentacene showed dramatic spectral changes upon crystallization. In addition, significant deviations were also observed between the spectral lineshapes polarized parallel and perpendicular to the crystallographic short *b*-axis, such as a pronounced Davydov splitting (≈1000 cm^{-1}). Collaborating with Dr. Spano and his coworkers, the anisotropic linear absorption spectra were theoretically analyzed using a Holstein-like Hamiltonian based on both Frenkel and CT excitons. The results established that the different Frenkel/CT mixing compositions are the cause of the anisotropic property of the low-lying excitations.

Chapter 6 discusses the direct observations of the anisotropic singlet fission in hexacene single crystals. Both the singlet and triplet Davydov splittings have been obtained, suggesting strong CT characters in hexacene. Additionally, polarized kinetic experiments also indicate that singlet fission in crystalline hexacene is a two-step process, different from the traditional one-step dominant picture. The anisotropic rates of singlet fission along two crystallographic axes present strong dependence on the intermolecular packing.

1.4 Bibliography

1. Colloid and Surface Chemistry. 1st ed. ed.; Shchukin, E. D., Ed. Elsevier: Amsterdam ;, 2001.
2. Birdi, K. S., Surface and Colloid Chemistry : Principles and Applications. CRC Press: Boca Raton :, 2010.
3. Evans, D. F., The Colloidal Domain : Where Physics, Chemistry, Biology, and Technology Meet. Wennerström, H. k., Ed. VCH Publishers: New York, NY :, 1994.
4. Everett, D. H., Basic Principles of Colloid Science. Royal Society of Chemistry: London :, 1988.
5. Nanoparticle Technology Handbook. 2nd ed. ed.; Hosokawa, M., Ed. Elsevier: Amsterdam ;, 2012.
6. Alarcon, E. I., Silver Nanoparticle Applications: In the Fabrication and Design of Medical and Biosensing Devices. Griffith, M.; Udekwu, K. I., Eds.
7. Nanoparticles : Building Blocks for Nanotechnology. Rotello, V. M., Ed. Kluwer Academic/Plenum Publishers: New York :, 2004.
8. Daniel, M.-C.; Astruc, D., Gold Nanoparticles: Assembly, Supramolecular Chemistry, Quantum-Size-Related Properties, and Applications toward Biology, Catalysis, and Nanotechnology. *Chem. Rev.* **2003,** *104* (1), 293-346.
9. Halas, N. J.; Lal, S.; Chang, W.-S.; Link, S.; Nordlander, P., Plasmons in Strongly Coupled Metallic Nanostructures. *Chem. Rev.* **2011,** *111* (6), 3913-3961.
10. Mayer, K. M.; Hafner, J. H., Localized Surface Plasmon Resonance Sensors. *Chem. Rev.* **2011,** *111* (6), 3828-3857.

11. Rosi, N. L.; Mirkin, C. A., Nanostructures in Biodiagnostics. *Chem. Rev.* **2005,** *105* (4), 1547-1562.

12. Rycenga, M.; Cobley, C. M.; Zeng, J.; Li, W.; Moran, C. H.; Zhang, Q.; Qin, D.; Xia, Y., Controlling the Synthesis and Assembly of Silver Nanostructures for Plasmonic Applications. *Chem. Rev.* **2011,** *111* (6), 3669-3712.

13. Eckhardt, S.; Brunetto, P. S.; Gagnon, J.; Priebe, M.; Giese, B.; Fromm, K. M., Nanobio Silver: Its Interactions with Peptides and Bacteria, and Its Uses in Medicine. *Chem. Rev.* **2013,** *113* (7), 4708-4754.

14. Ulman, A., Formation and Structure of Self-Assembled Monolayers. *Chem. Rev.* **1996,** *96* (4), 1533-1554.

15. Somorjai, G. A., Chemistry in Two Dimensions : Surfaces. Cornell University Press: Ithaca :, 1981.

16. Warr, G. G.; Evans, D. F., Spectroscopic Determination of the Effective Dielectric-Constant of Micelle Water Interfaces between 15 and 85-Degrees-C. *Langmuir* **1988,** *4* (1), 217-224.

17. Zachariasse, K. A.; Vanphuc, N.; Kozankiewicz, B., Investigation of Micelles, Micro-Emulsions, and Phospholipid-Bilayers with the Pyridinium N-Phenolbetaine Et(30), a Polarity Probe for Aqueous Interfaces. *J. Phys. Chem.* **1981,** *85* (18), 2676-2683.

18. Zhu, D. M.; Wu, X.; Schelly, Z. A., Reverse Micelles and Water in Oil Microemulsions of Triton X-100 in Mixed-Solvents of Benzene and N-Hexane - Dynamic Light-Scattering and Turbidity Studies. *Langmuir* **1992,** *8* (6), 1538-1540.

19. Shen, Y. R., The Principles of Nonlinear Optics. Wiley: New York :, 1984.

20. Shen, Y. R., Optical 2nd Harmonic-Generation at Interfaces. *Annu. Rev. Phys. Chem.* **1989,** *40*, 327-350.

21. Boyd, R. W., Nonlinear Optics. 3rd ed. ed.; Academic Press: Burlington, MA :, 2008.

22. Eisenthal, K. B., Second Harmonic Spectroscopy of Aqueous Nano- and Microparticle Interfaces. *Chem. Rev.* **2006,** *106* (4), 1462-1477.

23. Wang, H.; Yan, E. C. Y.; Borguet, E.; Eisenthal, K. B., Second Harmonic Generation from the Surface of Centrosymmetric Particles in Bulk Solution. *Chem. Phys. Lett.* **1996,** *259* (1–2), 15-20.

24. Jen, S.-H.; Gonella, G.; Dai, H.-L., The Effect of Particle Size in Second Harmonic Generation from the Surface of Spherical Colloidal Particles. I: Experimental Observations†. *J. Phys. Chem. A* **2009,** *113* (16), 4758-4762.

25. Jen, S.-H.; Dai, H.-L., Probing Molecules Adsorbed at the Surface of Nanometer Colloidal Particles by Optical Second-Harmonic Generation. *J. Phys. Chem. B* **2006,** *110* (46), 23000-23003.

26. Jen, S.-H.; Dai, H.-L.; Gonella, G., The Effect of Particle Size in Second Harmonic Generation from the Surface of Spherical Colloidal Particles. Ii: The Nonlinear Rayleigh−Gans−Debye Model. *J. Phys. Chem. C* **2010,** *114* (10), 4302-4308.

27. Coropceanu, V.; Cornil, J.; da Silva, D. A.; Olivier, Y.; Silbey, R.; Bredas, J. L., Charge Transport in Organic Semiconductors. *Chem. Rev.* **2007,** *107* (4), 926-952.

28. Hains, A. W.; Liang, Z. Q.; Woodhouse, M. A.; Gregg, B. A., Molecular Semiconductors in Organic Photovoltaic Cells. *Chem. Rev.* **2010,** *110* (11), 6689-6735.

29. Murphy, A. R.; Frechet, J. M. J., Organic Semiconducting Oligomers for Use in Thin Film Transistors. *Chem. Rev.* **2007,** *107* (4), 1066-1096.

30. Samuel, I. D. W.; Turnbull, G. A., Organic Semiconductor Lasers. *Chem. Rev.* **2007,** *107* (4), 1272-1295.

31. Shirota, Y.; Kageyama, H., Charge Carrier Transporting Molecular Materials and Their Applications in Devices. *Chem. Rev.* **2007,** *107* (4), 953-1010.

32. Kohler, A., Electronic Processes in Organic Semiconductors : An Introduction. Bässler, H., Ed.

33. Helfrich, W.; Schneide.Wg, Transients of Volume-Controlled Current and of Recombination Radiation in Anthracene. *J. Chem. Phys.* **1966,** *44* (8), 2902.

34. Helfrich, W.; Schneide.Wg, Recombination Radiation in Anthracene Crystals. *Phys. Rev. Lett.* **1965,** *14* (7), 229.

35. Pope, M.; Magnante, P.; Kallmann, H. P., Electroluminescence in Organic Crystals. *J. Chem. Phys.* **1963,** *38* (8), 2042.

36. Zahn, D. R. T.; Gavrila, G. N.; Salvan, G., Electronic and Vibrational Spectroscopies Applied to Organic/Inorganic Interfaces. *Chem. Rev.* **2007,** *107* (4), 1161-1232.

37. Smith, M. B.; Michl, J., Singlet Fission. *Chem. Rev.* **2010,** *110* (11), 6891-6936.

38. Spano, F. C., Excitons in Conjugated Oligomer Aggregates, Films, and Crystals. *Annu. Rev. Phys. Chem.* **2006,** *57*, 217-243.

39. Shockley, W.; Queisser, H. J., Detailed Balance Limit of Efficiency of P-N Junction Solar Cells. *J. Appl. Phys.* **1961,** *32* (3), 510.

40. Congreve, D. N.; Lee, J. Y.; Thompson, N. J.; Hontz, E.; Yost, S. R.; Reusswig, P. D.; Bahlke, M. E.; Reineke, S.; Van Voorhis, T.; Baldo, M. A., External Quantum Efficiency above 100% in a Singlet-Exciton-Fission-Based Organic Photovoltaic Cell. *Science* **2013,** *340* (6130), 334-337.

41. Smith, M. B.; Michl, J., Recent Advances in Singlet Fission. *Annu. Rev. Phys. Chem.* **2013,** *64*, 361-386.

42. Chernikov, A.; Yaffe, O.; Kumar, B.; Zhong, Y.; Nuckolls, C.; Heinz, T. F., Spectroscopic Study of Anisotropic Excitons in Single Crystal Hexacene. *J. Phys. Chem. Lett.* **2014,** *5* (21), 3632-3635.

43. Prikhotk.Af; Tsikora, L. I., Spectral Investigations of Pentacene. *Opt. Spectrosc.* **1968,** *25* (3), 242.

44. Zanker, V.; Preuss, J., Microspectrometrical Measurements on Single Crystals of Tetracene and Pentacene in Depedence of Thickness and Temperature. *Z. Angew. Physik* **1969,** *27* (6), 363.

45. Faltermeier, D.; Gompf, B.; Dressel, M.; Tripathi, A. K.; Pflaum, J., Optical Properties of Pentacene Thin Films and Single Crystals. *Phys. Rev. B* **2006,** *74* (12).

46. Dressel, M.; Gompf, B.; Faltermeier, D.; Tripathi, A. K.; Pflaum, J.; Schubert, M., Kramers-Kronig-Consistent Optical Functions of Anisotropic Crystals: Generalized Spectroscopic Ellipsometry on Pentacene. *Opt. Express* **2008,** *16* (24), 19770-19778.

CHAPTER 2

SECOND HARMONIC GENERATION FROM THE SURFACE OF SILVER NANOPARTICLES

2.1 Introduction

Colloids containing particles with sizes ranging from micrometers to nanometers are of great current interest. Many of the unique properties of colloids originate from the high ratio between the number of atoms at the surface and that in the bulk. As the particles become smaller, the surface characteristics become more deterministic of the colloidal properties. Among the various colloidal particles, noble metal nanoparticles, such as those made of gold and silver, have been the focus of intensive studies. There have been a large number of applications spanning in fields from optics to energy, catalysis, and biomedicine that are based on the use of noble metal nanoparticles.[1-5] Consequently, the ability to characterize the structure and functionalization of the particle surface is crucial in the field of noble metal nanoparticles.

Despite the great desire for sensing nanoparticles, a lack of effective tool limits the *in situ* study of colloidal particles surface. Part of the difficulty comes from the fact that, in a great deal of applications, the surface/interfaces of particles are deeply buried in the colloidal medium. Depositing the particles out of colloidal solution may cause loss of surface functionality and therefore is not suitable for direct surface studies. In this sense, optical methods are often chosen for their advantage of making little alteration to the system.[6-9] However, conventional optical techniques, such as UV-Vis linear absorption, although being proved effective in a number of colloidal researches, provide little

information about the particle surface, due to the fact that the bulk contribution dominates the signal. Hence, second harmonic generation (SHG), a particular second-order nonlinear optical technique, has emerged as a versatile tool for interfacial/surface studies.

As a nonlinear optical phenomenon, SHG was first discovered by Franken *et al.* in 1961, shortly after the invention of the first working laser by Maiman in 1960, marking the start of nonlinear optics fields.[10-11] The nature that SHG converts two photons with frequency ω into one photon with second-harmonic (SH) frequency 2ω,[10, 12] makes it extremely useful in science and engineer areas and therefore inspires great efforts on the experimental and theoretical investigations of SHG phenomenon. Among a series of experiments, SHG exhibited unique sensitivity and selectivity to the symmetry that have drawn considerable attention from scientists interested at the surface field. It has been demonstrated experimentally and theoretically that SHG is forbidden in the media with inversion symmetry.[11, 13-17] Attributed to the symmetry-break nature of interfaces, SHG signal was found only originated from the interface as the boundary between two inversion symmetric media.[10, 12] Therefore, SHG has great potential in the *in situ* study of interface/surface. Indeed, ever since the pioneer work by Shen and his coworkers,[18-20] SHG has been developed as an effective tool for the characterization of planar surfaces, such as air/water interface and metallic surface.

SHG's intrinsic, symmetry-based surface sensitivity is not limited to planar interfaces. The effectiveness of SHG for detecting molecules at surface of micrometer-size particles was first demonstrated by Eisenthal and his coworkers.[21] Our group, along with others,[22-25] has extended the application of SHG for probing the surface of nanometer-size particles in colloids. Compared with the planar interfaces, SHG signal from the particle

surfaces interfere with each other and hence scatter into the space, leading to the phenomenon as second harmonic scattering (SHS), a particular kind of nonlinear light scattering. Previous studies have been focusing on the surface of polymer particles, liposomes and *E.coli* systems.[22-27] As the particles themselves are not resonant with the fundamental or the second harmonic (SH) light, they often require an addition of SHG-active dyes, such as malachite green.[22-27] Although a system with center of inversion symmetry on a scale much smaller than the optical coherence length does not facilitate dipole allowed SHG, its finite size still enables the phase matching condition for SHS to be satisfied at large scattering angles.[23-24, 28-29] In the case of silver nanoparticles (Ag NPs), due to the localized surface plasmon that is in resonance with the SH light, the surface layer should have a large enough hyperpolarizability to allow for direct detection of surface generated SH signal even in the absence of an adsorbed layer of hyperpolarizable molecules. Therefore, SHS can be developed for probing the surface of noble metallic particles buried deeply in a condensed medium.

In this chapter, we present an experimental observation of strong SHS signal from Ag NPs with 80nm diameter in average. A direct experimental evident is provided to prove that SH signal mainly originates from the surface of Ag NPs. In addition, angular scattering patterns of Ag NPs have been measured in angle-resolved SHS experiments in various polarization combinations. The results not only support our prediction that SH signal emits at large scattering angles, but also agree with the theoretical calculation based on nonlinear Mie theory (NLM).

2.2 Second-Order Nonlinear Spectroscopy: Second Harmonic Generation

To facilitate SHS as an effective tool for sensing nanoparticles, fundamental understanding of the second-order nonlinear optical process is necessary. Optics is the study of phenomena that occur as a consequence of the interaction between material systems and the applied optical field. The modification of the optical properties by the presence of light, generally, can be described by the polarization, $\tilde{P}(t)$, as a power series in the applied optical field, $\tilde{E}(t)$, shown in Eq. 2.1,[10]

$$\begin{aligned}\tilde{P}(t) &= \varepsilon[\chi^{(1)}\tilde{E}(t) + \chi^{(2)}\tilde{E}^2(t) + \chi^{(3)}\tilde{E}^3(t) + \cdots] \\ &= \tilde{P}^{(1)}(t) + \tilde{P}^{(2)}(t) + \tilde{P}^{(3)}(t) + \cdots = \tilde{P}^{L}(t) + \tilde{P}^{NL}(t)\end{aligned} \tag{2.1}$$

where ε is the permittivity, $\chi^{(1)}$, $\chi^{(2)}$ and $\chi^{(3)}$ are the first, second, and third order optical susceptibilities, respectively. For simplicity, both the polarization, $\tilde{P}(t)$, and the optical field, $\tilde{E}(t)$, are taken to be scalar quantities. The tilde symbol, ~, means that they are fast oscillating quantities.

In the case of linear optics, only the first linear term, $\tilde{P}^{L}(t) = \varepsilon\chi^{(1)}\tilde{E}(t)$, is considered. However, when the applied optical field is sufficiently intense, the high order terms, $\tilde{P}^{NL}(t) = \varepsilon[\chi^{(2)}\tilde{E}^2(t) + \chi^{(3)}\tilde{E}^3(t) + \cdots]$, become non-negligible. Hence, nonlinear spectroscopy differs from linear spectroscopy in that the response of a material to light depends on the strength of the applied optical field in a nonlinear manner.

2.2.1 General Theory of Second Harmonic Generation

In this chapter, we focus on a special case of the second-order nonlinear spectroscopy, second harmonic generation (SHG). An example of SHG is illustrated

schematically in Fig. 2.1A. Here, a laser beam with frequency ω, is incident upon a homogeneous material with the second-order susceptibility $\chi^{(2)}$. The second-order polarization, $\tilde{P}^{(2)}$, subsequently, results in the generation of radiation at the SH frequency 2ω.

$$\tilde{P}^{(2)} = \tilde{P}_{2\omega} = \varepsilon_0 \chi^{(2)} \tilde{E}_\omega \tilde{E}_\omega \tag{2.2}$$

To acquire a complete description of the SH radiation, we need to solve the Maxwell's equations. Assuming there is no free charge and free current, the Maxwell's equations lead to the wave equation,[10, 12, 30]

$$\nabla^2 \tilde{\boldsymbol{E}} - \frac{\varepsilon^{(1)}}{c^2} \frac{\partial^2}{\partial t^2} \tilde{\boldsymbol{E}} = \frac{1}{\varepsilon_0 c^2} \frac{\partial^2}{\partial t^2} \tilde{\boldsymbol{P}}^{(2)} \tag{2.3}$$

with $\varepsilon^{(1)}$ the relative permittivity. An analytical solution can be obtained at the condition that ignores the depletion of the fundamental light:[10, 12, 30]

$$I_{2\omega} = \frac{8 |\chi_{eff}^{(2)}|^2 \omega^2 I_\omega^2}{n_\omega^2 n_{2\omega} \varepsilon_0 c^2} L^2 \mathrm{sinc}^2\left(\frac{\Delta k \cdot L}{2}\right) \tag{2.4}$$

where $\chi_{eff}^{(2)}$ is the effective second-order nonlinear susceptibility, $n_{2\omega}$ and n_ω are the refractive indices of the material at the frequencies of 2ω and ω, L is the optical length, I_ω is the intensity of the fundamental light, and Δk is the difference of wave vectors between the fundamental and the SH light, i.e. $\Delta k = k_{2\omega} - 2k_\omega$.

In Eq. 2.4, there are two critical parameters that determine the SH signal, namely, $\chi_{eff}^{(2)}$ and Δk. $\chi_{eff}^{(2)}$ is the intrinsic nonlinear property of the material. In a two-level system between the ground state and the excited state (Fig. 2.1B), the second-order susceptibility can be expressed as,[10]

$$\chi^{(2)} = \frac{< g|\mu|i >< i|\mu|e >< e|\mu|g >}{[(\omega_{gi} - \omega) - i\gamma_{ig}][(\omega_{ge} - 2\omega) - i\gamma_{eg}]} \tag{2.5}$$

where $< g|\mu|i >$ represents the transition dipole moment from the ground state g to the intermediate state i, ω_{gi} is the corresponding frequency of the transition, γ_{ig} is the linewidth for the transition, and etc. Since the SH intensity is proportional to the square of the second-order susceptibility $\chi^{(2)}$, Eq. 2.5 shows that the magnitude of $\chi^{(2)}$, and consequently the SH intensity, $I_{2\omega}$, can be greatly enhanced when the fundamental or/and the SH frequency is in resonance with any of the transitions. As for Δk, it appears that the SH signal becomes larger as Δk is closer to 0. This is called phase-matching condition.

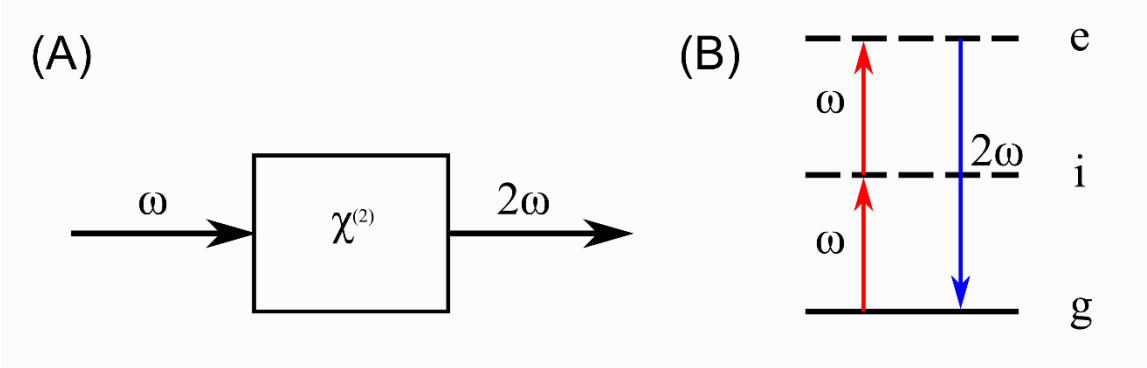

Figure 2.1 (A) Schematic of SHG from an isotropic material. (B) Two-level system for SHG.

2.2.2 Second Harmonic Generation from Planar Interface

SHG, ever since its discovery, has been widely applied in a great number of areas for research and industry. One of the areas we are interested in is the study of interfacial phenomena.

The advantage of SHG in interfacial research results from its intrinsic property related to inversion symmetry. For isotropic media, an inversion symmetry operation changes all vectors' signs. Therefore, the second-order polarization, $\tilde{P}^{(2)}$, must satisfy Eq. 2.6,

$$-\tilde{P}^{(2)} = \varepsilon_0 \chi^{(2)}(-\tilde{E}_\omega)(-\tilde{E}_\omega) \tag{2.6}$$

Fulfilling both Eq. 2.2 and Eq. 2.6 requires $\chi^{(2)} = -\chi^{(2)}$, which is impossible unless $\chi^{(2)} = 0$. Therefore, as an even-order nonlinear process, SHG must vanish in media with inversion symmetry. On the other hand, interfaces between two media with inversion symmetry can be seen as a boundary layer in that the inversion symmetry is broken. The fact that SHG is forbidden from the bulks indicates that SHG can only arise from the interfacial layer, making SHG an intrinsically interfacial technique.

To investigate SHG from the interface, we start with the planar interface model as displayed in Fig. 2.2. Complete treatment of SHG from planar interface can be found in literatures.[10, 12, 16] In brief, the second-order polarization $\tilde{P}^{(2)}$ generated from the interface is governed by the Maxwell's equations with new boundary conditions.[16] Seeking the solution must take into account the vector nature of the polarization and the optical field. Therefore, the second-order susceptibility should be treated as a third-rank tensor,[10, 12] and the second-order polarization can be expressed as,

$$P_i^{(2)} = \sum_{j,k} \chi_{ijk}^{(2)} E_\omega^j E_\omega^k \tag{2.7}$$

with *i, j, k* the three normal coordinates of laboratory system (*i, j, k*)=(*x, y, z*), respectively.

The boundary conditions[16] for Fig. 2.2 include

$$\begin{cases} \Delta B_x = -4\pi i \dfrac{2\omega}{c} P_y \\ \Delta B_y = 4\pi i \dfrac{2\omega}{c} P_x \\ \Delta B_z = 0 \\ \Delta E_x = -\dfrac{4\pi}{\varepsilon'} \dfrac{\partial}{\partial x} P_y \\ \Delta E_y = -\dfrac{4\pi}{\varepsilon'} \dfrac{\partial}{\partial y} P_z \\ \Delta D_z = -4\pi \left(\dfrac{\partial}{\partial x} P_x + \dfrac{\partial}{\partial y} P_y \right) \end{cases} \tag{2.8}$$

where ε' is the relative permittivity from the interface, and ΔQ represents the difference of quantity Q across the interface $\Delta Q = Q(z = 0^+) - Q(z = 0^-)$, for Q=B_x, B_y. B_z, E_x, E_y, D_z.

Solving the Maxwell's equations leads to the modification of $\chi_{eff}^{(2)}$ in Eq. 2.7 that,[16]

$$\chi_{eff}^{(2)} = [\hat{e}(2\omega) \cdot \vec{L}(2\omega)] \cdot \chi_{ijk}^{(2)} : [\vec{L}(\omega) \cdot \hat{e}(\omega)][\vec{L}(\omega) \cdot \hat{e}(\omega)] \tag{2.9}$$

with $\hat{e}$ the unit electric field vector for the fundamental and SH light, and $\vec{L}$ the Fresnel coefficients as functions of refractive indices and the angles of the fundamental and SH light.

As a third-rank tensor, the second-order nonlinear susceptibility $\chi_{ijk}^{(2)}$ has 3×3×3=27 elements. The number can been reduced given the symmetry of the system.[31-32]

For an isotropic interface, although the inversion symmetry is broken along the *z*-axis, other symmetries are still preserved. According to the rotational symmetry around the *z*-axis, the *x* and *y*-axis are indistinguishable, and hence many elements of $\chi_{ijk}^{(2)}$ vanish except for 7 elements with only 3 independent values: $\chi_{zzz}^{(2)}$, $\chi_{zxx}^{(2)} = \chi_{zyy}^{(2)}$, $\chi_{xzx}^{(2)} = \chi_{yzy}^{(2)} = \chi_{xxz}^{(2)} = \chi_{yyz}^{(2)}$.[32]

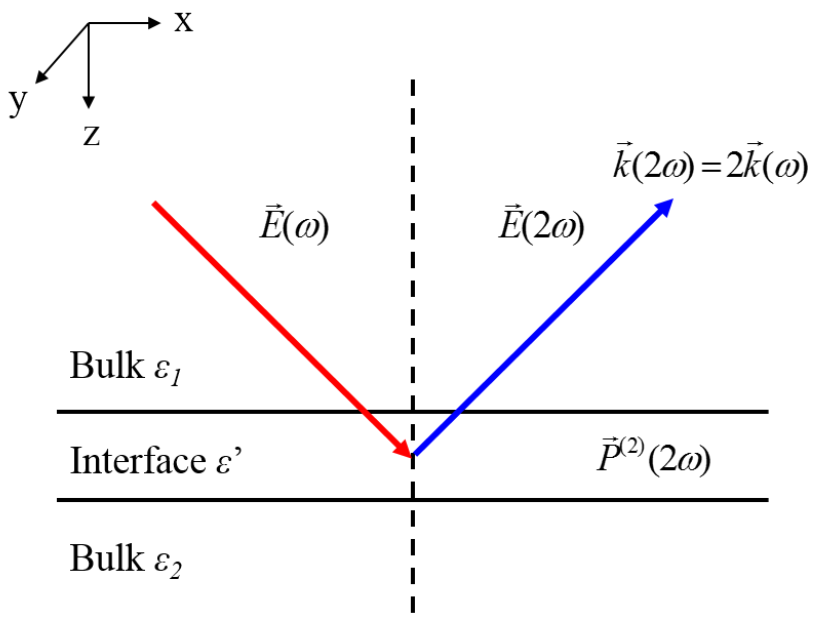

Figure 2.2 Schematic of SHG generated from a planar interface between two isotropic bulk media.

2.2.3 Second Harmonic Generation from Colloidal Interface

Aside from the planar interface, highly-curved interface, such as the interface between colloidal particle and its solvent, is also an important aspect of interest. Compared to planar surfaces in which SHG is emitted along the reflective direction, SH signal from the surfaces of colloids scatter into the space with an angular distribution determined by the sizes, shapes, and compositions of the particles.[28-29, 33-34] Therefore, SH signal from particles are often called second harmonic scattering (SHS). As discussed in last section, both the second-order nonlinear susceptibility $\chi_{eff}^{(2)}$ and the phase-matching condition govern the SH signal. High absolute value of $\chi_{eff}^{(2)}$ can be obtained when the particle itself is in resonance with the fundamental or SH light, or the non-resonant particle is covered by SHG-active probes, such as malachite green. As for the phase-matching condition, however, the situation becomes complex. As shown in Fig. 2.3, for a spherical particle, the phase difference between two ends of the particle along the diameter will be $\Delta\vec{k}\cdot\vec{L}+\pi$, in which π results from the centrosymmetry of the spherical shape.[22-23] In the forward direction,

$$|\Delta\vec{k}\cdot\vec{L}|=|(\vec{k}_{2\omega}-2\vec{k}_{\omega})\cdot\vec{L}|=\frac{4\pi(n_{2\omega}-n_{\omega})}{\lambda_{\omega}}\cdot D \tag{2.10}$$

with *D* being the particle diameter. If both refractive indices are close to each other and *L* is smaller or close to the wavelength λ_{ω}, then $|\Delta\vec{k}\cdot\vec{L}|\approx 0$ and the SH signal will destructively interfere with each other and end up with cancellation. However, consider other propagation directions at angle θ_s in that the fundamental and SH light are not parallel, Eq. 2.10 should be written as

$$|\Delta\vec{k}\cdot\vec{L}|=|2\vec{k}_{2\omega}\sin\frac{\theta_s}{2}\cdot\vec{L}|=\frac{4\pi n_{2\omega}}{\lambda_{2\omega}}\sin\frac{\theta_s}{2}\cdot D \tag{2.11}$$

assuming refractive indices of the fundamental and SH light are the same for the solvent. As the diameter *D* is smaller than the wavelength $\lambda_{2\omega}$, the equation $|\Delta\vec{k}\cdot\vec{L}|=\pi$ is valide, when the angle θ_s is large. On the other hand, when the diameter D is larger, multiple angles can satisfy the equation $|\Delta\vec{k}\cdot\vec{L}|=(2n+1)\pi$ for n=0,1,2,…, indicating that there exist multiple maxima in the angular distribution pattern.[24-25]

The above discussion is based on a simple picture of SHS from colloidal particles. A complete treatment of SHS requires theoretical frameworks, such as the nonlinear Rayleigh-Gans-Debye theory (NLRGD) or the nonlinear Mie (NLM). Details can be found in the literature.[25, 28-29, 34] Briefly, NLRGD applies to particles with various shapes, but the refractive index of particles' must be close to the solvent. On the other hand, NLM theory works regardless of the composition, but is only suitable for spherical shape. The coordinate system commonly used for SHS from the colloidal surfaces also differs from the planar interfaces. Instead of using the laboratory coordinate system, for spherical particles, the directionality of the surface polarization is often defined by the spherical local surface coordinates, in which $\parallel$ and $\perp$ represent the directions parallel and perpendicular to the local surface, respectively. With respect to isotropic systems, out of 7 non-zero elements, only 3 independent values exist. In local surface coordinates, they correspond to $\chi_{\perp\perp\perp}$, $\chi_{\perp\parallel\parallel}$ and $\chi_{\parallel\perp\parallel}$.

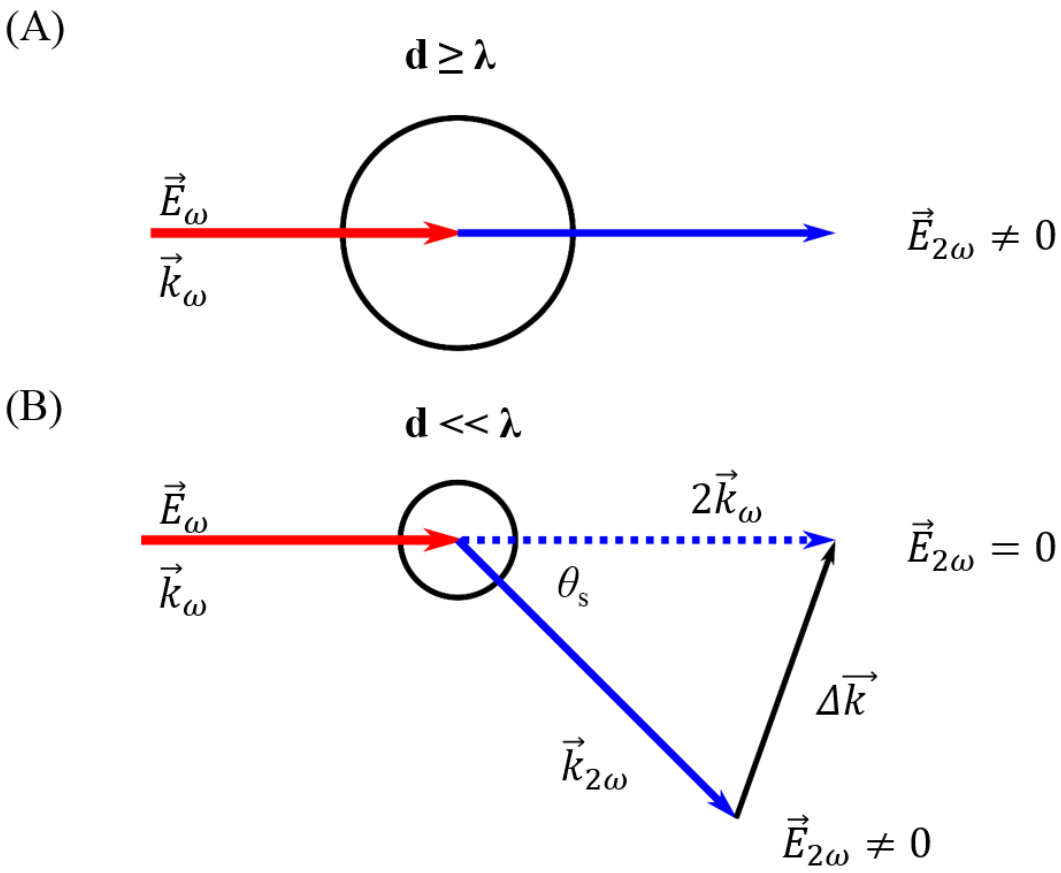

Figure 2.3 Schematic of SHS from colloidal particles with diameter larger (A) and smaller (B) than the wavelength.

2.3 Experiment

2.3.1 Experimental Setup

Two experimental setups have been built for collecting the SH emission spectrum as well as the angular distribution of SHS. The setup for the SH emission spectrum is shown in Fig. 2.4. The fundamental 800 nm pulse laser we used was provided by a Ti-Sapphire femtosecond laser (Coherent, Micra V oscillator) with 130 fs pulse duration, 78 MHz repetition rate and 300 mW average power. The polarization of the fundamental laser (horizontal to the optical table out of the laser oscillator) was controlled by a half-wave plate (HWP). A longpass filter (Schott RG695) was used to remove any possible SH signal from the optical components up to the sample.

The SH signal was obtained by focusing the 800 nm fs pulse onto a liquid jet of colloidal solution produced in a micropump-driven flow system. The beam diameter at the focus area was 40μm, corresponding to 2.4×10^{9} W/cm^{2} peak power. As it is expected that SHS from Ag NPs has a wide distribution of scattering angles, the SH signal was collected by 2-inch lenses in a wide solid angle (within ±20° in both horizontal and vertical angles around the fundamental beam propagation direction). After passing through a bandpass filter (Schott BG39, 340 nm - 600 nm) that got rid of the fundamental beam, the collected light was delivered into a monochromator (Princeton Instrument, Acton SP2300) and measured by a photomultiplier tube (PMT, R1527 Hamamatsu). The electronic signal from PMT was further amplified by a fast preamplifier (350 MHz, Stanford Research) and analyzed by a photon counting system (Stanford Research SR400). A labview (National Instrument) program was written to control the monochromator and to record data from the photon counting system. The emission spectrum was measured by scanning the wavelength through the monochromator. And the time-resolved experiment was performed by fixing

the monochromator at 400nm and collecting the SH signal at 1 sec interval synchronized by the computer.

The angle-resolved experiments were conducted at a similar setup but with different signal collection system (Fig. 2.5). The jet that was perpendicular to the optical table was located at the center of a motorized rotational stage (CR1-Z7E, Thorlabs). The scattered light was first filtered by a bandpass filter that blocked the scattered fundamental light, and then collected by a lens with 1-inch diameter and 6-inch focus length. An iris was put in front of the lens for the purpose of adjusting the angular resolution. The collected SH light subsequently passed through a pair of lenses that reduce the beam diameter, and focused onto an optical fiber by a collimator. All the collective optics were assembled on an arm mounted on the motorized rotational stage so that the collection angle can be scanned. The light transferred by the optical fiber was filtered by a bandpass filter (20 nm FWHM, Thorlabs) centered at the SH wavelength (400 nm), and was eventually delivered into a PMT. The SH signal was amplified and analyzed by the same photon counting system. The polarization of the fundamental 800nm light was adjusted by a half-wave plate (HWP) and the polarization of the SH light was selected by a Glan-Thompson polarizer before the optical filter. The experiment was controlled by an *ad hoc* labview program that synchronized all instruments.

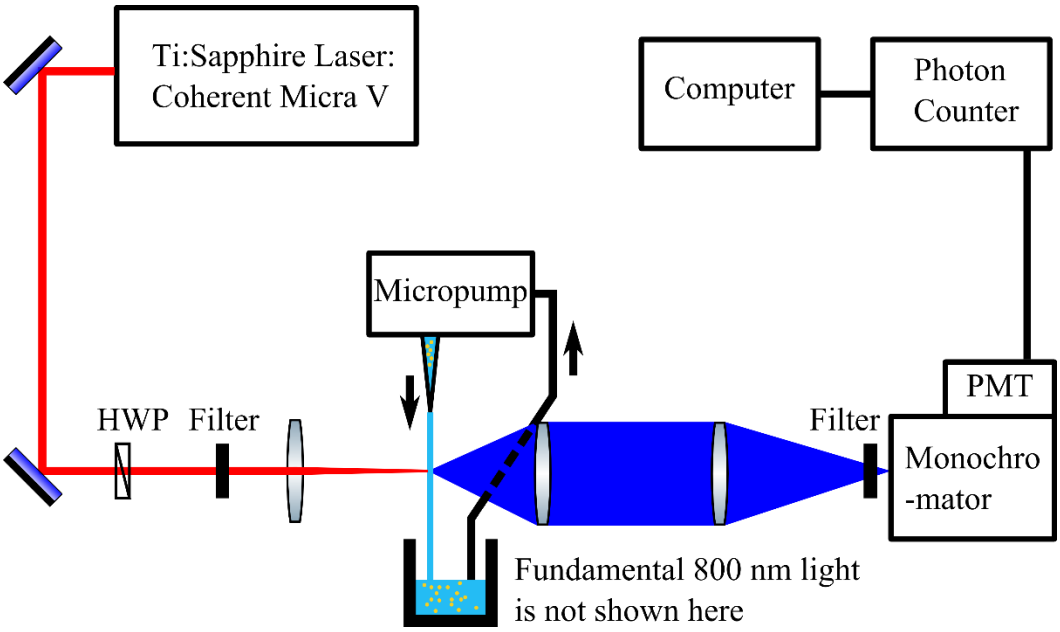

Figure 2.4 Schematic of the experimental setup for the SH emission spectrum

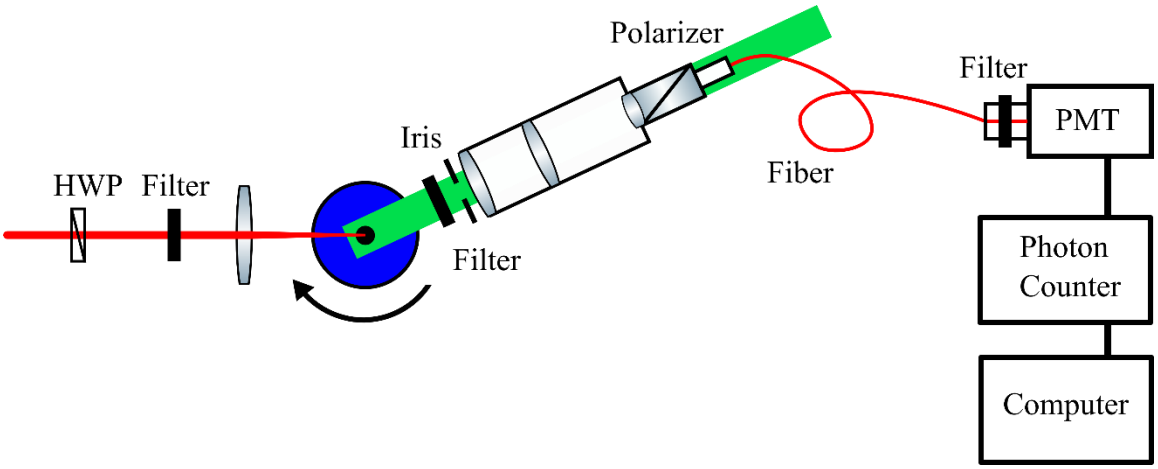

Figure 2.5 Schematic of the experimental setup for angle-resolved SHS experiments

2.3.2 Sample Flow-jet Circulation System

As for SHS experiments, sample system plays an important role because the SH signal can be weaker orders of magnitude compared to linear optical measurements. In our experiments, a flow-jet circulation system was used: a micropump made of stainless steel pull the Ag NPs suspension from the container and formed perpendicularly at the exit a liquid jet where Ag NPs was radiated by the fundamental laser.

Such flow-jet circulation system has several advantages: 1) the diameter of the liquid jet can be set based on the opening of the tip installed at the exit; 2) the Ag NPs suspension was under constant circulation that kept the nanoparticle number density uniform and also worked as stirring for the titration experiment; 3) the windowless liquid jet prevented the SH signal from the background material or the nanoparticle that adsorbed on the walls; 4) the cross-section of the liquid jet is centrosymmetric and suitable for angle-resolved experiments. Experimentally, the jet diameter was set at 2 mm so that the optical length (2 mm) would be much shorter than that using a conventional quartz cuvette (1 cm). This effort minimized the reabsorption of the SH signal by Ag NPs.

2.3.3 Sample Preparation

The citrate-stabilized Ag NPs with average particle diameter of 80 nm were purchased from British Cellbio International. Its original particle number density was 1.1×10^{9} particles/ml and was diluted by 36 times in volume with deionized water (Millipore, 18.2 MΩ·cm), so that the number of Ag NPs in the laser focus zone was around 1.0×10^{2}. TEM picture of Ag NPs is shown in Fig. 2.6. Ethanethiol (Sigma-Aldrich, 97%)

was also dissolved in deionized water. And sodium citrate (Sigma-Aldrich, 99%) was used to keep a citrate concentration of 5 μM for all samples used in the experiments.

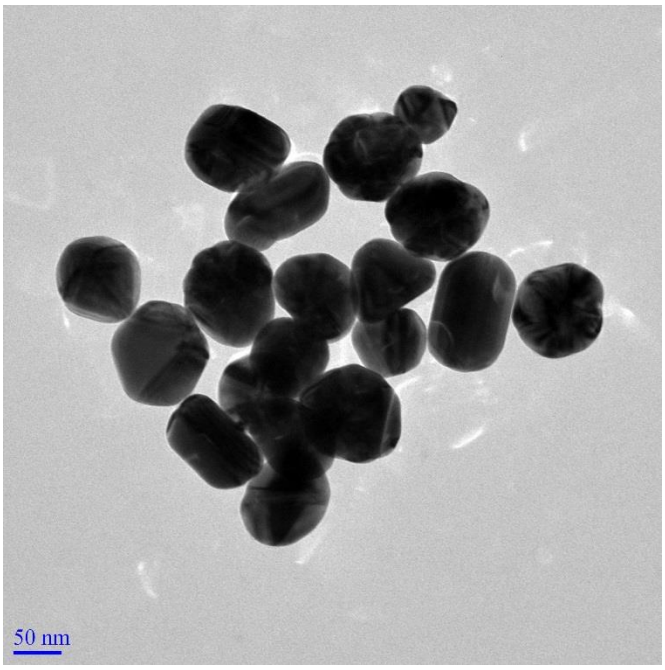

Figure 2.6 TEM picture of Ag NPs

2.3.4 Sample Stability

To assure that our experiments did not alter the bulk properties of Ag NPs, such as the size or the shape, complementary measurements have been performed. Dynamic light scattering (DLS, 90Plus/BI-MAS, Brookhaven Instrument) was used to measure the average diameters of the particles. No change of the average diameter has been detected before and after the irradiation of the fundamental 800 nm fs laser. The average diameters during the surface modification of thiols were also monitored by DLS. Size changes less than 5% of standard deviation have been measured, that was within the experimental

uncertainty. Therefore, we concluded that no coagulation or fragmentation of nanoparticles occurred in our experiment, verifying that the decrease in the SH signal did not result from the change of particles size.

Additionally, UV-Vis absorption measurement was also applied to characterize Ag NPs. Fig. 2.7 shows the extinction spectra of silver colloidal sample before and after the surface modification of ethanethiol using a Shimadzu UV-1800 spectrophotometer. A minor (<5%) change in intensity was observed with no peak position shift. As the shape and peak position in extinction spectra mainly depend on the particle shapes and sizes,[35] it was concluded that the bulk of Ag NPs did not change upon the adsorption of ethanethiol, which is reasonable considering the small size of ethanethiol molecules used here. The change of peak intensity can be explained as the quench of surface plasmon by ethanethiol.

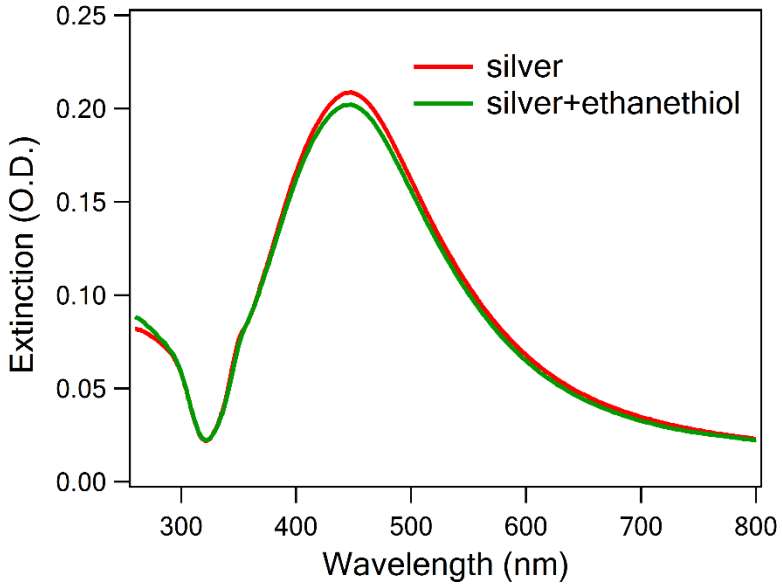

Figure 2.7 Extinction spectra of silver colloids before (red) and after (green) the addition of ethanethiol.

2.4 Results and Discussion

The SH emission spectrum from a colloid of Ag NPs is shown in Fig. 2.8. The peak centered at 400 nm is assigned to SHS while the weaker but broader peak at longer wavelength is assigned as two-photon fluorescence (TPF) of Ag NPs. The emission spectrum in Fig. 2.8 can be empirically fit by a combination of a squared Gaussian function for the 400 nm (SH) peak and a regular Gaussian function for TPF. Compared to polymer particles with similar size,[24] Ag NPs present much higher SHG signal. However, due to the practical difficulty, Ag NPs are not perfectly spherical (see Fig. 2.6). To some extent, the centrosymmetric property of Ag NPs is broken.

Fig. 2.9 illustrates the angular distribution patterns of SHS from 80 nm Ag NPs at different combinations of the input (the fundamental light) and the output (the SH light) polarizations. Since the refractive index of noble metallic nanoparticles is much higher than that of the solvent (water in this case), we applied the previously developed nonlinear Mie theory (NLM) to analyze the patterns.[34] It predicted that, out of the four combinations, P-in/P-out gives the highest SH intensity, in agreement with our experimental results. By evaluating the contributions from the susceptibility tensor components, $\chi_{\perp\perp\perp}$, $\chi_{\perp\parallel\parallel}$ and $\chi_{\parallel\perp\parallel}$, it was found that $\chi_{\perp\perp\perp}$ is the only component able to produce the pattern with well-resolved lobes displayed in Fig. 2.9A, while the other two give little contribution to the SH intensity. This result differs from our group's previous work in which $\chi_{\perp\parallel\parallel}$ dominates the SH signal arising from malachite green adsorbed at the polystyrene nanoparticle surface.[24-25] The difference may originate from the different nanoparticles' compositions, metallic vs. dielectric, as well as the orientation of malachite green molecules at the surface of the

polystyrene nanoparticles. A closer comparison between the experimental data and the theoretical calculations, however, shows some discrepancies, particularly in the combinations of P-in/S-out and S-in/S-out. Based on the NLM prediction, they ought to be forbidden, while we observed weak SH signal as seen in Fig. 2.9 C and D. This violation can be attributed to the fact that the shapes of Ag NPs are not perfectly spherical.

Although the theoretical calculation supports our deduction that the SH signal mainly originates from the surface, an experimental demonstration is still required. Previous studied carried out at flat silver or gold surfaces under ultrahigh vacuum conditions or in solution phases have showed that the chemical bonding localizes the electrons at the surface and hence reduces the nonlinear polarization and susceptibility.[36-39] Therefore, ethanethiol that contains a sulphydryl group was introduced to explore the source of the SH signal from Ag NPs. As ethanethiol molecules chemically bond with Ag atoms at the particle surface, the surface contribution to the total SH signal can be quenched. The amount of decay quantitatively indicates the portion of the SH signal from particle surface. Fig. 2.10 shows the SH intensity recorded as a function of time, following the addition of ethanethiol into the colloidal solution. The addition of thiols resulted in a considerable decrease in the SH intensity until minimum as ethanethiols reacting with the surface silver atoms reached equilibrium. The concentration of ethanethiol used here was chosen to assure that the saturation was reached at the surface. The percentage of the SH intensity decay, at saturation of quenching, was around 60% of the original SH intensity. The response of the SH signal to the addition of ethanethiol provides a direct experimental proof that the majority of the SH signal originates from the surface of Ag NPs. The

remaining part (<40%) may arise either from the unquenched surface contribution and/or contributions associated with the particle bulk.

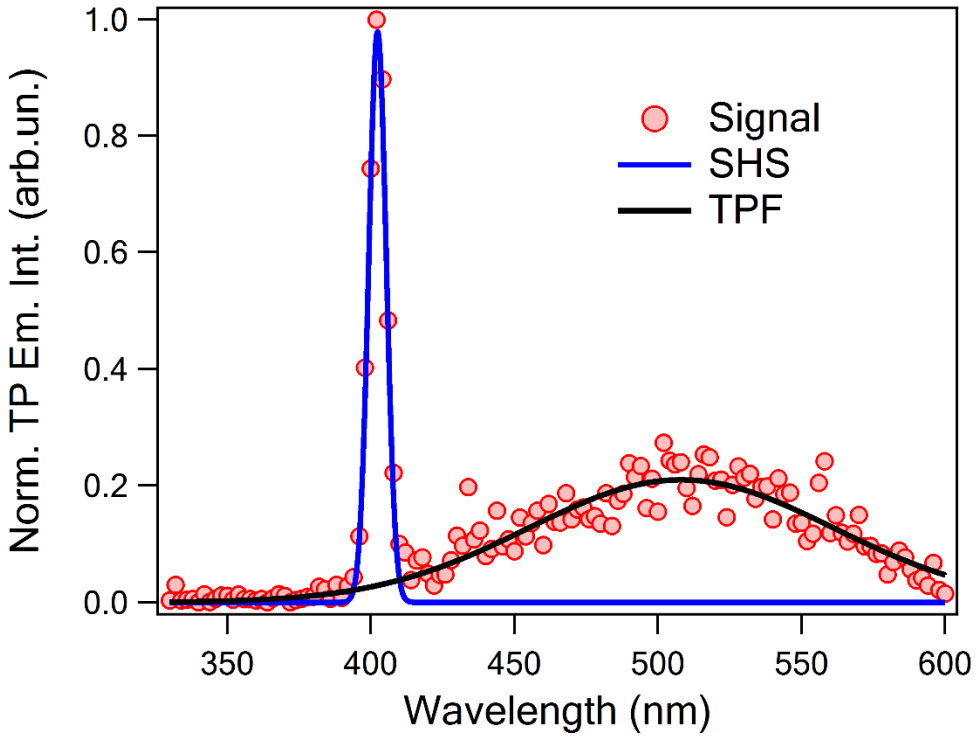

Figure 2.8 Emission spectrum of Ag NPs. SH signal (blue) is fitted by a squared Gaussian equation, and TPF (black) is fitted by a Gaussian equation.

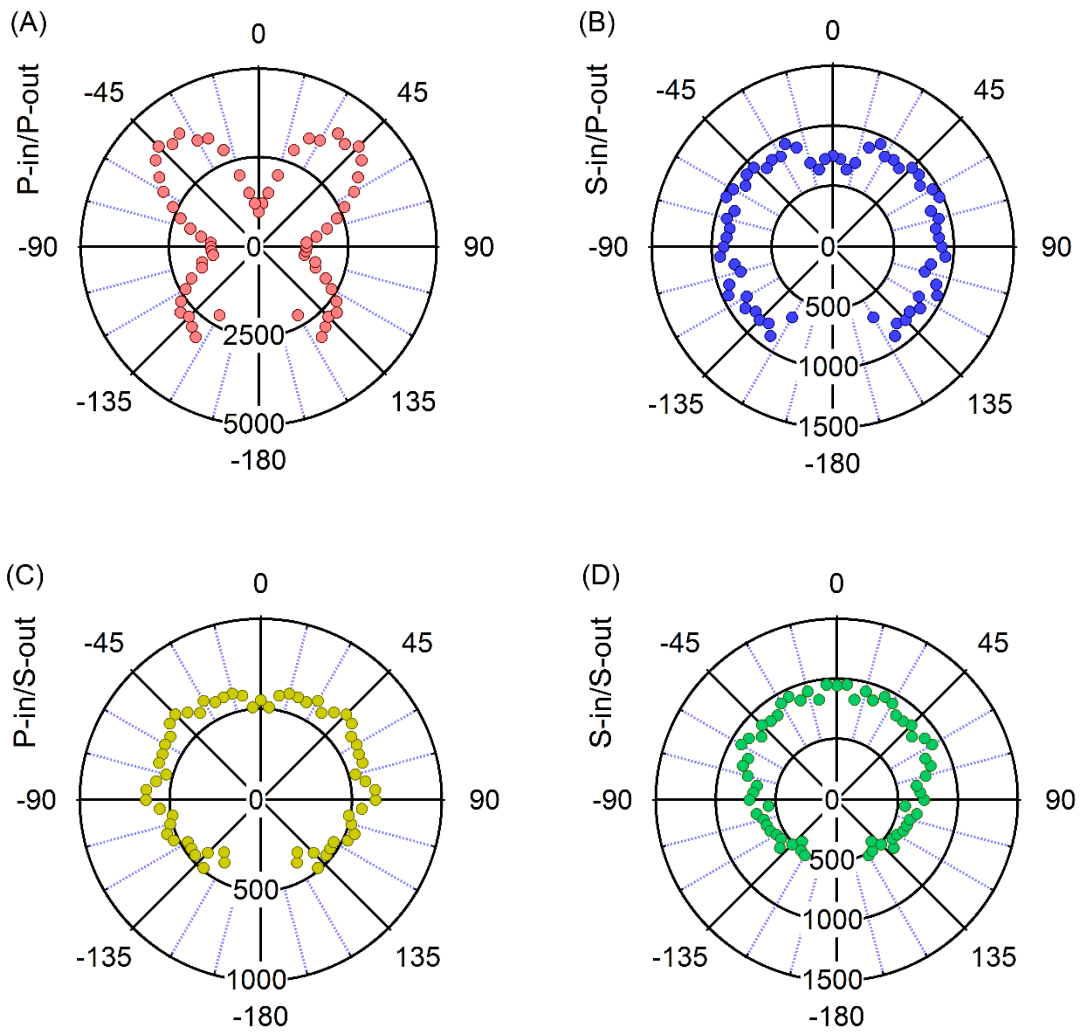

Figure 2.9 Angle-resolved SHS patterns in the horizontal plane for 80nm Ag NPs at four polarization combinations of the fundamental (input) and SH light (output): (A) P-in/P-out, (B) S-in/P-out, (C) P-in/S-out, and (D) S-in/S-out

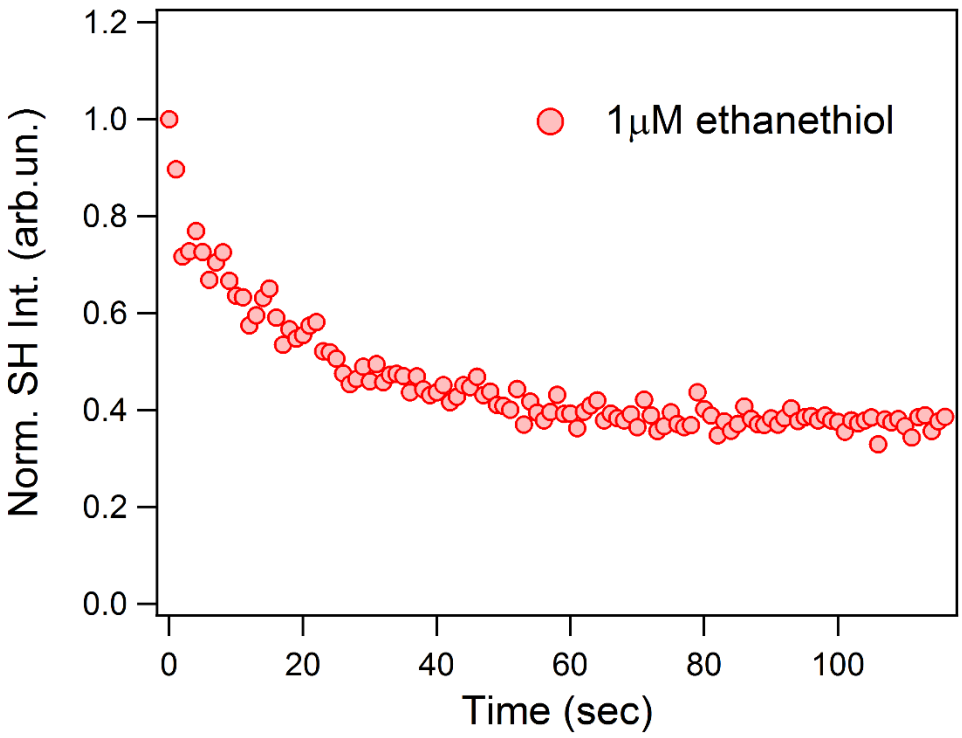

Figure 2.10 The SH intensity, normalized to unity at t = 0, as a function of time after the addition of 1μM ethanethiol

2.5 Summary

In summary, the SH signal from Ag NPs with average diameter of 80 nm have been observed in our group. The angular-dependent patterns of SHS are in good agreement with our predication based on nonlinear Mie theory.[34] It is established that $\chi_{\perp\perp\perp}$ is the dominant second-order surface susceptibility tensor element for Ag NPs. The discrepancies between the theoretical calculation and SHS data indicates that the shapes of the Ag NPs are not uniformly spherical, supported by our TEM measurement. Despite the imperfect centrosymmetric shape of the particles, experimental evidence has been presented that the majority of the SH intensity originated from the surface, not from the bulk. Thus, SHS can serve as a probe to characterize adsorption and reactions occurring at the surface of metallic nanoparticles *in situ* and in real time, particularly when the molecules of interest do not possess large nonlinear polarizability. For instance, we demonstrate the surface SHG can be quenched by chemical bonding of thiols. In return, the Gibbs free energy change and the activation energy of the thiol-silver reactions at the surface of nanoparticles can be acquired by performing concentration-dependent and temperature-dependent time-resolved experiments.

2.6 Bibliography

1. Daniel, M.-C.; Astruc, D., Gold Nanoparticles: Assembly, Supramolecular Chemistry, Quantum-Size-Related Properties, and Applications toward Biology, Catalysis, and Nanotechnology. *Chem. Rev.* **2003,** *104* (1), 293-346.
2. Eckhardt, S.; Brunetto, P. S.; Gagnon, J.; Priebe, M.; Giese, B.; Fromm, K. M., Nanobio Silver: Its Interactions with Peptides and Bacteria, and Its Uses in Medicine. *Chem. Rev.* **2013,** *113* (7), 4708-4754.
3. Halas, N. J.; Lal, S.; Chang, W.-S.; Link, S.; Nordlander, P., Plasmons in Strongly Coupled Metallic Nanostructures. *Chem. Rev.* **2011,** *111* (6), 3913-3961.
4. Rosi, N. L.; Mirkin, C. A., Nanostructures in Biodiagnostics. *Chem. Rev.* **2005,** *105* (4), 1547-1562.
5. Rycenga, M.; Cobley, C. M.; Zeng, J.; Li, W.; Moran, C. H.; Zhang, Q.; Qin, D.; Xia, Y., Controlling the Synthesis and Assembly of Silver Nanostructures for Plasmonic Applications. *Chem. Rev.* **2011,** *111* (6), 3669-3712.
6. Bellino, M. G.; Calvo, E. J.; Gordillo, G., Adsorption Kinetics of Charged Thiols on Gold Nanoparticles. *Phys. Chem. Chem. Phys.* **2004,** *6* (2), 424-428.
7. Kirk, J. S.; Bohn, P. W., Surface Adsorption and Transfer of Organomercaptans to Colloidal Gold and Direct Identification by Matrix Assisted Laser Desorption/Ionization Mass Spectrometry. *J. Am. Chem. Soc.* **2004,** *126* (18), 5920-5926.
8. Lee, K. H.; Chen, S. J.; Jeng, J. Y.; Cheng, Y. C.; Shiea, J. T.; Chang, H. T., Fluorescence and Interactions with Thiol Compounds of Nile Red-Adsorbed Gold Nanoparticles. *J. Colloid. Inter. Sci.* **2007,** *307* (2), 340-348.

9. Weeraman, C.; Yatawara, A. K.; Bordenyuk, A. N.; Benderskii, A. V., Effect of Nanoscale Geometry on Molecular Conformation: Vibrational Sum-Frequency Generation of Alkanethiols on Gold Nanoparticles. *J. Am. Chem. Soc.* **2006,** *128* (44), 14244-14245.

10. Boyd, R. W., Nonlinear Optics. 3rd ed. ed.; Academic Press: Burlington, MA :, 2008.

11. Franken, P. A.; Weinreich, G.; Peters, C. W.; Hill, A. E., Generation of Optical Harmonics. *Phys. Rev. Lett.* **1961,** *7* (4), 118.

12. Shen, Y. R., The Principles of Nonlinear Optics. Wiley: New York :, 1984.

13. Surface Polaritons Electromagnetic Waves at Surfaces and Interfaces. Agranovich, V. M.; Mills, D. L., Eds. North-Holland Pub. Co. :: Amsterdam ;, 1982.

14. Bloember.N; Chang, R. K.; Jha, S. S.; Lee, C. H., Optical Second-Harmonic Generation in Reflection from Media with Inversion Symmetry. *Phys. Rev.* **1968,** *174* (3), 813.

15. Brown, F.; Parks, R. E.; Sleeper, A. M., Nonlinear Optical Reflection from a Metallic Boundary. *Phys. Rev. Lett.* **1965,** *14* (25), 1029.

16. Heinz, T. F. Nonlinear Optics of Surfaces and Adsorbates. University of California at Berkeley, 1982.

17. Terhune, R. W.; Maker, P. D.; Savage, C. M., Optical Harmonic Generation in Calcite. *Phys. Rev. Lett.* **1962,** *8* (10), 404.

18. Shen, Y. R., Surface-Properties Probed by 2nd-Harmonic and Sum-Frequency Generation. *Nature* **1989,** *337* (6207), 519-525.

19. Shen, Y. R., Optical 2nd Harmonic-Generation at Interfaces. *Annu. Rev. Phys. Chem.* **1989,** *40*, 327-350.

20. Shen, Y. R., Studies of Liquid-Crystal Monolayers and Films by Optical 2nd Harmonic-Generation - Invited Lecture. *Liq. Cryst.* **1989,** *5* (2), 635-643.

21. Wang, H.; Yan, E. C. Y.; Borguet, E.; Eisenthal, K. B., Second Harmonic Generation from the Surface of Centrosymmetric Particles in Bulk Solution. *Chem. Phys. Lett.* **1996,** *259* (1–2), 15-20.

22. Eisenthal, K. B., Second Harmonic Spectroscopy of Aqueous Nano- and Microparticle Interfaces. *Chem. Rev.* **2006,** *106* (4), 1462-1477.

23. Jen, S.-H.; Dai, H.-L., Probing Molecules Adsorbed at the Surface of Nanometer Colloidal Particles by Optical Second-Harmonic Generation. *J. Phys. Chem. B* **2006,** *110* (46), 23000-23003.

24. Jen, S.-H.; Dai, H.-L.; Gonella, G., The Effect of Particle Size in Second Harmonic Generation from the Surface of Spherical Colloidal Particles. II: The Nonlinear Rayleigh−Gans−Debye Model. *J. Phys. Chem. C* **2010,** *114* (10), 4302-4308.

25. Jen, S.-H.; Gonella, G.; Dai, H.-L., The Effect of Particle Size in Second Harmonic Generation from the Surface of Spherical Colloidal Particles. I: Experimental Observations†. *J. Phys. Chem. A* **2009,** *113* (16), 4758-4762.

26. Wilhelm, M. J.; Sheffield, J. B.; Gonella, G.; Wu, Y.; Spahr, C.; Zeng, J.; Xu, B.; Dai, H.-L., Real-Time Molecular Uptake and Membrane-Specific Transport in Living Cells by Optical Microscopy and Nonlinear Light Scattering. *Chem. Phys. Lett.* **2014,** *605–606* (0), 158-163.

27. Zeng, J.; Eckenrode, Heather M.; Dounce, Susan M.; Dai, H.-L., Time-Resolved Molecular Transport across Living Cell Membranes. *Biophys. J.* **2013,** *104* (1), 139-145.

28. Dadap, J. I.; Shan, J.; Eisenthal, K. B.; Heinz, T. F., Second-Harmonic Rayleigh Scattering from a Sphere of Centrosymmetric Material (Vol 83, Art No 004045, 1999). *Phys. Rev. Lett.* **2003,** *91* (14).

29. Dadap, J. I.; Shan, J.; Heinz, T. F., Theory of Optical Second-Harmonic Generation from a Sphere of Centrosymmetric Material: Small-Particle Limit. *J. Opt. Soc. Am. B* **2004,** *21* (7), 1328-1347.

30. Cerullo, G.; De Silvestri, S., Ultrafast Optical Parametric Amplifiers. *Rev. Sci. Instrum.* **2003,** *74* (1), 1-18.

31. Sipe, J. E.; Moss, D. J.; Vandriel, H. M., Phenomenological Theory of Optical 2nd-Harmonic and 3rd-Harmonic Generation from Cubic Centrosymmetric Crystals. *Phys. Rev. B* **1987,** *35* (3), 1129-1141.

32. Guyotsionnest, P.; Chen, W.; Shen, Y. R., General-Considerations on Optical 2nd-Harmonic Generation from Surfaces and Interfaces. *Phys. Rev. B* **1986,** *33* (12), 8254-8263.

33. Gonella, G.; Dai, H.-L., Second Harmonic Light Scattering from the Surface of Colloidal Objects: Theory and Applications. *Langmuir* **2013,** *30* (10), 2588-2599.

34. Gonella, G.; Gan, W.; Xu, B.; Dai, H.-L., The Effect of Composition, Morphology, and Susceptibility on Nonlinear Light Scattering from Metallic and Dielectric Nanoparticles. *J. Phys. Chem. Lett.* **2012,** *3* (19), 2877-2881.

35. Mayer, K. M.; Hafner, J. H., Localized Surface Plasmon Resonance Sensors. *Chem. Rev.* **2011,** *111* (6), 3828-3857.

36. Dounce, S. M.; Yang, M.; Dai, H. L., Physisorption on a Metal Surface Probed by Surface State Resonant Second Harmonic Generation. *Surf. Sci.* **2004,** *565* (1), 27-36.

37. Heskett, D.; Song, K. J.; Burns, A.; Plummer, E. W.; Dai, H. L., Coverage Dependent Phase Transition of Pyridine on Ag (110) Observed by Second Harmonic Generation. *J. Chem. Phys.* **1986,** *85* (12), 7490-7492.

38. Heskett, D.; Urbach, L. E.; Song, K. J.; Plummer, E. W.; Dai, H. L., Oxygen and Pyridine on Ag (110) Studied by Second Harmonic Generation: Coexistence of Two Phases within Monolayer Pyridine Coverage. *Surf. Sci.* **1988,** *197* (1-2), 225-238.

39. Dannenberger, O.; Buck, M.; Grunze, M., Self-Assembly of N-Alkanethiols: A Kinetic Study by Second Harmonic Generation. *J. Phys. Chem. B* **1999,** *103* (12), 2202-2213.

CHAPTER 3

ADSORPTION OF NEUTRAL THIOL MOLECULE ON SILVER NANOPARTICLES

3.1 Introduction

Organosulfur molecules, or thiols, have been widely used to modify surface properties of noble metal surfaces in a broad range of novel technological applications.[1-3] Adsorption of thiols on the planar surfaces of noble metals, such as gold or silver, have been intensively studied for their mechanisms and rates.[3-15] It is generally accepted that the mechanism of thiol adsorption onto the gold or silver planar surface consists of many steps, starting with the physical adsorption, followed by the sulfur-metal bonding reaction as well as the reorientation of the adsorbed thiol molecules, and eventually forming a compact self-assembled monolayer (SAM).[4-5, 14-15] With respect to the adsorption rates, however, both diffusion limited and non-diffusion limited kinetics have been reported, although the conditions for the two scenarios have not been consistently defined.[5-6, 9, 13-16]

In addition to planar surfaces of noble metals, thiol adsorption has also been broadly utilized for metallic nanoparticles, such as controlling their biomedical functions,[17] tuning optical properties,[18] changing the attached chromophores,[19] and synthesizing nanoparticles and nanocages of different shapes and sizes.[20] Optical techniques are often chosen to study the reactions between the thiol molecules and the metallic nanoparticles, due to the fact that the particle surfaces are buried in colloidal solution.[18-19, 21-23] For example, a sum frequency vibrational spectroscopy (SFG) study has revealed that long-chain thiol molecules on gold nanoparticles of varying sizes have different conformations.[23]

More than a decade ago, hyper Rayleigh scattering from gold nanoparticles was first reported as an incoherent second harmonic phenomenon.[24] It was believed that there was an inherent size restriction in second harmonic scattering (SHS) such that the method could not be applied to particles with diameters much smaller than the optical wavelength. Our group, however, has demonstrated that SHS from the surface of nanometer size particles can be detected at specific scattering angles where the phase matching conditions are satisfied.[25-27] This advancement has led to the detection of SHS from silver nanoparticles (Ag NPs),[18] that was discussed in previous chapter. As the SH signal is sensitive to the polarizability of the free electrons at the surface layer of Ag NPs, the surface contribution can be identified from the response in the SH signal to the formation of silver-sulfur covalent bonds that localize the silver electrons at the surface. It turns out that the majority of the SH signal is from the surface of Ag NPs with 80 nm diameter. The surface portion of the SH signal, that dominates the total SH signal from Ag NPs, can therefore be used for probing the adsorption and reactions taking place at the surface.

The change of the SH intensity is quantitatively related to the thiol coverage at the surface, and hence can be used for the determination of the adsorption rate as well as the free energy change of the adsorptive reaction. If there is a barrier associated with the rate-limiting process in the adsorption, temperature dependence of the adsorption rate enables the determination of the activation energy and reveals what the activation process is. Herein we present experimental observations indicating that the neutral thiol adsorption at the Ag NPs surface is an activated process. For the case of 1,2-benzenedithiol, the Gibbs free energy change is < -8.8 kcal/mol, and the activation energy is determined as 8.4 kcal/mol.

This energy barrier is likely associated with the transition state during the formation of silver-sulfur bond, but not from the diffusion-limited process.

3.2 Experiment

The Ag NPs (British Cellbio International) with average particle diameter of 80 nm and number density 1.1×10^{9} particles/ml were diluted by 36 times in volume with deionized water (Millipore, 18.2 MΩ·cm). The number of Ag NPs in the laser focus zone was around 1.0×10^{2}. 1,2-benzenedithiol (Sigma-Aldrich, 96%) was dissolved in deionized water. Sodium citrate (Sigma-Aldrich, 99%) was added in all the samples at a concentration of 5 μM to maintain the stability of colloids.

The experiment setup and the time-resolved experiments for 1,2-benzenedithiol were the same as described in Chapter 2.

With respect to the titration experiment, aqueous solutions of 1,2-benzenedithiol at known high concentrations were added into the Ag colloidal suspension by a digital titrator (Hirschmann, akku-drive, 20ml unit) controlled by a computer. This allowed the synchronization between the data recording and titration through an *ad-hoc* labview program: the wavelength of the monochromator was set at the peak wavelength of the SH signal, i.e. 400nm, while the SH signal was recorded every 3 min after the 1,2-benzenedithiol aliquots were added at room temperature. This assured that the equilibrium state of the reaction was reached. The volume change induced by the titration amount was corrected by the labview program instantaneously.

In the temperature-dependent time-resolved experiments, the sample temperature was controlled by setting the temperature of the bath into which the sample container was

immersed: a hot water bath kept the temperature at (303±1) K, while a coolant bath was used to lower down the temperature to (284±1) K. The room temperature was (293±1) K. Besides, the micropump system was protected by heat insulating materials to maintain the temperature for both the sample container and the sample jet. The time-resolved experiment was performed as a labview program set the monochromator at 400nm and collected the SH signal at 1 sec interval synchronized by the computer.

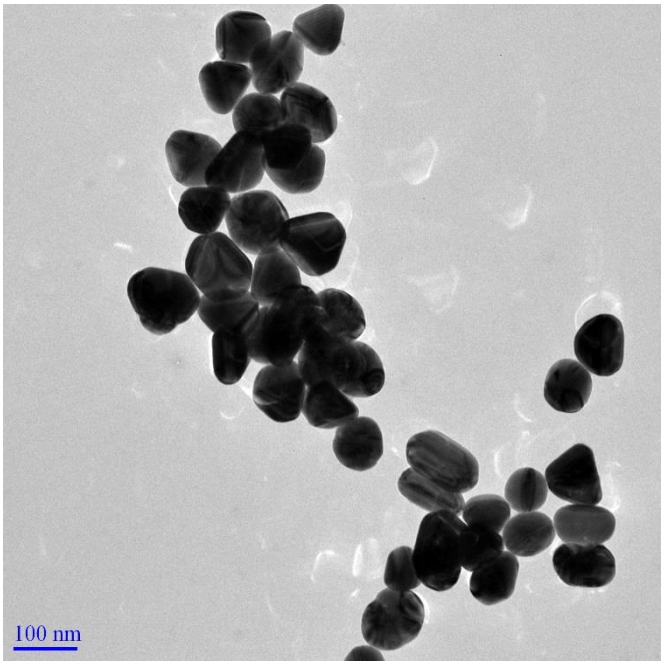

Figure 3.1 TEM picture of Ag NPs

3.3 Results and Discussion

3.3.1 Concentration-Dependent Neutral Thiol Adsorption and Gibbs Free Energy Change

The decline of the SH signal from Ag NPs depends on the thiol concentration added. An example is shown in Fig. 3.2 in which the decrease of the SH intensity reached saturation at the 1,2-benzenedithiol concentration of 2 μM. It shows that 54% of the total SH intensity vanished after the surface of Ag NPs were saturated by 1,2-benzenedithiol. This observation indicated that >54% of the SH signal was generated from the particle surface, given that the quenching efficiency was unknown. The remaining part (<46%) may arise either from the unquenchable surface contribution and/or contributions associated with the particle bulk. Based on previous ultrahigh vacuum studies,[28-30] it is reasonable to expect that the reduction of the nonlinear polarization at the Ag NPs surface is linearly proportional to the surface coverage θ of thiols. The total SH intensity can therefore be described as[6, 30]

$$I(2\omega) \propto |\chi_{Ag} - \chi_Q \theta e^{i\phi}|^2 \tag{3.1}$$

where χ_{Ag} represents the susceptibility of the bare Ag NPs (including surface and possibly bulk contributions), χ_Q is the total decrease in surface susceptibility induced by thiol adsorption at the saturation coverage, θ is the surface coverage of thiol molecule at certain concentration, and ϕ is the phase difference between the two susceptibilities.

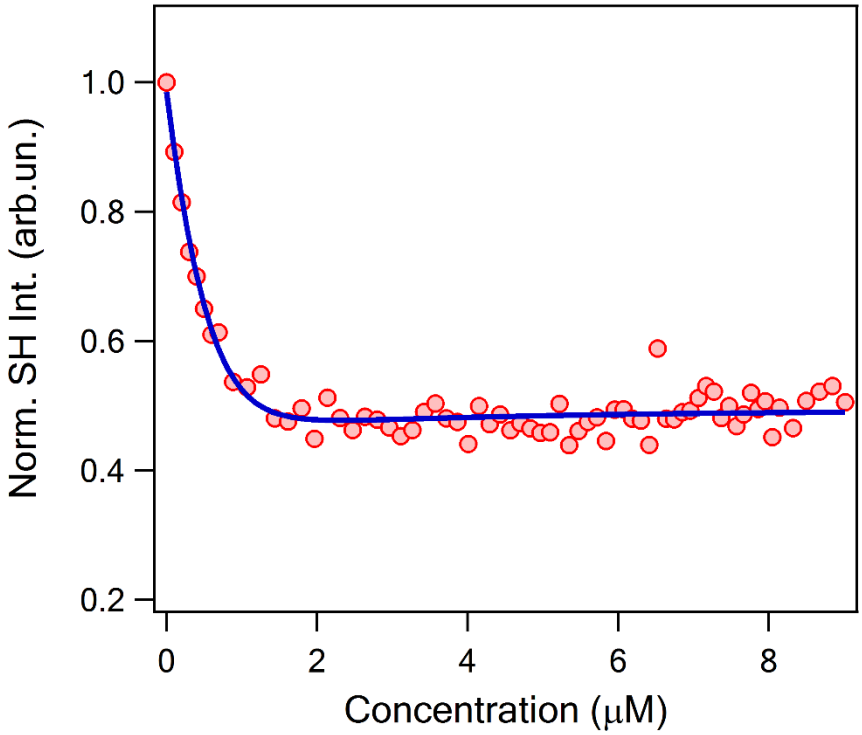

Figure 3.2 The SH intensity, normalized to unity at the point with no 1,2-benzenedithiol added, measured as a function of the 1,2-benzenedithiol concentration. The blue curve is the nonlinear least-square fitting by Eq. 3.5.

The coverage of 1,2-benzenedithiol at the surface of Ag NPs obeys the adsorption reaction between the neutral thiol molecules and Ag atoms at the surface. It appears from our experiments that the adsorption follows the Langmuir adsorption process. The Langmuir adsorption model was developed and named after Irving Langmuir in 1916,[31] based on three assumptions: 1) the adsorption is limited to one monolayer, 2) the surface is divided into sites for adsorption with equal probability for each site, and 3) there are no inter-adsorbate interactions. Hence, the equilibrium between thiols in the colloidal solution, *T*, the thiols bonded at the surface, *TS*, and the surface empty sites *ES* can be described as

$$T + ES \underset{k_{-1}}{\overset{k_1}{\rightleftharpoons}} TS \tag{3.2}$$

where k_1 is the rate constant for adsorption, and k_{-1} is the rate constant for desorption. The equilibrium constant, *K*, equals to $\frac{k_1}{k_{-1}}$.

The equilibrium equation is as below,

$$K = \frac{N}{(C-N)(N_{\max}-N)} \tag{3.3}$$

where *N* is the concentration of the occupied bonding sites, C is the initial concentration of thiol added, and $N_{\max}$ is the maximum concentration of bonding sites at the surface of nanoparticles.

By solving Eq. 3.3, the surface coverage θ , i.e. N/N_{max} , can be expressed as[32]

$$\theta = \frac{(C + N_{\max} + K^{-1}) - \sqrt{(C + N_{\max} + K^{-1})^2 - 4CN_{\max}}}{2N_{\max}} \tag{3.4}$$

Combining the surface coverage θ (Eq. 3.4) and the SH signal (Eq. 3.1), the SH intensity as a function of 1,2-benzenedithiol concentration is

$$I(2\omega) \propto | \chi_{Ag} - \chi_Q \frac{(C + N_{\max} + K^{-1}) - \sqrt{(C + N_{\max} + K^{-1})^2 - 4CN_{\max}}}{2N_{\max}} e^{i\phi} |^2 \qquad (3.5)$$

A nonlinear least-square fit in Fig. 3.2 can be achieved only as $K \geq 3 \times 10^6$ M^{-1}, which indicates that the upper limit of the adsorption Gibbs free energy change for 1,2-benzenedithiol is −8.8 kcal/mol, i.e. $\Delta G \leq$ -8.8 kcal/mol. Adsorption of thiols onto Au, Ag or Cu surfaces has been reported in the literatures.[6, 8-9, 11] The adsorption free energy obtained in this work is close to the value deduced from the infrared adsorption study of 1,2-benzenedithiol onto a Ag film in benzene solution (−9.4 kcal/mol).

3.3.2 Temperature-Dependent Time-Resolved Neutral Thiol Adsorption and Activation Energy

Fig. 3.3 shows the SH signal of Ag NPs as a function of time following the addition of 1,2-benzenedithiol at a range of concentrations from 0.1 μM to 0.5 μM. The experiments were performed at three different temperatures. The decrease of the SH signal scattered from Ag NPs resulted from the reduction of the nonlinear susceptibility of the Ag surface atoms as silver-sulfur bonds form.[6, 18]

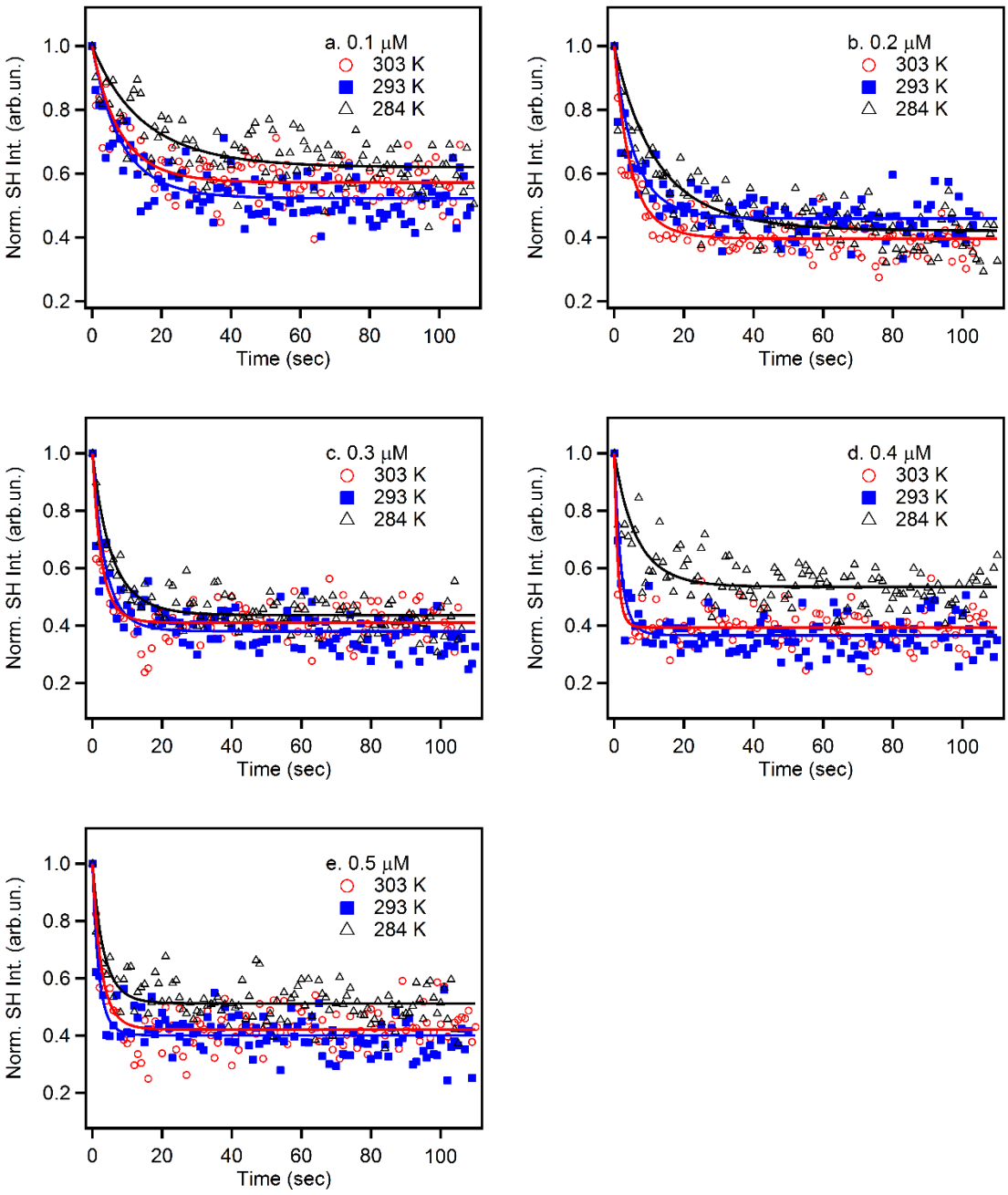

Figure 3.3 The SH intensity, normalized to unity at t = 0, as a function of time following the addition of different concentrations of 1,2-benzenedithiol (a. 0.1 μM, b. 0.2, c. 0.3 μM, d. 0.4 μM, e. 0.5 μM) at t = 0 recorded at the specified constant temperature: 303±1 K (red circle), 293±1 K (blue solid square), 284±1 K (black triangle).

Based on Langmuir model (Eq. 3.2), the kinetics equation is as follow,

$$\frac{dN}{dt} = k_1 C(N_{\max} - N) - k_{-1} N \tag{3.6}$$

where k_1 is the rate constant for adsorption, k_{-1} is the rate constant for desorption, N is the concentration of occupied bonding sites, C is the initial concentration of thiol added, and $N_{\max}$ is the maximum concentration of bonding sites at the surface of Ag NPs.

Eq. 3.6 can be simplified under the assumption that the concentration of thiols in the colloid (including those in solution and at surface) is much bigger than that of the bonding sites at the surface of Ag NPs, such that the depletion of 1,2-benzenedithiol from bulk can be neglected. By solving the differentiate equation, the surface coverage θ of 1,2-benzenedithiol as a function of time follows:

$$\theta = \frac{N}{N_{\max}} = 1 - e^{-(k_1 C + k_{-1})t} \tag{3.7}$$

By putting together Eq. 3.1 and Eq. 3.7, the SH intensity can be expressed as:

$$I(2\omega) \propto | \chi_{Ag} - \chi_Q (1 - e^{-t/\tau}) e^{i\phi} |^2 \tag{3.8}$$

Here χ_{Ag} is the total susceptibility of the nanoparticle before thiol adsorption, χ_Q is the total portion of surface susceptibility that can be quenched by thiol adsorption, and ϕ is the phase difference between these two parts. The time constant τ is associated with k_1 and k_{-1} as $\tau^{-1} = k_1 C + k_{-1}$.

Eq. 3.8 was used to fit the decay of the SH signal from Ag NPs after the addition of 1,2-benzenedithiol, as shown in Fig. 3.3. The τ^{-1} values obtained from all experiments

are displayed in Fig. 3.4. The data points at the same temperature display a linear relationship of $\tau^{-1} = k_1 C + k_{-1}$. The large error bars associated with the high concentration measurements at 303 K are due to the fact that the SH signal decayed at a rate close to the experimental temporal resolution of 1 sec. The point marked with * is not included in the analysis because of its large error bar of 0.6. For 303±1 K, the points from 0.1 to 0.4 μM are results from an average of two sets of experiments. Solid lines are fittings for the extraction of the adsorption rate constants based on Eq. 3.8. The k_1 values were acquired as: $(4.3\pm1.2)\times10^5\ M^{-1}s^{-1}$ for 284 K, $(7.0\pm1.0)\times10^5\ M^{-1}s^{-1}$ for 293 K, and $(1.1\pm0.1)\times10^6\ M^{-1}s^{-1}$ for 303 K. The k_{-1} values obtained are smaller than the uncertainty. This indicates that the desorption of the adsorbed 1,2-benzendithiol from particle surface is not energetically favored, consistent with the high adsorption free energy change we obtained in last section as well as previous studies that thiols adsorbed on noble metal surface do not desorb easily.[6, 13] Furthermore, the Arrhenius equation can be used to fit the temperature-dependent adsorption rate constants to obtain the activation energy E_a. For the adsorption of 1,2-benzenedithiol onto Ag NPs, E_a was determined as (8.4±0.3) kcal/mol, as displayed in Fig. 3.5.

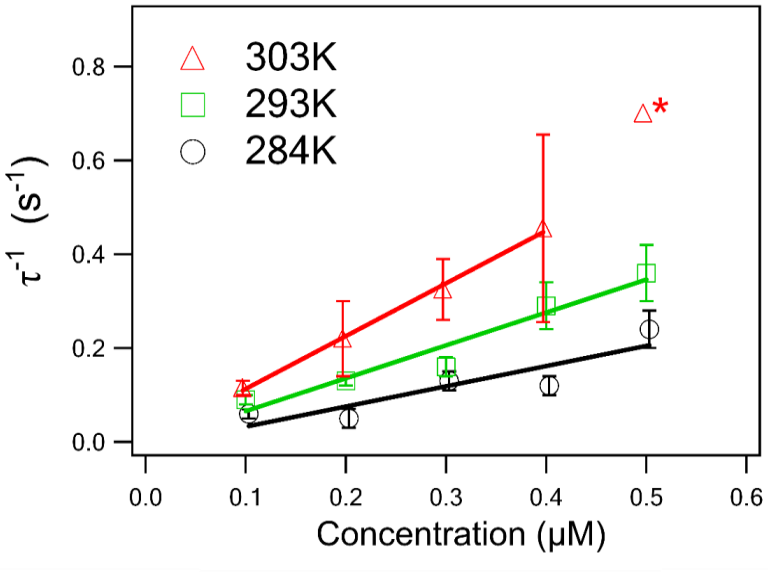

Figure 3.4 τ^{-1} values plotted as a function of thiol concentrations at three temperatures: 303±1 K (red triangles), 293±1 K (green squares), 284±1 K (black circles).

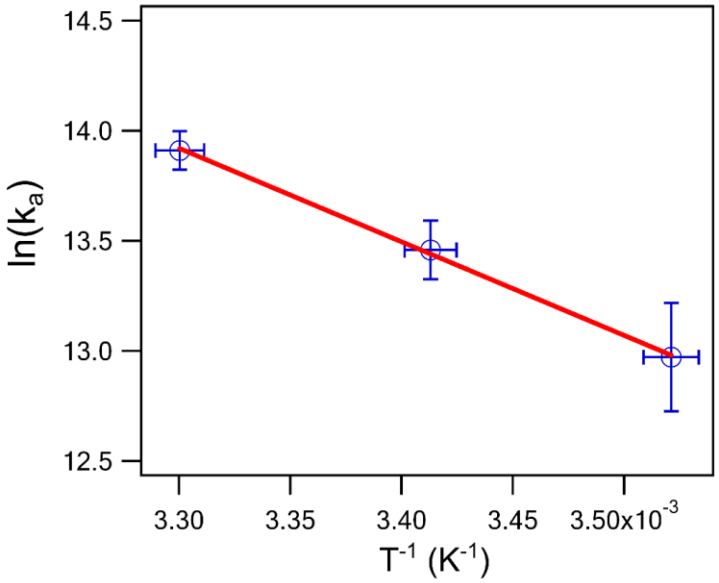

Figure 3.5 Arrhenius plot of the adsorption rate constants. The red solid line is the nonlinear least square fit.

In the literatures, the adsorption of decanethiol on Au(111) surfaces in ethanol have been reported to have an energy barrier as 7.1 kcal/mol,[15] close to the value of 6.9 kJ/mol for the adsorption of several alkanethiols on Au(111) surface obtained in ultrahigh vacuum study.[10] Despite the differences in metal surfaces and solvents, the activation energy of 8.4 kcal/mol for 1,2-benzenedithiol appears to 1.3 kcal/mol higher. A previous report has showed that both sulfur atoms are bonded on the silver surface,[11] and the large activation energy we observed can be associated with the bonding reactions of two sulfhydryl groups.

3.3.3 Model of Neutral Thiol Adsorption on Silver Nanoparticles

The commonly accepted mechanism for thiol adsorption onto noble metal surfaces starts with a physical adsorption process before chemical reactions.[4-5, 13-15] The activation barrier of 8.4 kcal/mol is too high to be associated with the physical processes such as diffusion. The correlation with the number of bonds also suggests that large activation energy is from the chemical bonding process. As comparison, several studies of thiols adsorption onto flat gold surfaces reported that the adsorption rate was diffusion limited, particularly when the thiol concentration in the solution is at the micromolar scale.[5, 13, 15] Notice that the average diffusion distance for thiol molecules traveling to the planar surface can be as long as 1.9 mm for a 2 μM solution.[5] On the other hand, in the environment of a colloidal solution, the average distance between thiol molecules and Ag NPs is on the order of 10 μm given the average distance between two nearby particles is about 30 μm based on the particle density used. This short distance is consistent with the assertion that diffusion is not the rate-determining step and not the source of the activation energy.

The stability of silver colloids are maintained by the surface coverage of citrate ions that establishs the charge-charge repulsion to prevent Ag NPs from aggregation. The presence of citrate ions may create a barrier for the thiols to physically approach the surface. However, considering the neutral nature of 1,2-benzenedithiol, the physical adsorption may not dominate the entire adsorption process. The activation barrier of (8.4±0.3) kcal/mole is too high to be associated with physical adsorption alone. Thus, we attribute this activation energy mainly to the formation of the transition state during the chemical reaction. Herein we propose a mechanism illustrated in Fig. 3.6. It is reasonable to believe that the activation energy is required for the breaking of the S-H bonds and the formation of the S-Ag bonds, so we propose the transition state to have sulfur atoms weakly interacting with both hydrogen atoms and silver atoms. The final structure of 1,2-benzenedithiol molecules adsorbed on Ag surface was based on the previous infrared spectroscopic study.[11]

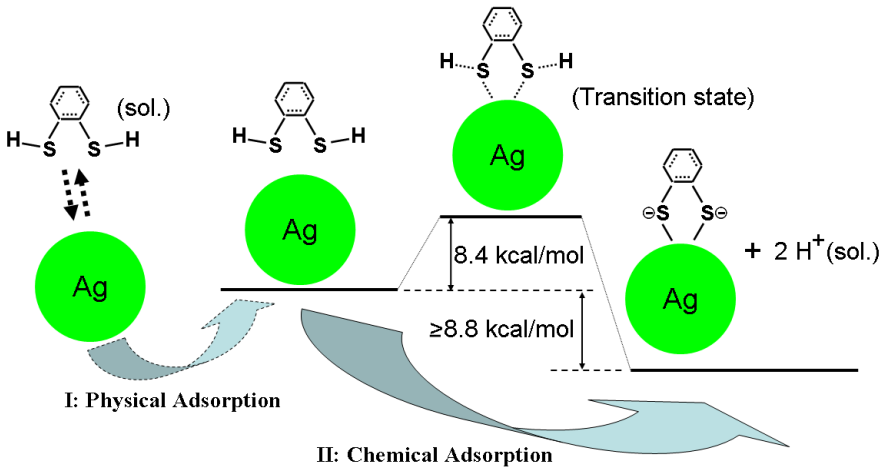

Figure 3.6 Schematic illustration of the mechanism and the energy change associated with the adsorption of 1,2-benzenedithiol on Ag NPs.

3.4 Summary

In summary, second harmonic scattering has been demonstrated as a powerful probe to investigate the adsorption process between Ag NPs and the neutral thiol molecules, i.e. 1,2-benzenedithiol. Both the Gibbs free energy change ($\leq$ -8.8 kcal/mol) and the activation energy (8.4±0.3) kcal/mol of the adsorption in aqueous silver colloids have been determined respectively in the concentration dependent and temperature dependent time-resolved experiments. This energy barrier is attributed to the formation of the transition state during the bonding reaction, not the physical adsorption or diffusion processes.

3.5 Bibliography

1. Daniel, M.-C.; Astruc, D., Gold Nanoparticles: Assembly, Supramolecular Chemistry, Quantum-Size-Related Properties, and Applications toward Biology, Catalysis, and Nanotechnology. *Chem. Rev.* **2003,** *104* (1), 293-346.
2. Love, J. C.; Estroff, L. A.; Kriebel, J. K.; Nuzzo, R. G.; Whitesides, G. M., Self-Assembled Monolayers of Thiolates on Metals as a Form of Nanotechnology. *Chem. Rev.* **2005,** *105* (4), 1103-1169.
3. Schreiber, F., Structure and Growth of Self-Assembling Monolayers. *Prog. Surf. Sci.* **2000,** *65* (5-8), 151-256.
4. Bain, C. D.; Troughton, E. B.; Tao, Y. T.; Evall, J.; Whitesides, G. M.; Nuzzo, R. G., Formation of Monolayer Films by the Spontaneous Assembly of Organic Thiols from Solution onto Gold. *J. Am. Chem. Soc.* **1989,** *111* (1), 321-335.
5. Camillone, N., Diffusion-Limited Thiol Adsorption on the Gold(111) Surface. *Langmuir* **2004,** *20* (4), 1199-1206.
6. Dannenberger, O.; Buck, M.; Grunze, M., Self-Assembly of N-Alkanethiols: A Kinetic Study by Second Harmonic Generation. *J. Phys. Chem. B* **1999,** *103* (12), 2202-2213.
7. Fenter, P.; Eberhardt, A.; Eisenberger, P., Self-Assembly of N-Alkyl Thiols as Disulfides on Au (111). *Science* **1994,** *266* (5188), 1216-1218.
8. Hatchett, D. W.; Uibel, R. H.; Stevenson, K. J.; Harris, J. M.; White, H. S., Electrochemical Measurement of the Free Energy of Adsorption of N-Alkanethiolates at Ag(111). *J. Am. Chem. Soc.* **1998,** *120* (5), 1062-1069.

9. Karpovich, D. S.; Blanchard, G. J., Direct Measurement of the Adsorption Kinetics of Alkanethiolate Self-Assembled Monolayers on a Microcrystalline Gold Surface. *Langmuir* **1994,** *10* (9), 3315-3322.

10. Lavrich, D. J.; Wetterer, S. M.; Bernasek, S. L.; Scoles, G., Physisorption and Chemisorption of Alkanethiols and Alkyl Sulfides on Au(111). *J. Phys. Chem. B* **1998,** *102* (18), 3456-3465.

11. Lee, Y. J.; Jeon, T. C.; Paik, W. K.; Kim, K., Self-Assembly of 1,2-Benzenedithiol on Gold and Silver: Fourier Transform Infrared Spectroscopy and Quartz Crystal Microbalance Study. *Langmuir* **1996,** *12* (24), 5830-5837.

12. Nuzzo, R. G.; Zegarski, B. R.; Dubois, L. H., Fundamental Studies of the Chemisorption of Organosulfur Compounds on Gold (111). Implications for Molecular Self-Assembly on Gold Surfaces. *J. Am. Chem. Soc.* **1987,** *109* (3), 733-740.

13. Schlenoff, J. B.; Li, M.; Ly, H., Stability and Self-Exchange in Alkanethiol Monolayers. *J. Am. Chem. Soc.* **1995,** *117* (50), 12528-12536.

14. Subramanian, R.; Lakshminarayanan, V., A Study of Kinetics of Adsorption of Alkanethiols on Gold Using Electrochemical Impedance Spectroscopy. *Electrochim. Acta* **2000,** *45* (27), 4501-4509.

15. Han, Y.; Uosaki, K., Effects of Concentration and Temperature on the Formation Process of Decanethiol Self-Assembled Monolayer on Au(111) Followed by Electrochemical Reductive Desorption. *Electrochim. Acta* **2008,** *53* (21), 6196-6201.

16. Buck, M.; Grunze, M.; Eisert, F.; Fischer, J.; Trager, F., Adsorption Kinetics of N-Alkyl Thiols on Gold Studied by Second Harmonic Generation and X-Ray Photoelectron Spectroscopy. *J. Vac. Sci. Technol. A* **1992,** *10* (4), 926-929.

17. Chung, Y. C.; Chen, I. H.; Chen, C. J., The Surface Modification of Silver Nanoparticles by Phosphoryl Disulfides for Improved Biocompatibility and Intracellular Uptake. *Biomaterials* **2008,** *29* (12), 1807-1816.

18. Gan, W.; Gonella, G.; Zhang, M.; Dai, H. L., Reactions and Adsorption at the Surface of Silver Nanoparticles Probed by Second Harmonic Generation. *J. Chem. Phys.* **2011,** *134* ((4)), 041104.

19. Lee, K. H.; Chen, S. J.; Jeng, J. Y.; Cheng, Y. C.; Shiea, J. T.; Chang, H. T., Fluorescence and Interactions with Thiol Compounds of Nile Red-Adsorbed Gold Nanoparticles. *J. Colloid. Inter. Sci.* **2007,** *307* (2), 340-348.

20. Cho, E. C.; Cobley, C. M.; Rycenga, M.; Xia, Y. N., Fine Tuning the Optical Properties of Au-Ag Nanocages by Selectively Etching Ag with Oxygen and a Water-Soluble Thiol. *J. Mater. Chem.* **2009,** *19* (35), 6317-6320.

21. Bellino, M. G.; Calvo, E. J.; Gordillo, G., Adsorption Kinetics of Charged Thiols on Gold Nanoparticles. *Phys. Chem. Chem. Phys.* **2004,** *6* (2), 424-428.

22. Kirk, J. S.; Bohn, P. W., Surface Adsorption and Transfer of Organomercaptans to Colloidal Gold and Direct Identification by Matrix Assisted Laser Desorption/Ionization Mass Spectrometry. *J. Am. Chem. Soc.* **2004,** *126* (18), 5920-5926.

23. Weeraman, C.; Yatawara, A. K.; Bordenyuk, A. N.; Benderskii, A. V., Effect of Nanoscale Geometry on Molecular Conformation: Vibrational Sum-Frequency

Generation of Alkanethiols on Gold Nanoparticles. *J. Am. Chem. Soc.* **2006,** *128* (44), 14244-14245.

24. Vance, F. W.; Lemon, B. I.; Hupp, J. T., Enormous Hyper-Rayleigh Scattering from Nanocrystalline Gold Particle Suspensions. *J. Phys. Chem. B* **1998,** *102* (50), 10091-10093.

25. Jen, S.-H.; Dai, H.-L., Probing Molecules Adsorbed at the Surface of Nanometer Colloidal Particles by Optical Second-Harmonic Generation. *J. Phys. Chem. B* **2006,** *110* (46), 23000-23003.

26. Jen, S.-H.; Dai, H.-L.; Gonella, G., The Effect of Particle Size in Second Harmonic Generation from the Surface of Spherical Colloidal Particles. Ii: The Nonlinear Rayleigh−Gans−Debye Model. *J. Phys. Chem. C* **2010,** *114* (10), 4302-4308.

27. Jen, S.-H.; Gonella, G.; Dai, H.-L., The Effect of Particle Size in Second Harmonic Generation from the Surface of Spherical Colloidal Particles. I: Experimental Observations†. *J. Phys. Chem. A* **2009,** *113* (16), 4758-4762.

28. Dounce, S. M.; Yang, M.; Dai, H.-L., Physisorption on a Metal Surface Probed by Surface State Resonant Second Harmonic Generation. *Surf. Sci.* **2004,** *565* (1), 27-36.

29. Heskett, D.; Song, K. J.; Burns, A.; Plummer, E. W.; Dai, H. L., Coverage Dependent Phase Transition of Pyridine on Ag(110) Observed by Second Harmonic Generation. *J. Chem. Phys.* **1986,** *85* (12), 7490-7492.

30. Heskett, D.; Urbach, L. E.; Song, K. J.; Plummer, E. W.; Dai, H. L., Oxygen and Pyridine on Ag(110) Studied by Second Harmonic Generation: Coexistence of Two Phases within Monolayer Pyridine Coverage. *Surf. Sci.* **1988,** *197* (1), 225-238.

31. Langmuir, I., The Constitution and Fundamental Properties of Solids and Liquids Part I Solids. *J. Am. Chem. Soc.* **1916,** *38,* 2221-2295.

32. Wang, H.; Yan, E. C. Y.; Borguet, E.; Eisenthal, K. B., Second Harmonic Generation from the Surface of Centrosymmetric Particles in Bulk Solution. *Chem. Phys. Lett.* **1996,** *259* (1–2), 15-20.

CHAPTER 4

ADSORPTION OF ANIONIC THIOL MOLECULE ON SILVER NANOPARTICLES

4.1 Introduction

Nanoparticles have been intensively studied for many current and potential applications in chemical, material, and medical technologies.[1-3] In many of the applications utilizing colloidal particles there is a need to modify the particle surface either to provide the particles with new functionalities by attaching specific molecular groups (active functionalization) or to reduce/eliminate undesirable interactions of the particles with their surroundings (passive functionalization). For metallic particle surfaces, even though new routes, such as the use of N-heterocyclic carbenes,[4-5] are continuously proposed, so far the most versatile method for functionalizing the metallic particle surface, quite independently from the desired functional group, is through thiolation.[6-8] Indeed, molecules containing a sulfhydryl group, which has high affinity with noble metals, presents an efficient route for surface modification.[9] As thiolation constitutes an important and frequently used surface modification step,[10-11] a mechanistic understanding of the reactions between thiols and metallic particle surfaces is of great importance to the control of the particle surface properties and the development of new surface modification methods.[4] The adsorption of charged thiols can be used, for instance, to alter the surface charge properties and therefore enable specific applications of metallic nanoparticles. An example is the case in which cationic thiols are used to promote J-aggregation of anionic cyanines on the surface of Au NPs.[12]

Despite the importance of understanding molecular interactions at the surface of metallic particles, studies carried out on metallic nanoparticle surfaces are lacking when compared to their planar surface counterpart, and there is an even smaller number of studies investigating Ag compared to Au. This is because, when compared to the planar surface case, characterizing the metallic particle surface in the colloidal environment is experimentally more complex. To prevent particles from aggregating, stabilizers such as citrate (Cit) are routinely used to treat the particle surface. Furthermore, there is the need for an *in situ* surface-sensitive method that is capable of probing the surface of nanometer size particles buried in the colloidal solution.

The effectiveness of second harmonic scattering (SHS) for detecting molecules at particle surfaces in the colloidal environment was first demonstrated by Eisenthal and coworkers.[13] Our group[14-19], along with others[20-24], has demonstrated that SHS is capable of probing the surface of nanometer size particles in colloids. In particular, we have shown that the surface layer of metallic nanoparticles can be examined.[14-17] SHS refers to the process in which the coherent SH signal generated by a particle is scattered by the particle itself because its size is comparable to or smaller than the wavelength used in the experiment. As a coherent second-order optical process, second harmonic generation (SHG) is intrinsically interface sensitive. In the electric dipole approximation, when the bulk presents a center-of-inversion symmetry, the surface is the sole source of SHG.

In the past, SHG has been used extensively to study planar surfaces,[25-29] including polycrystalline gold surfaces in aqueous solutions.[29-30] Our group has shown that adsorption and reaction of thiol molecules on the surface of metallic particles in colloidal solutions can be characterized by SHS.[14-15] The SH signal detected in those experiments

has been shown to be mostly from the surface of the Ag nanoparticles (Ag NPs).[14] With the surface origin of the SH signal established, SHS was then used to probe the adsorption reaction of a neutral thiol, 1,2-benezenedithiol, on Ag NPs and to determine the adsorption free energy, saturation density as well as reaction activation energy.[15]

In this chapter, we report the characterization of the adsorption reaction of negatively charged thiols onto Cit-stabilized Ag NPs. An alkanethiol molecule with a sulfonate endgroup (SO_3^-), such as 3-mercaptopropanesulfonate (MPS), has low pK_a ($pK_a < -1$).[31] In our experimental condition, the pH of the colloidal solution is 6.6 (which only decreases slightly after thiol adsorption[32]) at which little to no MPS is in neutral form. Through SHS measurements, supported by results from other complementary techniques, we demonstrate that this sulfonated thiol is able to chemisorb to the Ag NPs surface and further stabilize the Ag NPs by replacing the physisorbed water and Cit ions and thus increasing the amount of negative charges at the surface. The higher stability may facilitate the use of MPS adsorbed-Ag NPs as more effective intermediates for surface modification. Most importantly, it is shown that, due to the presence of charges at the particle surface, the mechanism of anionic thiols adsorption is different from that of neutral thiols.[14-15]

4.2 Experiment

4.2.1 Second Harmonic Scattering Experiments

The experimental setup for the SH signal collection was the same as described in Chapter 2 and Chapter 3. However, due to the fact that the anionic thiol presents a much slower adsorption rate than that of neutral thiol, the sample system was varied depending on the types of experiments.

As for the titration experiments, instead of using a digital titrator to add the thiol in the sample, 40 samples were prepared by means of distributing 800 ml of Ag NPs solution equally into 40 test tubes, each containing a final volume equal to 20 ml. An aqueous stock solution of MPS was prepared at a concentration of 2.5 mM, and different aliquots of this stock solution were added to the 40 tubes so that the final MPS concentrations in the tubes ranged from 0 to 50 μM. The tubes were shaken at 100 RPM at 25 °C for 12 hours until equilibrium. The content of each tube was then used to fill the reservoir of the liquid jet setup followed by the same procedure as described in Chapter 2. In addition, since the SH emission peak has always been superimposed to a broad two-photon fluorescence background, to extract the pure SH signal, the emission spectrum was fitted using the sum of a squared Gaussian function for the 400 nm (SH) peak and a regular Gaussian function for the two-photon fluorescence for the determination of the SH intensity.

To minimize the effect of liquid evaporation, especially when the temperature was high, a quartz fluorimeter cell (62F-Q-10 from Starna Cells, Inc. 1 cm path length) was employed. Another advantage of using the fluorimeter cell is that it provides higher precision for temperature control: by tuning the temperature of the water flowing through the cell jacket, it was possible to precisely control the temperature of the sample from 293 K to 333 K at the interval of 10 K. The actual temperature of the solution was measured using a thermocoupler. At a given temperature, 1.5 ml of the Ag NPs colloidal solution was added into the cell. The SH signal as a function of time was collected after the addition of an aliquot of MPS stock solution chosen in such a way that the final concentration of MPS in the cell equaled to 50 μM. A magnetic bar was used to stir the sample continuously during the data recording.

4.2.2 Dynamic Light Scattering and Zeta Potential Measurements

Hydrodynamic size and zeta potential (ζ) of Ag NPs in aqueous colloidal solution have been measured with Malvern Zetasizer Nano ZSP using disposable folded capillary cells. Measurements were conducted at (25.0±0.1) °C with a 632.8 nm red laser. The average value out of a total of three measurements have been acquired for each sample.

4.2.3 Sample Preparation

Sodium citrate dehydrate (99%), sodium 3-mercaptopropanesulfonate (MPS, 90%), 11-mercaptoundecanoic acid (MUA, 98%) were purchased from Sigma-Aldrich Inc. Deionic (DI) water (18.2 MΩ·cm) was prepared in the laboratory using a Barnstead E-pure Ultrapure Water Purification system.

The Cit-stabilized Ag NPs were received from our collaborator, Dr. Brendan DeLacy. Briefly, a modified procedure by Lee and Meisel was used to prepare Ag NPs.[33] Approximately 110 mg of $AgNO_3$ were dissolved in 400 mL deionized H_2O (18 MΩ·cm) and placed in a 1-liter 3-neck flask. Separately, 10 mL of 1% (wt/wt) trisodium citrate solution was placed in an addition funnel, which was attached to a second neck of the flask. Additionally, to minimize evaporation losses, a condenser tube was placed on the center neck of the flask. The solution was then heated to 100°C using a heating jacket and temperature controller (Glass-Col, Terre Haute, IN), while magnetically stirring and refluxing. Upon reaching the boiling point, the trisodium citrate solution was added drop-wise. Heating continued for an additional hour at 100°C. Finally, the heating jacket was removed and the solution was stirred for an additional hour at room temperature. The final

approximate concentration of the silver colloid is 0.3 mg/mL, assuming a 100% yield. The size and shape of the Ag NPs were characterized by TEM shown in Fig. 4.1.

Before the experiments, the Ag NPs colloidal solutions have been pretreated with dialysis to remove the chemicals left over from the synthesis. As shown in Fig. 4.2, it has been experimentally observed that as [Cit] increases the ζ becomes more negative up to a [Cit] = 30 μM above which no further change is observed. Hence we chose to stabilize our stock solution using a Cit concentration equal to 30 μM. For dialysis, a sulfur-free spectra/Pro 7 RC membrane (Spectrum Laboratories, Inc. MWCO 2000) was used. After soaking for 30 min with high volumes of DI-water, the dialysis membrane was loaded with Ag NPs, and then placed in the dialysis buffer, 30 μM Cit solution, at a volume equal to 200 times that of the original sample. A clean magnetic stir bar was used to stir the entire solution. Each 30 min the dialysis buffer was refreshed and the whole procedure repeated 8 times. The dialysis treatment appeared not to influence the UV-Vis and two-photon emission spectra of the Ag NPs. Unless otherwise specified, all Ag NPs were used after diluting 40 times this stock solution. By comparing the two-photon emission spectra as well as UV-Vis spectra of dialyzed and undialyzed samples (see Fig. 4.3) it was concluded that dialysis does not influence the optical properties of the Ag NPs colloidal solution.

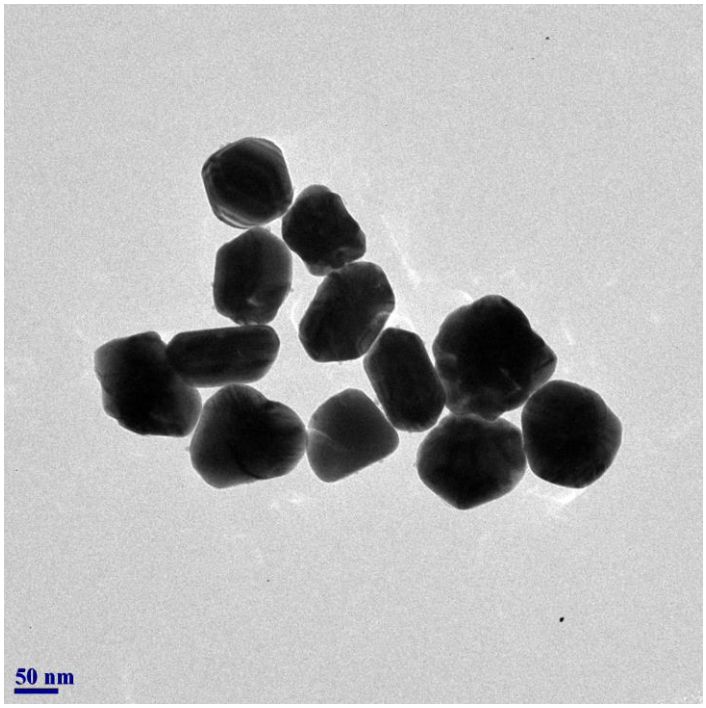

Figure 4.1 TEM image of Ag NPs.

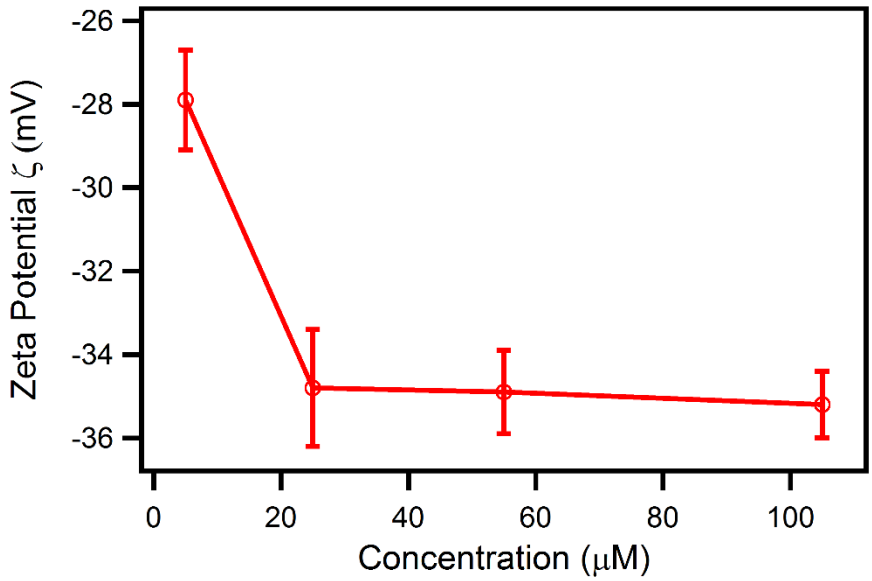

Figure 4.2 Zeta potential (ζ) of Ag NPs in aqueous colloidal solution as a function of Cit concentrations.

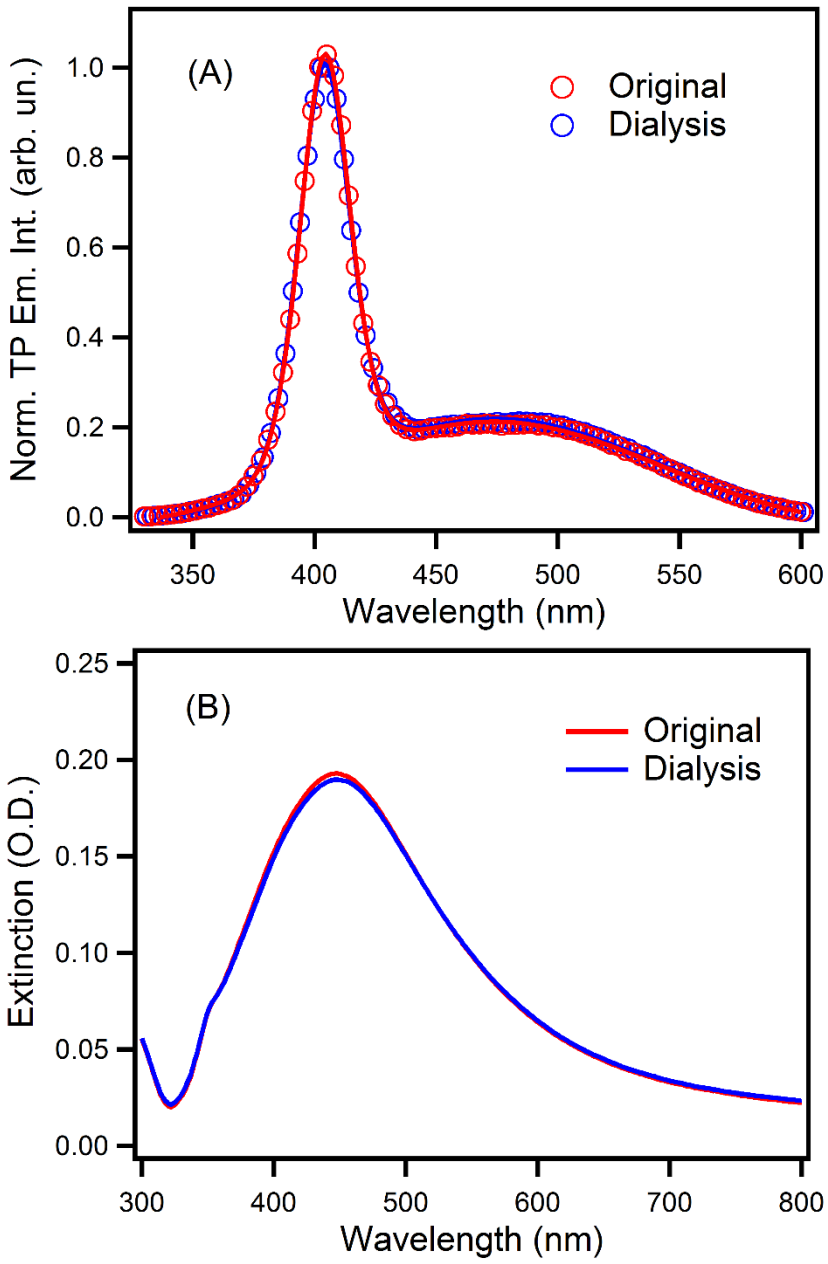

Figure 4.3 (A) Two-photon emission spectra of Ag NPs before (red, "original") and after (blue, "dialysis") dialysis. (B) UV-Vis extinction spectra of Ag NPs colloidal solution before (red, "original") and after (blue, "dialysis") dialysis.

4.3 Results and Discussion

As demonstrated in Chapter 3, the adsorption of thiols on noble metal colloids can be characterized using SHS. The SH signal mainly originates from the surface of Ag NPs and can be quenched by the formation of the sulfur-silver covalent bonding. Besides, the magnitude of the SH signal is related to the thiol coverage on the surface. Therefore, monitoring the SH signal as functions of thiol concentration and time provides both the thermodynamic and kinetic information for the adsorption reaction between the thiol molecules and the Ag NPs.

4.3.1 Concentration-Dependent Anionic Thiol Adsorption on Silver Nanoparticles

As for anionic thiol molecules, Fig. 4.4A shows the dependence of the SH intensity as a function of MPS concentration in the colloid. Previous studies of a neutral thiol, 1,2-benezenedithiol,[15] revealed a typical Langmuir adsorption behavior as a monotonic, exponential-like decay of the SH signal when the thiol concentration in the colloidal solution is increased. The SHS adsorption isotherm in the case of MPS is, however, dramatically different. The SH signal reduces by 56% as the bulk MPS concentration, [MPS], is initially increased from 0 to 0.12 μM. Further addition of [MPS] up to 1.0 μM induces no detectable quench in terms of the SH signal. However, when [MPS] is increased between ~1 and 10 μM, the SH intensity appears to decrease by another 22% of the total until saturation is finally approached. The total amount of SHS quench as the final adsorption equilibrium is about 78%.

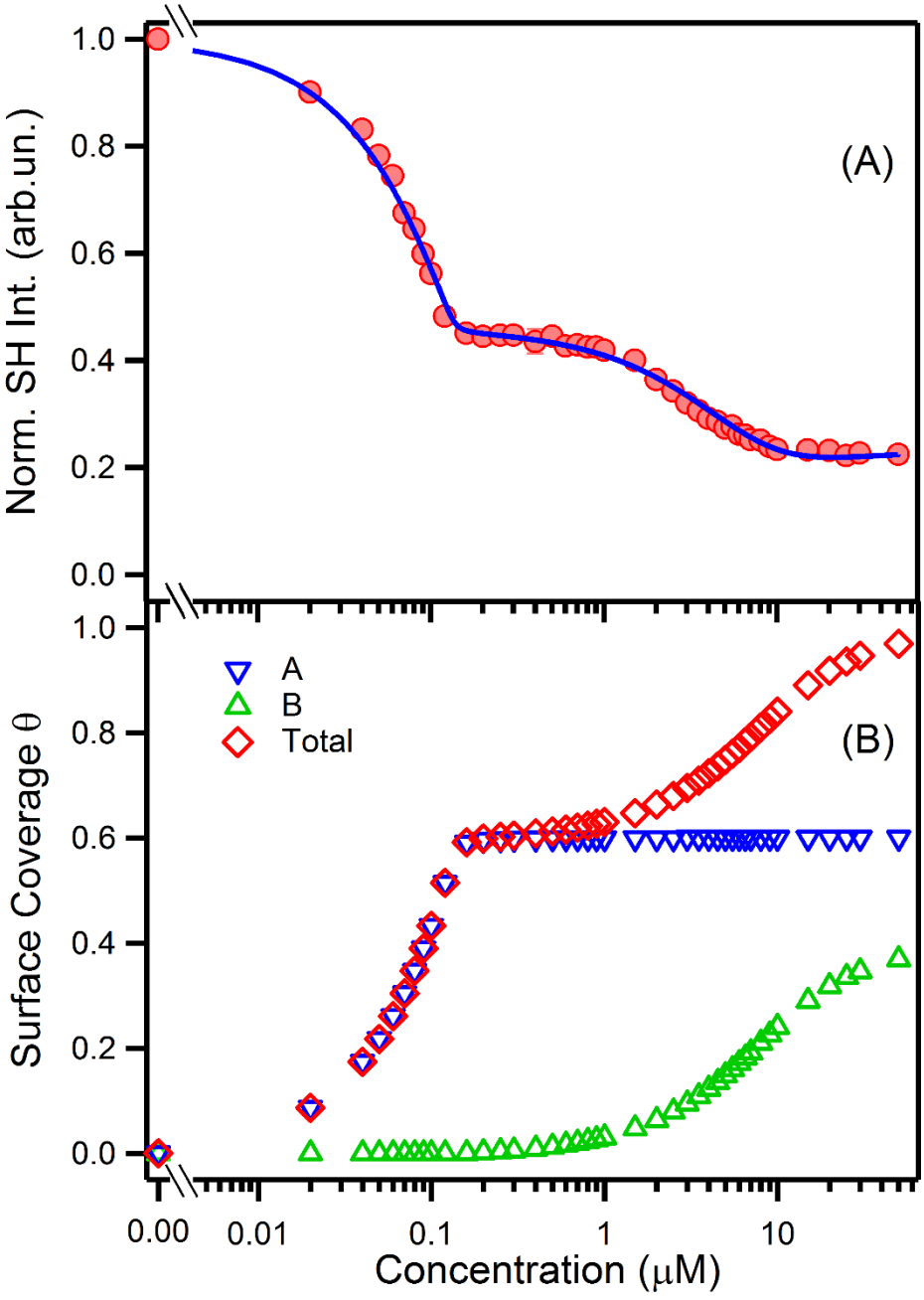

Figure 4.4 (A) The SHS intensity, set as unity for the intensity detected with no MPS, measured as a function of the MPS concentration, and (B) θ_A (blue), θ_B (green), and the total coverage θ (red) obtained from the best fit, shown in (A) as the solid line.

The observed behavior of the SH signal strongly suggests that the adsorption of MPS on the Ag NPs surface proceeds through a two-step mechanism as the surface MPS coverage changes in response to the MPS concentration.

4.3.2 Temperature-Dependent Time-Resolved Anionic Thiol Adsorption on Silver Nanoparticles

To verify the speculation that there are two steps in the adsorption process from the appearance of the adsorption isotherm, the kinetics associated with the MPS adsorption were examined at a set of temperatures. Time-resolved observation of the SH intensity, which can be quantitatively related to the thiol surface coverage, reflects the rate constants of the MPS adsorption onto Ag NPs. The temperature dependence of this adsorption rate constants allows the determination of activation energy of the adsorption reaction.

Fig. 4.5 shows the SH intensity response to the addition of fixed amounts of [MPS] as a function of time. Regardless of the temperature, generally, the SH signal from Ag NPs rapidly decays initially and then continues decreasing at a much slower rate. Compared to the neutral thiol adsorption, these measurements made over a wide range of temperatures are consistent with a two-stage mechanism for the adsorption of MPS.

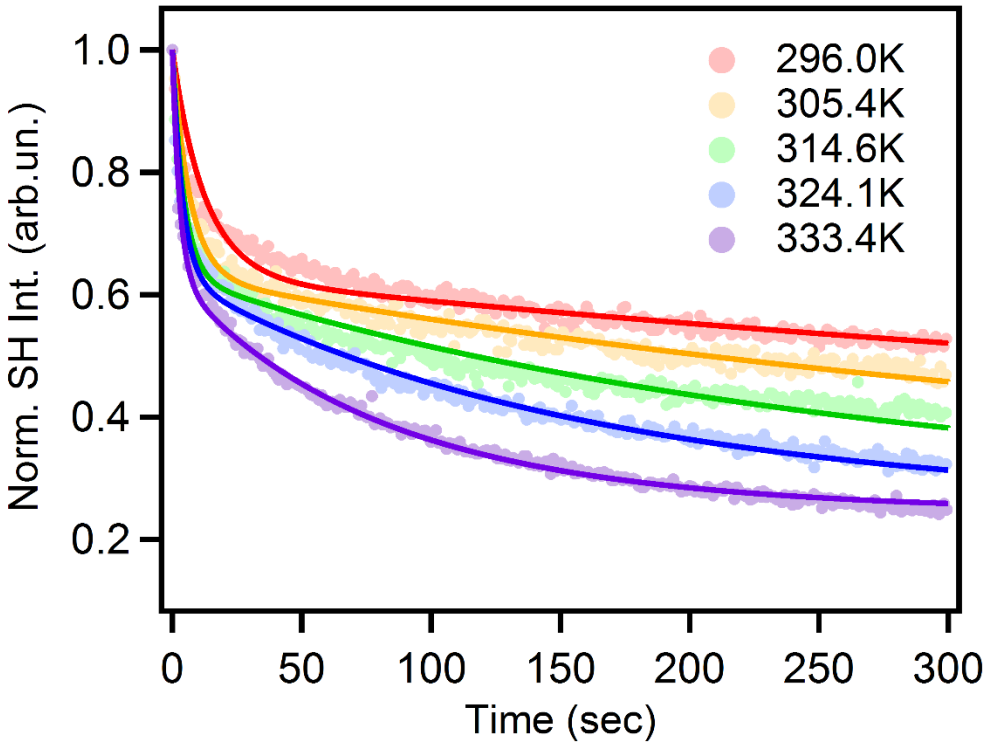

Figure 4.5 The SHS intensity, normalized to unity at t = 0, as a function of time following the addition of [MPS] = 50 μM at t = 0 recorded at the specified constant temperature: (red) 296.0±0.1, (yellow) 305.4±0.1, (green) 314.6±0.1, (blue) 324.1±0.1, and (purple) 333.4±0.1 K.

4.3.3 Effect of Citrate ion to Anionic Thiol Adsorption on Silver Nanoparticles

One important difference between colloidal systems and the more widely studied flat surfaces is the presence of the electrolytes in the solution because of the need to stabilize the particles in colloids. The Ag NPs synthesized through the conventional method carry a large amount of Cit ions at the surface, forming an electric double layer (EDL) that prevents the particles from aggregation. The Ag NPs appear to be negatively charged due to the anionic nature of Cit ions. Therefore, with respect to anionic thiol adsorption, it is important to understand the role of Cit in the MPS adsorption process. For instance, MPS adsorption has been found to be significantly slower than neutral thiols.[15]

For comparison, two Cit concentrations have been applied to stabilize the silver colloids: 30 μM, the one used to stabilize the Ag NPs in Fig. 4.4A, and 0.5 μM, at which the surface charge density of Ag NPs is expected to be lower. As illustrated in Figure 4.5A, ζ varies with the Cit concentration. At [Cit] = 30 μM, where the surface is saturated with Cit, ζ = -(32.9±0.6) mV before the MPS addition. For [Cit] = 0.5 μM, also without MPS, ζ = -(17.2±0.3) mV, reflecting less Cit on the particle surface.

The two silver colloidal samples with 30 μM and 0.5 μM of Cit ions have been employed for concentration-dependent experiments of MPS. Both zeta potential (ζ) and the SH intensity were measured for the adsorption isotherms. As for zeta potential measurements, beside an offset in the absolute values of ζ, the two sets of data as a function of [MPS] present very similar behavior. In the range of [MPS] = 0 to ~0.1 μM, ζ becomes more negative with [MPS]; for [MPS] higher than 0.1 μM, ζ fluctuates but appears unchanged until [MPS] > 5 μM where ζ starts shifting to more positive values. The behavior of the ζ value as a function of [MPS] mirrors the distinctions in the adsorption

isotherm in the three [MPS] regions. The Zeta potential results also suggest different adsorption behaviors in two regions, [MPS] below ~0.1 μM and higher than ~1 μM, consistent with SHS adsorption isotherms illustrated in Fig. 4.6B.

In our system, after dialysis, the ions existing in the solution (pH~6.6) are Na^+, Cit^{3-} and MPS^-. A one-to-one replacement of Cit^{3-} by MPS^- would produce a less negatively charged particle surface, while replacement of water with MPS^- will lead to an increase of the negative charges of the particle. In the low MPS concentration regime, i.e. the first adsorption phase, the zeta potential measurements indicate that the particle surface is becoming more negatively charged. It is therefore reasonable to conclude that the exchange between water and MPS^- dominates in this phase. As the coverage increases till most sites occupied by water are filled, exchange between Cit^{3-} and MPS^- dominates, the total surface charge becomes less negative.

The SHS adsorption isotherms are also shown in Fig. 4.6B for comparison. Interestingly, the two SHS adsorption isotherms appear to be essentially identical despite the substantial difference in the Cit concentration and in absolute values of ζ. At the two different Cit concentrations the surface Cit coverage is very different. But the surface coverages are very similar at a set of MPS concentrations. It indicates that concentration of Cit ions have no detectable effect on the thermodynamics of the anionic thiol adsorption at Ag NPs. This seems reasonable based on the fact that Cit is physisorbed and their presence does not significantly affect the silver-sulfur bonding, which is the origin of the decrease in the SHS signal. The same conclusions can be drawn for the less strongly bonded water at the surface.

The complete rate of adsorption is determined by both mass transfer and chemistry reaction at the surface. Thus, it is important to discover which one is the rate-determining step for the adsorption process. Our previous work rules out the diffusion-limited adsorption of 1,2-benzendithiol in colloidal system. On the other hand, one of the major differences between MPS and 1,2-benzendithiol is the negative charge carried by MPS, and consequently adsorption of MPS onto Ag NPs is under the influence of the EDL. It is natural to expect that the presence of EDL will slow down the diffusion process. However, by controlling the concentration of Cit and in turn tuning the surface charge, we observed no significant difference in the MPS adsorption kinetics (shown in Fig. 4.7). This result suggests that the rate-determining step for MPS adsorption is still the chemistry reaction.

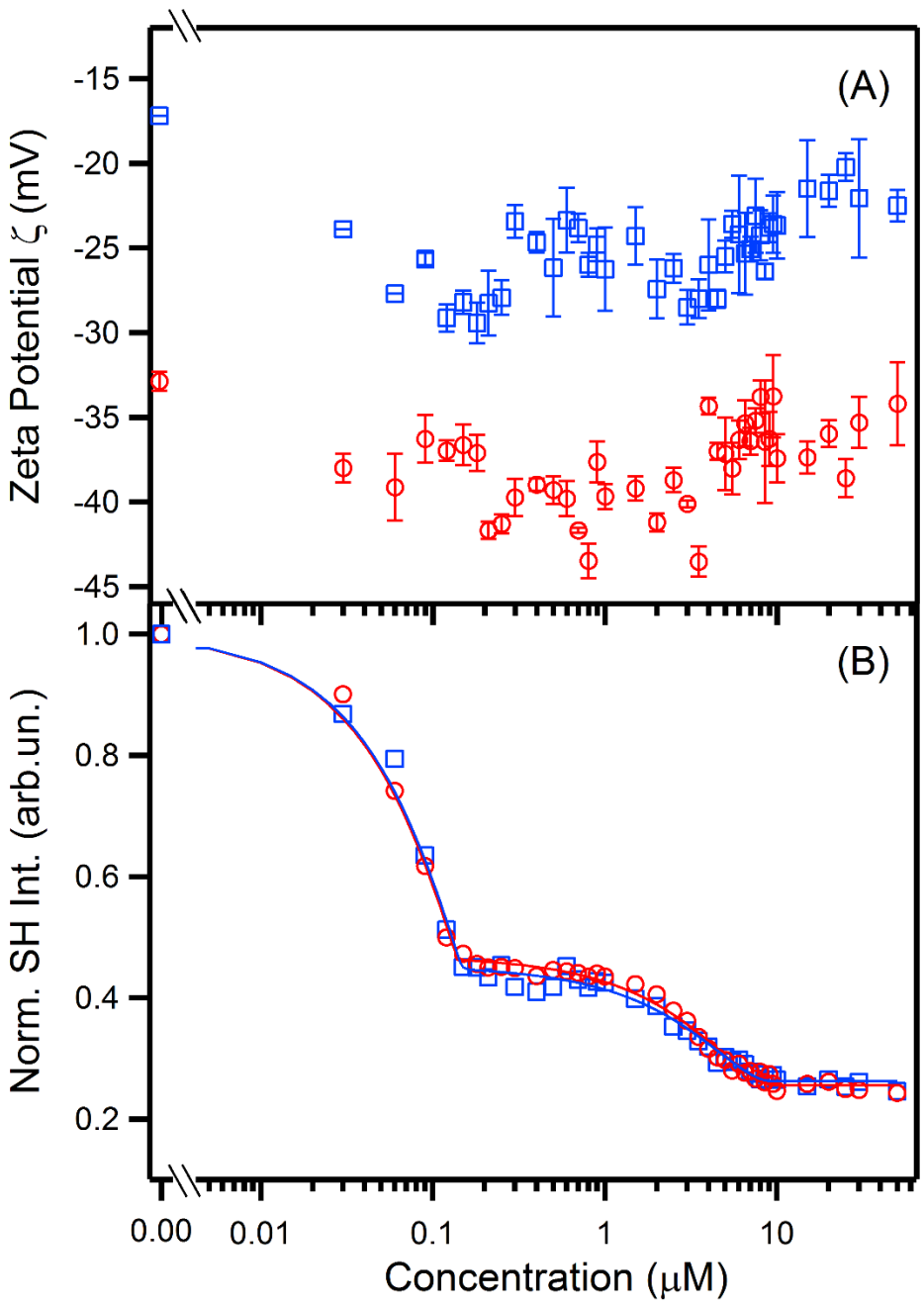

Figure 4.6 (A) Zeta potential (ζ) of the Ag NP colloidal solution measured as a function of the MPS concentration with the Cit concentration set at 0.5 μM (blue) and 30.0 μM (red); and (B) the corresponding SHS intensities (with the intensities measured for [MPS]=0 solutions set as unity).

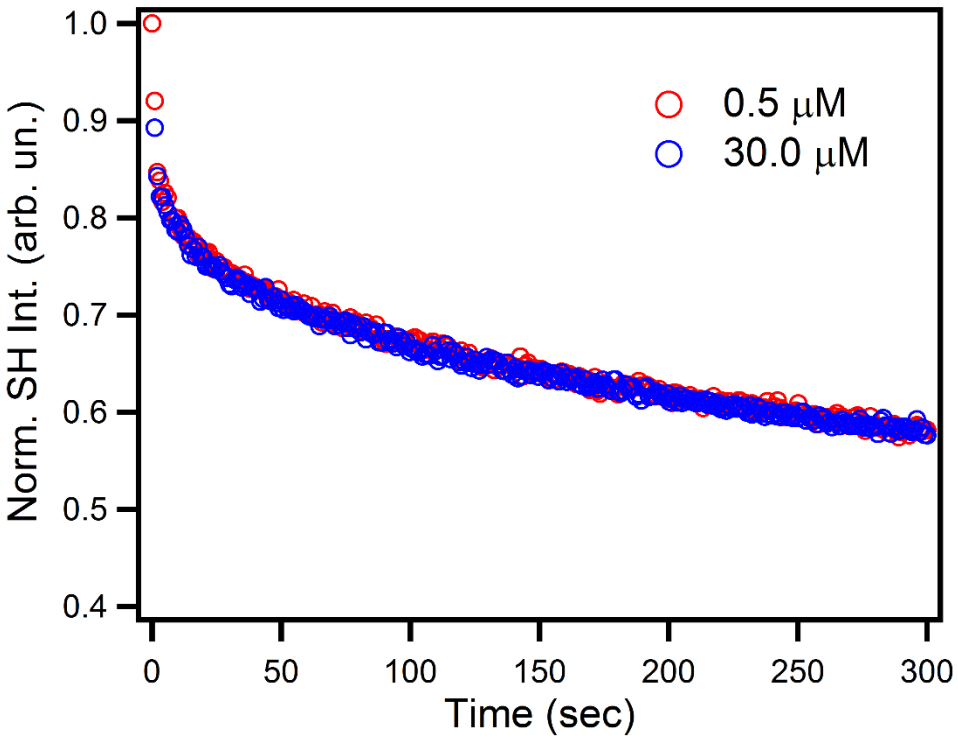

Figure 4.7 Normalized SHS intensity as a function of time after addition of [MPS]=50.0 μM to the Ag NPs solution at citrate concentration 0.5μM (red) and 30.0μM (blue). The experiment was done at room temperature.

4.3.4 Two-Step Model of Anionic Thiol Adsorption on Silver Nanoparticles

As the experimental results strongly suggest that the anionic thiols adsorb with two different mechanisms in different concentrations, we model the adsorption as a sum of two reactions, each associated with a specific site with its own adsorption characteristics – density, free energy, and activation energy:

$$T + ES_A \underset{}{\overset{K_A}{\rightleftharpoons}} TS_A \tag{4.1a}$$

$$T + ES_B \underset{}{\overset{K_B}{\rightleftharpoons}} TS_B \tag{4.1b}$$

In Eq. 4.1, MPS (T) adsorbs onto empty surface sites i (ES_i) on the Ag NP surface (where i=A, B), resulting in a MPS-occupied i site (TS_i). The relation between [MPS] and the amount of surface adsorbed thiol determined through the two adsorption reactions can be mathematically described using a modified Langmuir model. Here, the depletion of MPS in the bulk solution is taken into account.[13] The two equilibrium constants can be expressed as:

$$K_A = \frac{\theta_A N_{\max}}{N_{\max}(\theta_{A,\max} - \theta_A)(x - \theta N_{\max})} \tag{4.2a}$$

$$K_B = \frac{\theta_B N_{\max}}{N_{\max}(\theta_{B,\max} - \theta_A)(x - \theta N_{\max})} \tag{4.2b}$$

where x is the bulk concentration of MPS added into the colloidal solution, K_i is the equilibrium constants corresponding to the reactions in Eq. 4.1, $N_{\max}$ is the maximum number density of bonding sites available to MPS (including both A and B sites), and θ_i is the fraction of the i site covered by MPS ($\theta = \theta_A + \theta_B$), while $\theta_{i,\max}$ (with $\theta_{A,\max} + \theta_{B,\max} = 1$) is the maximum fraction of the i site when the surface is saturated.

Because the change in the surface nonlinear response of the Ag NPs is proportional to the surface coverage of thiols,[14-15, 30, 34-35] the SH intensity can be expressed as:

$$I(2\omega) \propto | \chi_{Ag} - \chi_Q(\theta_A + \theta_B)e^{i\phi} |^2 \tag{4.3}$$

where χ_{Ag} represents the susceptibility of the bare Ag NP (including surface and possibly bulk contributions[17]), χ_Q is the total decrease in surface susceptibility induced by thiol adsorption at the saturation coverage, and ϕ is the phase difference between the two susceptibilities.

With respect to observables in a time-dependent experiment, the rate equations below are used for their description:

$$\frac{d\theta_A}{dt} = k_{1,A}C(\theta_{A,\max} - \theta_A) - k_{-1,A}\theta_A \tag{4.4a}$$

$$\frac{d\theta_B}{dt} = k_{1,B}C(\theta_{B,\max} - \theta_B) - k_{-1,B}\theta_B \tag{4.4b}$$

where $k_{1,i}$ and $k_{-1,i}$ (i=A, B) are the rate constants for adsorption and desorption at the surface site i, respectively. C = [MPS] is a constant since at very high concentration depletion of the thiols in the solution due to surface adsorption is negligible. By solving Eq. 4.4, we obtain the analytical expression of the surface coverage θ_i as a function of time:

$$\theta_A = \Theta_A(1 - e^{-(k_{1,A}C + k_{-1,A})t}) \tag{4.5a}$$

$$\theta_B = \Theta_B(1 - e^{-(k_{1,B}C + k_{-1,B})t}) \tag{4.5b}$$

where Θ_i (i=A, B) is the final coverage for site i at [MPS] = C .

Given the fact that $k_{-1,i} \ll k_{1,i}$, $k_{-1,i}$ can be ignored, and it is thus possible to plot $k_{1,i}$ as a function of the reciprocal of temperature.

Eq. 4.3, after substituting from Eq. 4.2, can be used to fit the experimental SHS adsorption isotherm shown in Figure 4.3A. The parameters from a nonlinear least-squares fitting of the data, K and $\theta_{\max}N_{\max}$, together with some derived quantities, such as the Gibbs free energy change, ΔG_{ads}, and the molecular surface density defined as $\Gamma_{\max} = N_{\max}\theta_{\max} / (4\pi\overline{R}^2 n)$ (with $\overline{R}$ the average nanoparticle radius and n the particle density in the colloid) are listed in Table 4.1.

ΔG_{ads} for the A and the B site is -(14.3±0.3) kcal/mol and -(7.4±0.1) kcal/mol, respectively. Note the large difference in the two ΔG_{ads}, -6.9 kcal/mol, which can be attributed to the effects of electrostatic and steric repulsions in the two adsorption sites (see below).

The surface density of the A and the B sites at saturation coverage are (2.2± 0.2)×10^{14} MPS/cm^2 and (1.6± 0.2)×10^{14} MPS/cm^2, respectively. The calculated coverage θ_i, for both A and B sites, as well as the total coverage θ as a function of [MPS], calculated using the parameters from the fitting, are shown in Fig. 4.4B. Our calculation is based on the assumption that all Ag NPs have spherical shape with a diameter of 80 nm. In reality, however, TEM images indicate a polyhedral shape (see the TEM picture, Fig. 4.1) which has a surface to volume ratio higher than that of spheres. The size of the particles measured by dynamic light scattering (DLS) is (80±20) nm. Therefore, in our calculations we underestimate the total surface area of the particles and this, in turn, produces an overestimation of the surface coverage. This can explain why our $\Gamma_{Tot,\max} = \Gamma_{A,\max} + \Gamma_{B,\max}$ is larger than the value of 2.20×10^{14} molecules/cm^2 found for sodium 2-mercaptoethane sulfonate monolayer on rough Au thin film.[36] However, the value of $\Gamma_{Tot,\max}$ found for

MPS in this work is still smaller than that was reported for a densely packed SAM of ethanethiolate on Ag (111), namely 4.7×10^{14} molecules/cm^2,[37-38] and what our group previously obtained, namely 7×10^{14} molecules/cm^2, for 1,2-benzenedithiol on Ag NPs,[14] Note that both ethanethiol and 1,2-benezenedithiol are neutral molecules.

By the simultaneous fit of the time dependent SHS data in Fig. 4.4 with Eq. 4.3, after substituting for θ_i the expression in Eq. 4.5, it is possible to obtain $k_{1,i}$ at each temperature. $k_{1,i}$ as a function of the inverse of the absolute temperature can be analyzed using the Arrhenius equation (Fig. 4.8) for the determination of the activation energy of chemisorption to the A and the B site as (7.5±0.9) kcal/mol and (12.4±0.5) kcal/mol, respectively (Table 4.1).

Table 4.1 Parameters (θ_{max} N_{max}, K, E_a) extracted from the fitting and the derived quantities (Γ_{max}, ΔG_{ads})

	Site A	Site B
θ_{max} N_{max}	0.13 ± 0.01 μM	0.10 ± 0.01 μM
Γ_{max}	$(2.2 \pm 0.2)\times10^{14}$/cm^2	$(1.6 \pm 0.2)\times10^{14}$/cm^2
K	$(5.8 \pm 2.8)\times10^{10}$ M^{-1}	$(3.1 \pm 0.4)\times10^{5}$ M^{-1}
ΔG_{ads}	- (14.3 ± 0.3) kcal/mol	- (7.4 ± 0.1) kcal/mol
E_a	7.5 ± 0.9 kcal/mol	12.4 ± 0.5 kcal/mol

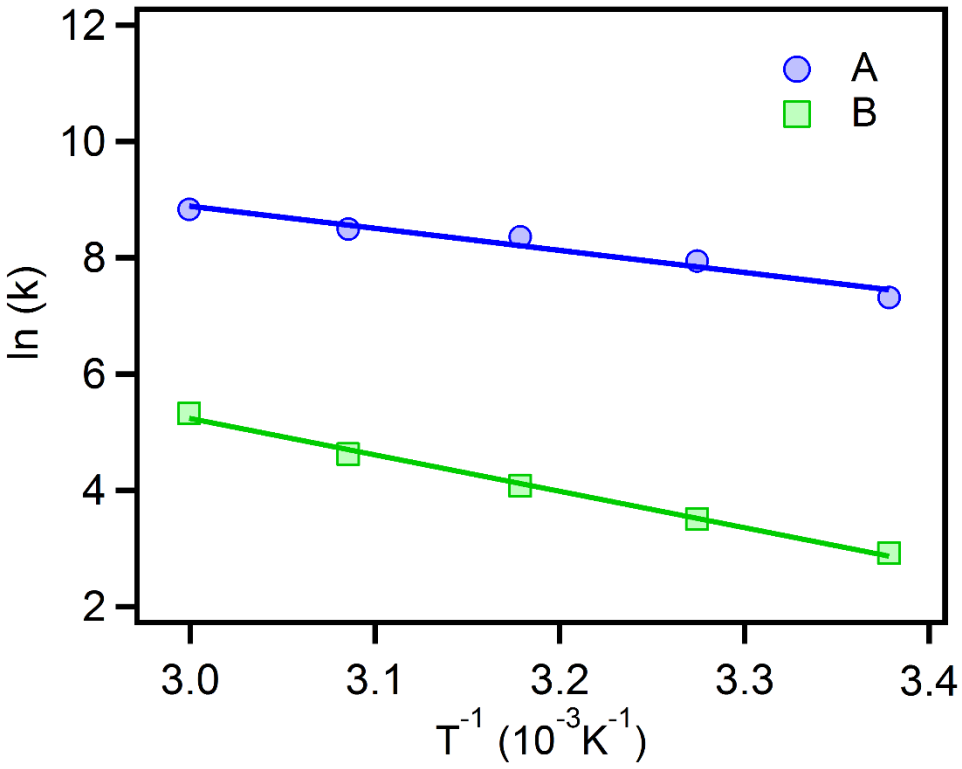

Figure 4.8 Arrhenius plot of the adsorption rate constants $k_{1,A}$ (blue) and $k_{1,B}$ (green).

It is important to note that the adsorption model proposed must be consistent with these observations: In the low MPS concentration regime the adsorption has a larger free energy (in magnitude) but smaller activation energy, and the particle surface is becoming more negatively charged. In the higher concentration regime, the 2nd stage, the free energy is smaller in magnitude but the activation energy becomes larger and the particle surface is less negatively charged. We propose a mechanism based on the effect of electrostatic repulsion by adsorbed charged thiols and the presence of the surfactant Cit at the particle surface.

The adsorption of n-alkanethiols on metal surfaces has been studied both in ultra-high vacuum[8, 39] and in solution[40-42] conditions. In a solution, adsorption is proposed to occur through a sequence of steps: (i) physisorption with displacement of original surfactants off the surface, (ii) formation, in the absence of strong hydrophobic effects and lateral chain interactions, of disordered sub monolayers at low coverage, and finally, (iii) the increase in coverage induces a rapid increase in intermolecular interactions, and eventually leads to a formation of a highly ordered full monolayer.[8] The MPS we are using here has short chain length with a negatively-charged terminus. The intermolecular interaction of n-alkanethiolates (charged) is expected to be different from the shorter chain n-alkanethiols. Because of the amphiphilic nature of n-alkanethiolates, the intermolecular interaction includes both attractive (i.e. lateral forces between hydrocarbon chains) and repulsive (i.e. sulfonate endgroup repulsion) forces. Depending on the coverage, further adsorption of thiols is either favored when attraction forces dominate, or disfavored when repulsion dominates.[37-38] Consequently, we propose a different adsorption mechanism for MPS. MPS has a short chain (n=3) and intense repulsive interaction: The sulfonate endgroup provides not only a long-range electrostatic repulsion, but also a short-range steric repulsion.[36]

The nearly constant SH signal observed for the range 0.12 μM<[MPS]<1.0 μM, in between the two adsorption regimes, can be best understand as that the MPS adsorption on the Ag NPs comes to a halt because the molecules have to overcome a large energy barrier compared to what is required at lower coverage to bind to the Ag NP surface. We thus postulate that the intermolecular repulsion is the origin of such barrier.[37-38, 43] The model,

schematically depicted in Fig. 4.9, reflects the evolution of the surface environment upon the adsorption of short-chain, negatively charged thiol molecules.

The presence of a negatively charged thiol chemisorbed to the Ag NP surface will affect the nearby environment for an incoming thiol molecule which also has negative charge. At low coverage, charged thiols may produce sufficient distance among them to reduce the repulsive interaction. Binding of charged thiols occurs as in A sites in Fig. 4.9. At low thiol concentration in solution, the surface coverage builds up until the critical coverage where the intermolecular repulsion prevents further adsorption. As the MPS concentration in solution further increases to above a higher critical value, sufficient driving force is generated and further surface adsorption on B sites occurs.

The Gibbs free energy change (ΔG) for charged thiol adsorption on metal surfaces in aqueous solution is affected by its solvation in the liquid, the intermolecular interactions which have both attractive and repulsive contributions, and the formation of the metal-S bond.[6, 9, 38] In addition, displacement of surfactants (water, Cit, etc.), in principle, also contributes to ΔG. In contrast, the activation energy is associated with the particular step that contributes most to the energy barrier for the chemisorption process.

At low coverage, where the interaction among adsorbed MPS molecules is negligible, ΔG is dominated by the energy of formation of the silver-sulfur bond. Subsequently, the magnitude of the free energy is larger. On the assumption that the major contribution to the activation energy is from the repulsion between the charges of the adsorbed and the incoming thiol, the activation energy is relatively low as the intermolecular distance can be long.

When the surface coverage is higher, intermolecular interactions have to be taken into account. It is reasonable to anticipate that the repulsion is larger than the attraction at the higher coverage. Comparing with sites A, sites B's free energy magnitude will be smaller. The reduction in $|\Delta G_{ads}|$ between A and B sites by 6.9 kcal/mol represents the contribution from the repulsive interactions, i.e. the sum of electrostatic and steric repulsions minus the change induced by the increased concentration of MPS in the solution. In contrast, the repulsion will cause the activation energy to be higher (increase from 7.5±0.9 to 12.4±0.5 kcal/mol) as it prevents the incoming charged thiol molecule getting close to the surface for the bond formation.

The measured relative values of the adsorption free energy and the activation energy are consistent with the proposed model. It should also be pointed out that the adsorption of MPS on the particle surface does not deplete the nearby thiols in the solution, at least for the higher concentrations, so that diffusion is not the rate-determining step and not the source of the activation energy.[15] The activation energy for the neutral 1,2-benezenedithiol on Ag NPs was previously found to be (8.4±0.3) kcal/mol.[15] The adsorption of decanethiol on Au(111) from ethanol has been reported to have an activation energy of 7.1 kcal/mol,[44] while an activation energy of 6.9 kcal/mol has been observed for several alkanethiol groups on Au(111) in ultrahigh vacuum conditions.[45] All these results are comparable to our activation energy associated with the site A, 7.5±0.9 kcal/mol. As discussed above, at low coverage where the binding to A sites dominates, the interaction between MPS molecules has no effect on the adsorption of incoming molecules, and hence the activation energy is mainly attributed to the silver-sulfur bond formation process, similar to the neutral thiol cases.

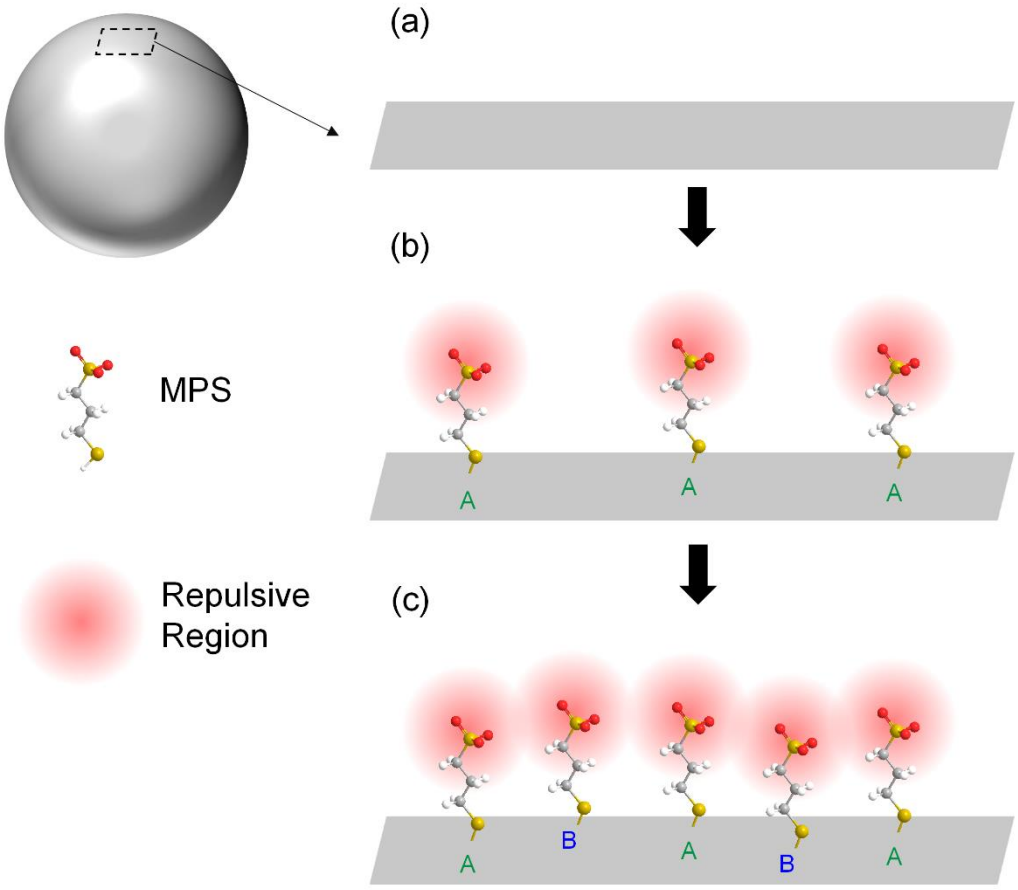

Figure 4.9 Schematic representation of the two-stage adsorption of MPS on Ag NPs surface.

4.4 Summary

In summary, the surface sensitive second-order nonlinear optical technique, second harmonic scattering, has enabled the characterization of the chemisorption of negatively charged thiol molecule MPS on the surface of Ag colloidal nanoparticles. It is found that the chemisorption of this charged thiol occurs in two different regimes of concentrations, in contrast to the neutral thiols which display only monotonic concentration dependence. This two-step adsorption is primarily a result of the charge-charge repulsion among the anionic thiols adsorbed on or near the surface. At low MPS concentration (below 0.1 μM), a low coverage of the charged thiols can adsorb onto the surface. The repulsion among adsorbed MPS molecules is small so that the activation energy (7.5±0.9 kcal/mol) is lower and the magnitude of the free energy of adsorption (-14.3±0.3 kcal/mol), dominated by the energy of formation of the Ag-S bond, is relatively large. The adsorbed thiols do not displace the Cit ions physisorbed on the surface, so the particle becomes more negatively charged. The adsorption of thiols stops when the coverage becomes sufficiently high so that the inter-thiol repulsion prohibits further adsorption. As the concentration increases to above 1 μM, sufficient driving force is built up to overcome the inter-thiol repulsion and chemisorption continues. Here due to increased repulsion the activation energy is bigger (12.4±0.5 kcal/mol) and the magnitude of the free energy change (-7.4±0.1 kcal/mol) is smaller. As the thiols replace the more negatively charged Cit, the particle becomes less negatively charged. This study illustrates the importance of Coulombic interactions in the chemisorption of charged thiols on metallic nanoparticles.

4.5 Bibliography

1. Nanoparticles : Building Blocks for Nanotechnology. Rotello, V. M., Ed. Kluwer Academic/Plenum Publishers: New York :, 2004.
2. Daniel, M.-C.; Astruc, D., Gold Nanoparticles: Assembly, Supramolecular Chemistry, Quantum-Size-Related Properties, and Applications toward Biology, Catalysis, and Nanotechnology. *Chem. Rev.* **2003,** *104* (1), 293-346.
3. Mayer, K. M.; Hafner, J. H., Localized Surface Plasmon Resonance Sensors. *Chem. Rev.* **2011,** *111* (6), 3828-3857.
4. Crudden, C. M.; Horton, J. H.; Ebralidze, I. I.; Zenkina, O. V.; McLean, A. B.; Drevniok, B.; She, Z.; Kraatz, H.-B.; Mosey, N. J.; Seki, T.; Keske, E. C.; Leake, J. D.; Rousina-Webb, A.; Wu, G., Ultra Stable Self-Assembled Monolayers of N-Heterocyclic Carbenes on Gold. *Nat. Chem.* **2014,** *6* (5), 409-414.
5. Weidner, T.; Baio, J.; Mundstock, A.; Grosse, C.; Karthauser, S.; Bruhn, C.; Siemeling, U., Nhc-Based Self-Assembled Monolayers on Solid Gold Substrates. *Aust. J. Chem.* **2011,** *64* (8), 1177-1179.
6. Love, J. C.; Estroff, L. A.; Kriebel, J. K.; Nuzzo, R. G.; Whitesides, G. M., Self-Assembled Monolayers of Thiolates on Metals as a Form of Nanotechnology. *Chem. Rev.* **2005,** *105* (4), 1103-1170.
7. Nuzzo, R. G.; Allara, D. L., Adsorption of Bifunctional Organic Disulfides on Gold Surfaces. *J. Am. Chem. Soc.* **1983,** *105* (13), 4481-4483.
8. Schreiber, F., Structure and Growth of Self-Assembling Monolayers. *Prog. Surf. Sci.* **2000,** *65* (5–8), 151-257.

9. Ulman, A., Formation and Structure of Self-Assembled Monolayers. *Chem. Rev.* **1996,** *96* (4), 1533-1554.

10. Stewart, A.; Zheng, S.; McCourt, M. R.; Bell, S. E. J., Controlling Assembly of Mixed Thiol Monolayers on Silver Nanoparticles to Tune Their Surface Properties. *ACS Nano* **2012,** *6* (5), 3718-3726.

11. Volkert, A. A.; Subramaniam, V.; Ivanov, M. R.; Goodman, A. M.; Haes, A. J., Salt-Mediated Self-Assembly of Thioctic Acid on Gold Nanoparticles. *ACS Nano* **2011,** *5* (6), 4570-4580.

12. Yoshida, A.; Yonezawa, Y.; Kometani, N., Tuning of the Spectroscopic Properties of Composite Nanoparticles by the Insertion of a Spacer Layer: Effect of Exciton−Plasmon Coupling. *Langmuir* **2009,** *25* (12), 6683-6689.

13. Wang, H.; Yan, E. C. Y.; Borguet, E.; Eisenthal, K. B., Second Harmonic Generation from the Surface of Centrosymmetric Particles in Bulk Solution. *Chem. Phys. Lett.* **1996,** *259* (1–2), 15-20.

14. Gan, W.; Gonella, G.; Zhang, M.; Dai, H.-L., Reactions and Adsorption at the Surface of Silver Nanoparticles Probed by Second Harmonic Generation. *J. Chem. Phys.* **2011,** *134* (4).

15. Gan, W.; Xu, B.; Dai, H.-L., Activation of Thiols at a Silver Nanoparticle Surface. *Angew. Chem. Int. Edit.* **2011,** *50* (29), 6622-6625.

16. Gonella, G.; Dai, H.-L., Second Harmonic Light Scattering from the Surface of Colloidal Objects: Theory and Applications. *Langmuir* **2013,** *30* (10), 2588-2599.

17. Gonella, G.; Gan, W.; Xu, B.; Dai, H.-L., The Effect of Composition, Morphology, and Susceptibility on Nonlinear Light Scattering from Metallic and Dielectric Nanoparticles. *J. Phys. Chem. Lett.* **2012,** *3* (19), 2877-2881.

18. Jen, S.-H.; Dai, H.-L., Probing Molecules Adsorbed at the Surface of Nanometer Colloidal Particles by Optical Second-Harmonic Generation. *J. Phys. Chem. B* **2006,** *110* (46), 23000-23003.

19. Jen, S.-H.; Gonella, G.; Dai, H.-L., The Effect of Particle Size in Second Harmonic Generation from the Surface of Spherical Colloidal Particles. I: Experimental Observations†. *J. Phys. Chem. A* **2009,** *113* (16), 4758-4762.

20. Ray, P. C., Size and Shape Dependent Second Order Nonlinear Optical Properties of Nanomaterials and Their Application in Biological and Chemical Sensing. *Chem. Rev.* **2010,** *110* (9), 5332-5365.

21. Brevet, P. F., Second Harmonic Generation in Nanostructures. In *Handbook of Nanoscale Optics and Electronics*, 1st ed.; Wiederrecht, G. P., Ed. Elsevier: Amsterdam ; Boston, 2010; pp 77-105.

22. Eisenthal, K. B., Second Harmonic Spectroscopy of Aqueous Nano- and Microparticle Interfaces. *Chem. Rev.* **2006,** *106* (4), 1462-1477.

23. Gomopoulos, N.; Lütgebaucks, C.; Sun, Q.; Macias-Romero, C.; Roke, S., Label-Free Second Harmonic and Hyper Rayleigh Scattering with High Efficiency. *Opt. Express* **2013,** *21* (1), 815-821.

24. Roke, S.; Gonella, G., Nonlinear Light Scattering and Spectroscopy of Particles and Droplets in Liquids. *Annu. Rev. Phys. Chem.* **2012,** *63* (1), 353-378.

25. Corn, R. M.; Higgins, D. A., Optical Second Harmonic Generation as a Probe of Surface Chemistry. *Chem. Rev.* **1994,** *94* (1), 107-125.

26. Dounce, S. M.; Yang, M.; Dai, H.-L., Physisorption on a Metal Surface Probed by Surface State Resonant Second Harmonic Generation. *Surf. Sci.* **2004,** *565* (1), 27-36.

27. Heskett, D.; Urbach, L. E.; Song, K. J.; Plummer, E. W.; Dai, H. L., Oxygen and Pyridine on Ag(110) Studied by Second Harmonic Generation: Coexistence of Two Phases within Monolayer Pyridine Coverage. *Surf. Sci.* **1988,** *197* (1–2), 225-238.

28. Camillone, N., Diffusion-Limited Thiol Adsorption on the Gold(111) Surface. *Langmuir* **2004,** *20* (4), 1199-1206.

29. Karpovich, D. S.; Blanchard, G. J., Direct Measurement of the Adsorption Kinetics of Alkanethiolate Self-Assembled Monolayers on a Microcrystalline Gold Surface. *Langmuir* **1994,** *10* (9), 3315-3322.

30. Dannenberger, O.; Buck, M.; Grunze, M., Self-Assembly of N-Alkanethiols: A Kinetic Study by Second Harmonic Generation. *J. Phys. Chem. B* **1999,** *103* (12), 2202-2213.

31. Guthrie, J. P., Hydrolysis of Esters of Oxy Acids: Pka Values for Strong Acids; Brønsted Relationship for Attack of Water at Methyl; Free Energies of Hydrolysis of Esters of Oxy Acids; and a Linear Relationship between Free Energy of Hydrolysis and Pka Holding over a Range of 20 Pk Units. *Can. J. Chemistry* **1978,** *56* (17), 2342-2354.

32. Campen, R. K.; Pymer, A. K.; Nihonyanagi, S.; Borguet, E., Linking Surface Potential and Deprotonation in Nanoporous Silica: Second Harmonic Generation and Acid/Base Titration. *J. Phys. Chem. C* **2010,** *114* (43), 18465-18473.

33. Lee, P. C.; Meisel, D., Adsorption and Surface-Enhanced Raman of Dyes on Silver and Gold Sols. *J. Phys. Chem.* **1982,** *86* (17), 3391-3395.

34. Campen, R. K.; Zheng, D.-s.; Wang, H.-f.; Borguet, E., Second Harmonic Generation as a Probe of Multisite Adsorption at Solid−Liquid Interfaces of Aqueous Colloid Suspensions†. *J. Phys. Chem. C* **2007,** *111* (25), 8805-8813.

35. Wang, H. F.; Yan, E. C. Y.; Liu, Y.; Eisenthal, K. B., Energetics and Population of Molecules at Microscopic Liquid and Solid Surfaces. *J. Phys. Chem. B* **1998,** *102* (23), 4446-50.

36. Rouhana, L. L.; Moussallem, M. D.; Schlenoff, J. B., Adsorption of Short-Chain Thiols and Disulfides onto Gold under Defined Mass Transport Conditions: Coverage, Kinetics, and Mechanism. *J. Am. Chem. Soc.* **2011,** *133* (40), 16080-16091.

37. Hatchett, D. W.; Stevenson, K. J.; Lacy, W. B.; Harris, J. M.; White, H. S., Electrochemical Oxidative Adsorption of Ethanethiolate on Ag(111). *J. Am. Chem. Soc.* **1997,** *119* (28), 6596-6606.

38. Hatchett, D. W.; Uibel, R. H.; Stevenson, K. J.; Harris, J. M.; White, H. S., Electrochemical Measurement of the Free Energy of Adsorption of N-Alkanethiolates at Ag(111). *J. Am. Chem. Soc.* **1998,** *120* (5), 1062-1069.

39. Schreiber, F.; Eberhardt, A.; Leung, T. Y. B.; Schwartz, P.; Wetterer, S. M.; Lavrich, D. J.; Berman, L.; Fenter, P.; Eisenberger, P.; Scoles, G., Adsorption

Mechanisms, Structures, and Growth Regimes of an Archetypal Self-Assembling System: Decanethiol on Au(111). *Phys. Rev. B* **1998,** *57* (19), 12476-12481.

40. Bain, C. D.; Troughton, E. B.; Tao, Y. T.; Evall, J.; Whitesides, G. M.; Nuzzo, R. G., Formation of Monolayer Films by the Spontaneous Assembly of Organic Thiols from Solution onto Gold. *J. Am. Chem. Soc.* **1989,** *111* (1), 321-335.

41. Laibinis, P. E.; Whitesides, G. M.; Allara, D. L.; Tao, Y. T.; Parikh, A. N.; Nuzzo, R. G., Comparison of the Structures and Wetting Properties of Self-Assembled Monolayers of N-Alkanethiols on the Coinage Metal Surfaces, Copper, Silver, and Gold. *J. Am. Chem. Soc.* **1991,** *113* (19), 7152-7167.

42. Schlenoff, J. B.; Li, M.; Ly, H., Stability and Self-Exchange in Alkanethiol Monolayers. *J. Am. Chem. Soc.* **1995,** *117* (50), 12528-12536.

43. Calvente, J. J.; Kováčová, Z.; Sanchez, M. D.; Andreu, R.; Fawcett, W. R., Desorption of Spontaneously Adsorbed and Electrochemically Readsorbed 2-Mercaptoethanesulfonate on Au(111). *Langmuir* **1996,** *12* (23), 5696-5703.

44. Han, Y.; Uosaki, K., Effects of Concentration and Temperature on the Formation Process of Decanethiol Self-Assembled Monolayer on Au(111) Followed by Electrochemical Reductive Desorption. *Electrochim. Acta* **2008,** *53* (21), 6196-6201.

45. Lavrich, D. J.; Wetterer, S. M.; Bernasek, S. L.; Scoles, G., Physisorption and Chemisorption of Alkanethiols and Alkyl Sulfides on Au(111). *J. Phys. Chem. B* **1998,** *102* (18), 3456-3465.

CHAPTER 5

POLARIZED LINEAR ABSORPTION IN MICRO-SIZED ULTRATHIN CRYSTALLINE PENTACENE

5.1 Introduction

Organic semiconductors have attracted considerable attention with respect to their current and potential applications in photonics and electronics.[1-6] The rapid growth of researches focus on π-conjugated materials in which a rich variety of new concepts have been uncovered. It is realized that π-conjugated materials possess the photovoltaic properties that are in some ways fundamentally different from that of inorganic semiconductors.[1, 6-7] For instance, upon photoexcitation, the excited electron and hole from a molecule will not intrinsically separate from each other. Instead, they tend to form a neutral quasi-particle, namely exciton, in which the electron and hole are attracted by the strong Coulombic force thanks to the low dielectric constants of organic materials. The mobility of excitons in organic materials, due to the neutral nature, differs from that of free carriers in inorganic semiconductors.[6-7] To realize the potential of organic semiconductors requires fundamental understanding of the physical, chemical, electronic and photovoltaic properties.

Among a number of candidates, the oligoacene series, such as tetracene, petacene, hexcene (see Fig. 5.1), as well as their derivatives, have been intensively studied.[1, 3, 8] Their exceptionally high charge mobilities have been reported, generating interest for applications such as field-effect transistor.[3, 9-10] More recently, the oligoacenes have also been under great scrutiny for their ability to promote singlet fission, which potentially

increases the energy conversion efficiency of solar cells.[2, 11-14] The phenomenon, singlet fission (SF), was first discovered in 1965 from the photophysical study of crystalline anthrancene, a member of the oligoacene series.[15] The SF process involves two neighboring molecules: an organic chromophore that is excited to the singlet state after absorbing one photon interacts with its adjacent ground-state molecule and ultimately convert both molecules to the triplet excited states. Hence, in SF, one photon absorbed eventually leads to two excited excitons in organic semiconductors, giving rise to the possibility for breaking up the Shockley–Queisser limit, in which the maximum solar efficiency for single p-n junction is about 33.7%.[11, 16]

Given the importance of the oligoacene-based organic semiconductors, we seek to employ the optical spectroscopic methods to study their excitonic properties as well as the SF mechanism. It is generally accepted that the peculiar excitonic properties of oligoacenes are responsible for their electronic and photovoltaic behaviors. Therefore, in this chapter, our goal is to link the steady-state electronic absorption spectra of oligoacenes with their excitonic compositions of photoexcited Frenkel and charge transfer (CT) excitons from both experimental and theoretical perspectives. The knowledge regarding the low energy exciton states of oligoacenes, in return, facilitate our research for the fundamental understanding of the SF process, especially about the potential role of the intermediate CT states.[11, 17] Direct observations of the SF process, on the other hand, require implementations of ultrafast time-resolved techniques, such as ultrafast transient absorption. A detailed discussion about the SF mechanism will be presented in the following chapter.

Aside from the large π-conjugated nature of oligoacenes, their molecular order and tight packing play a critical role in the electronic and photophysical properties of the oligoacene-based organic semiconductors, given the fact that the exciton mobility and SF both rely on the strong coupling between neighboring molecules.[2, 6, 11, 18] For this reason, oligoacenes in the forms of thin films, polycrystalline crystals as well as single crystals are the most commonly-used systems. Thus, we have chosen crystalline pentacene and hexacene for our researches. There are several reasons for using pentacene and hexacene in the form of single crystals: 1) both possess remarkable excitonic properties, such as high crystal-phase charge mobilities, [3, 9-10] 2) both are exoenergic in term of SF, that is the excitation energy of a singlet state is higher than two of the triplet states, i.e. $E(S_1)>2E(T_1)$, and therefore are energetically favored for SF,[8, 11] 3) compared to thin films and polycrystallines, single crystals present well-defined crystal structures and fewer defects,[19] 4) the anisotropic nature of the crystal structures provide an additional dimension for the analysis of the photophysics and the SF mechanism.

Despite the advantages granted to the use of single crystals, a relatively small number of optical spectroscopic studies have been reported.[20-22] It has to be noticed that, although the new progress of modern physical methods has made it not difficult to grow pentacene and hexacene single crystals with dimensions larger than 1mm, it remains an experimental challenge for a direct optical measurement in the transmission geometry. For example, due to the high absorption coefficients of pentacene and hexacene, the optimal thickness of the single crystals for the acquisition of the transmission UV-Vis absorption spectrum is about 100-500 nm. For large single crystals, only light reflection or ellipsometry measurement can be performed,[8, 23-26] and the extraction of the linear optical

absorbance requires certain models for post data analysis. In our experiments, instead, ultrathin single crystals of pentacene and hexacene have been studied, in which the conventional UV-Vis spectrometer fails because of the small size (<100 μm^2).

To solve the problem, in this chapter, we present an experimental setup we developed that uses a home-built optical microscope for selecting and positioning the single crystal samples. Transmission polarized UV-Vis absorption measurements can be conducted by coupling the microscope with a UV-Vis spectrometer. In this manner, the polarized spectra along two crystallographic axes of pentacene single crystals have been obtained. We observed significant difference between line shapes of the two spectra as well as a pronounced Davydov splitting (DS) of ≈1000 cm^{-1}, both of which are direct evidence of the anisotropic nature of crystalline pentacene. To investigate the excitonic compositions of pentacene single crystals, we collaborated with Dr. Spano, whose theoretical calculation unveils the important role of CT excitons in the lineshapes and the DS.

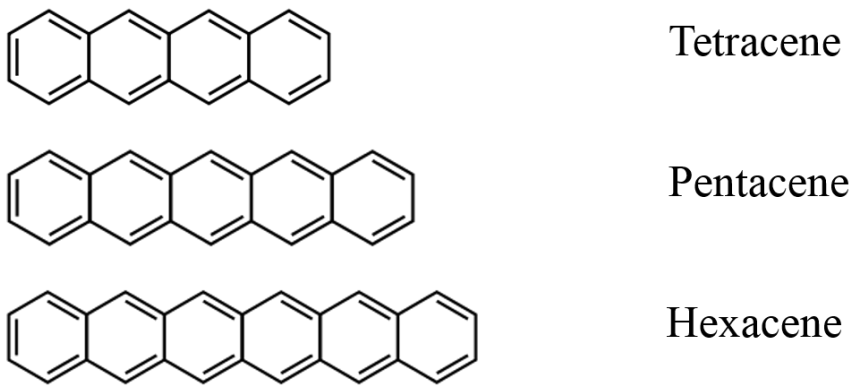

Figure 5.1 Molecular structures of tetracene, pentacene and hexacene.

5.2 Experiment

5.2.1 Experimental Setup

The experimental setup for the microscopic linear absorption is displayed in Fig. 5.2. The home-built microscope is illustrated in the dot-squared area. Basically, the incoming light from an incoherent broadband halogen-lamp (Lumina-I) was focused on the chosen sample at normal incident angle by an objective with x10 magnification. The sample substrate was mounted on a 3-axis (x, y, z) manual stage so that the position can be precisely adjustable. The transmitted light through the sample was collected by an 1-inch lens and subsequently delivered into the spectrometer (Andor Shamrock 500 with a grating blazed at 500nm, 150 groove/mm) equipped with a thermo-cooled CCD (Andor Newton). A LED pen was used to illuminate the sample substrate by collimating its light with the incoming excitation light through a beam splitter (Thorlabs). The reflected light from the samples went through the same alignment of the incident light but in the opposite direction. It was later reflected by another beam splitter (Thorlabs) and imaged in a CMOS camera (Thorlabs), where the sample position and the sample size was recorded.

As for polarization dependent experiments, a broadband polarizer (Thorlabs) was placed after the lamp to control the polarization of the excitation light. The linear absorption spectrum were collected by measuring the transmission light on and off the sample ($I_{on}(\lambda,\theta)$ and $I_{off}(\lambda,\theta)$) at given polarization angle (θ). Besides, the background light ($I_{bg}(\lambda)$) was also recorded by blocking the incident light. As a function of the polarization angle (θ), each spectrum was measured and calculated as,

$$A(\lambda,\theta) = \log_{10}[\frac{I_{off}(\lambda,\theta) - I_{bg}(\lambda)}{I_{on}(\lambda,\theta) - I_{bg}(\lambda)}] \tag{5.1}$$

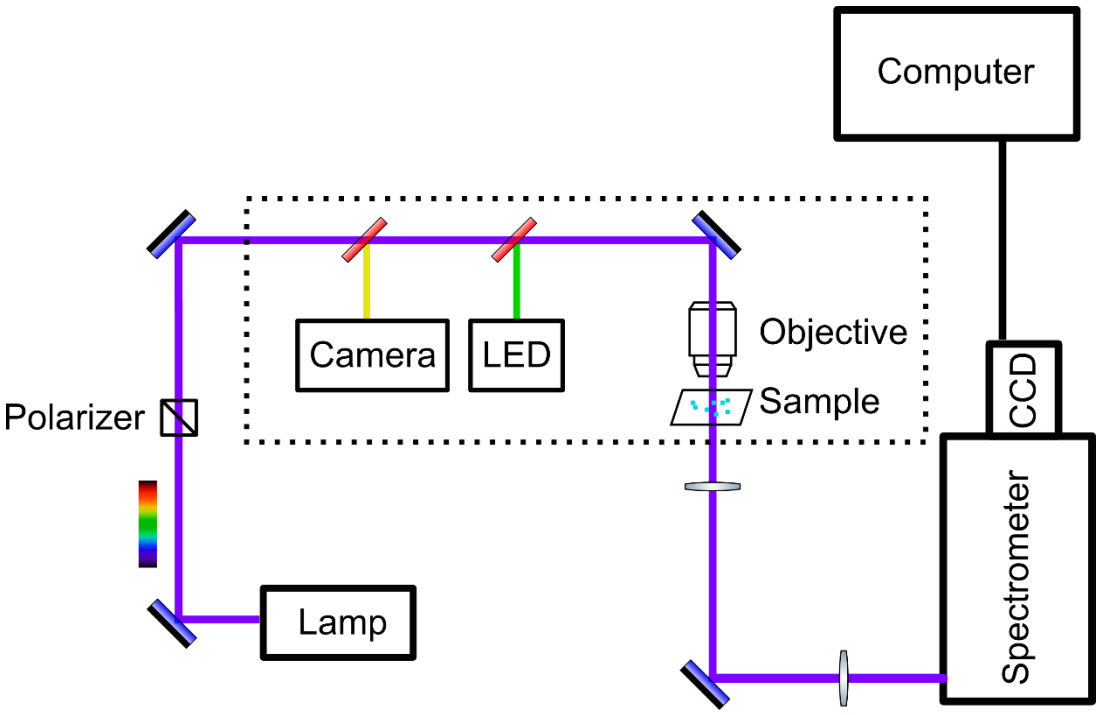

Figure 5.2. Schematic of the microscopic linear absorption spectrometer.

5.2.2 Sample Preparation

Pentacene single crystals were grown in a physical vapor transport (PVT) furnace[27] at atmospheric pressure. 8 mg of pentacene powder (Sigma Aldrich, triple-sublimed grade, ≥ 99.995 %) was heated in a hot zone of the furnace (320 °C) for one week. 50 SCCM of ultrahigh purity argon gas (99.999%) was used as purging gas as well as carrier gas. Crystalline pentacene were collected in the crystallization zone (260-280 °C). Grown in this manner, the pentacene crystal face (001) tends to be parallel to the substrate.[24] The collected pentacene single crystals were later spread on a quartz substrate, which was

subsequently sealed in a gasket container in a N_2 box to protect the single crystals from oxygen during the optical experiments. All experiments were conducted at room temperature.

The crystalline pentacene sample used in the experiment is shown in Fig. 5.3A. Based on the Beer's law, in which the extinction coefficient α=75000 cm^{-1} at 670 nm was from the literature,[24] the thickness was estimated as,

$$l = \frac{OD}{\alpha} = \frac{1.05}{7.5 \times 10^4} = 1.4 \times 10^{-5}\text{cm} = 140\text{nm} \tag{5.2}$$

Pentacene single crystal belongs to triclinic lattice system. Its unit cell parameters are listed in Table 5.1, in which the *b*-axis is defined as the direction that connects the nearest-neighboring molecules.[1] Fig. 5.3B displayed the unit cells at the *ab* herringbone plane viewed down the *c*-axis that is along the incident angle of the excitation light.

Table 5.1 Unit cell parameters of pentacene single crystal

Parameters	Value
a	7.71 Å
b	6.28 Å
c	14.4 Å
α	88.0°
β	76.8°
γ	84.5°

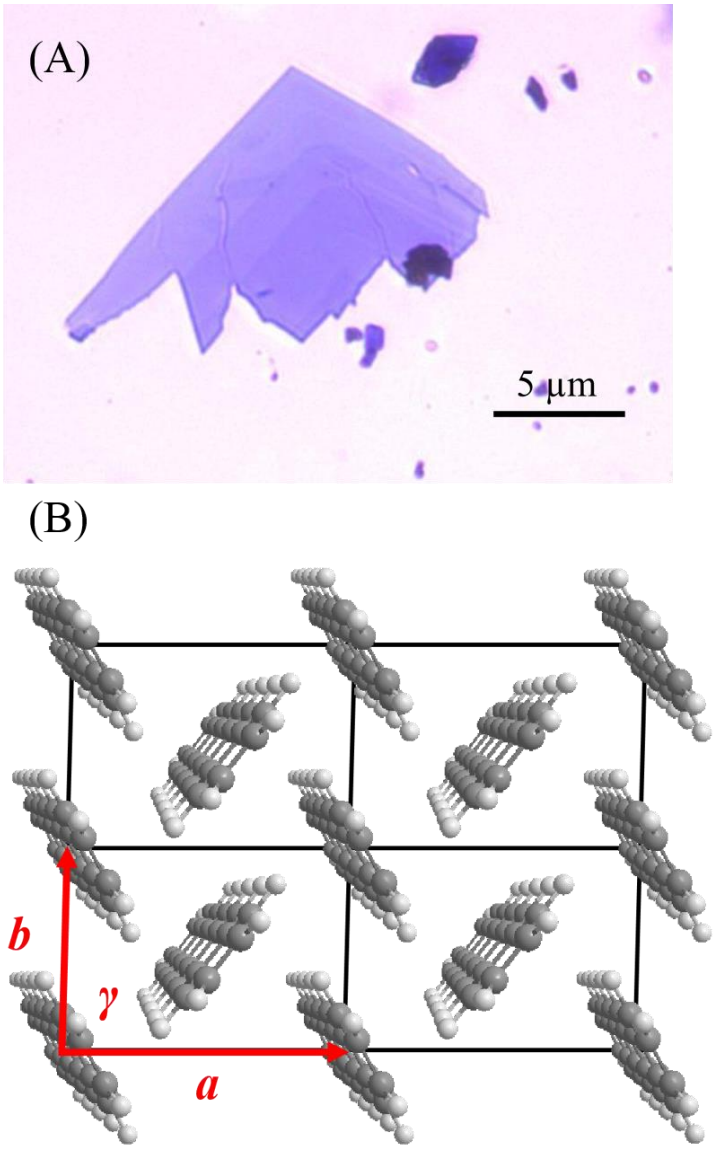

Figure 5.3 (A) Photographic image of a pentacene single crystal used for the polarized absorption experiment. (B) Structure of triclinic pentacene single crystal viewed down the *c*-axis.

The pentacene solution was prepared by dissolving pentacene powder in dichlorobenzene at a concentration of ca. 0.03 mM. The absorption spectrum of the isolated pentacene molecules in solution was obtained using a Shimadzu UV 1800 UV-Vis spectrophotometer.

5.3 Results and Discussion

Linear absorption measurements of the pentacene single crystals were conducted by irradiating the excitation light normal to the *ab* herringbone plane that contains the most strongly coupled molecules. The electric field interacting with the packed pentacene molecules at various polarization angles provides information that allows us to obtain knowledge on the anisotropic nature of the excitons. Fig. 5.4 shows the linear absorption spectra of crystalline pentacene as a function of the polarization angles. As the polarization rotates from 0° to 90° in an interval of 10°, a broad absorption peak centered at 672 nm starts to decrease till diminished at 90°, while a weaker but narrower peak at 627 nm follows the opposite tendency that increases gradually until maximum. A close look further reveals that the spectra polarized along 0° and 90° have fundamentally distinct spectral components, and the rest of the absorption spectra at polarization angles from 10° and 80° are the combinations of the two orthogonally polarized spectra. This is direct evidence of the anisotropic nature of the excitonic properties in crystalline pentacene. Based on the crystal structure, we assigned that the 0° polarization to coincide with the crystallographic short *b*-axis, in accord with the ellipsometry and reflectivity studies,[22-24, 26] and 90° polarization is in the direction perpendicular to the *b*-axis, that is mainly along the crystallographic long *a*-axis.

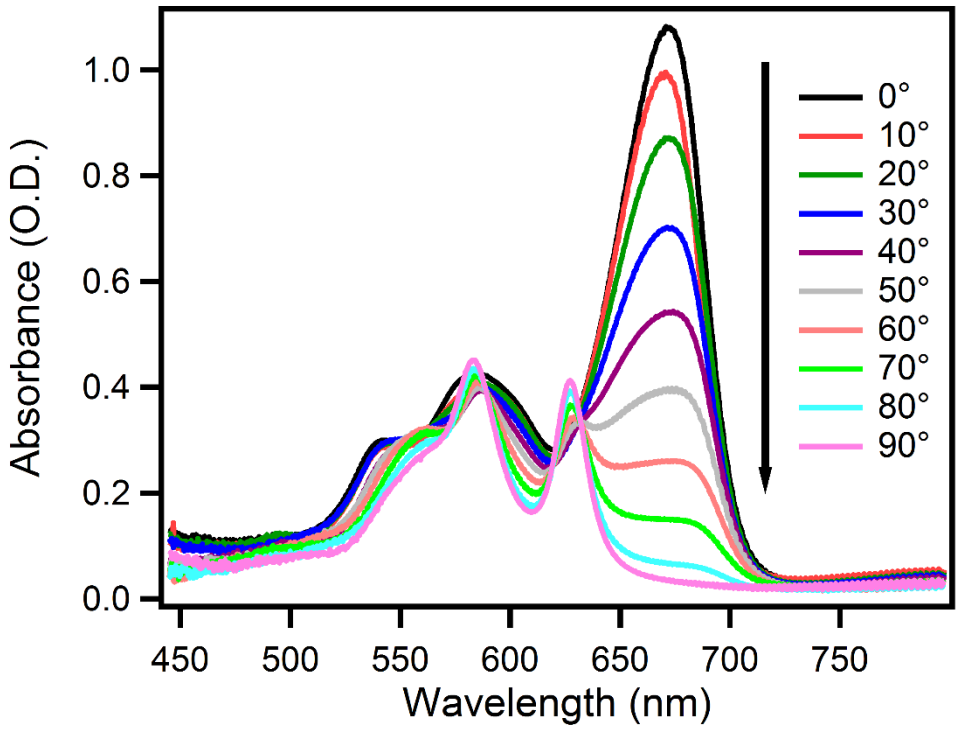

Figure 5.4 Linear absorption spectra of pentacene single crystal as a function of the polarization angles, from 0° to 90° in an interval of 10° .

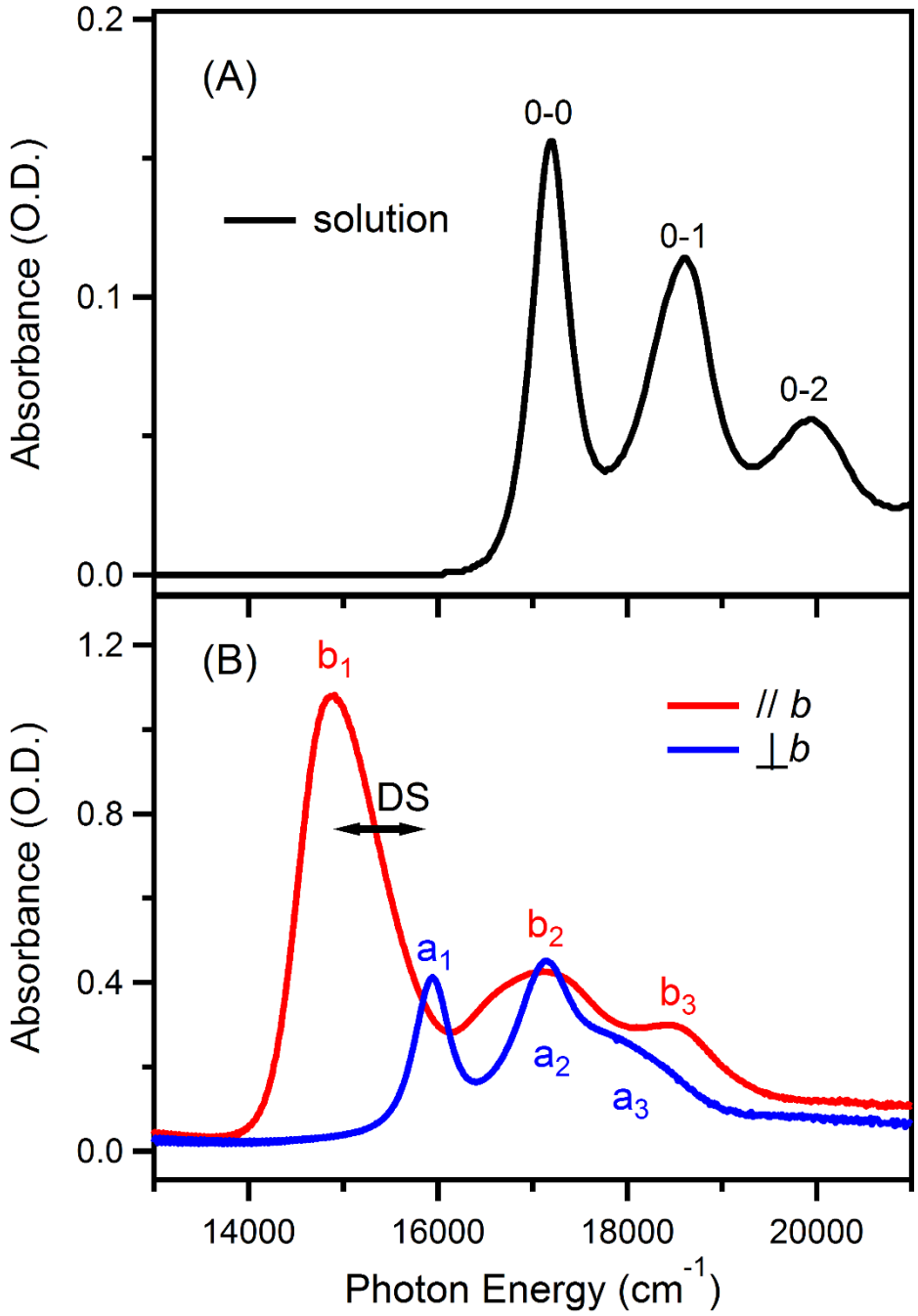

Figure 5.5 (A) Linear absorption spectrum of pentacene in dichlorobenzene solution. (B) Polarized absorption spectra of crystalline pentacene: red line is polarized parallel to the *b*-axis of the single crystal, while the blue line is polarized perpendicular to the *b*-axis. Davydov splitting (DS) is the energy gap between b_1 and a_1 transitions.

In contrast, shown in Fig. 5.5A is the absorption spectrum of the pentacene solution. The vibronic state information of the isolated pentacene molecule is clear: well-resolved vibronic progressions from lower to higher photon energy correspond to the excitations from the ground state to higher vibronic states, i.e. 0-0, 0-1, and 0-2, respectively. The associated vibrational energy, ω_{vib}, is 1380 cm^{-1} and results from a symmetric ring-stretching mode that is typical for many π-conjugated molecules. Fig. 5.6 illustrates the nuclear potential wells for the ground (S_0) and the first excited electronic state (S_1) of a pentacene molecule. The 0-1 vibronic transition possesses the highest Franck-Condon factor, as the 0-1 vibronic peak has the largest area.

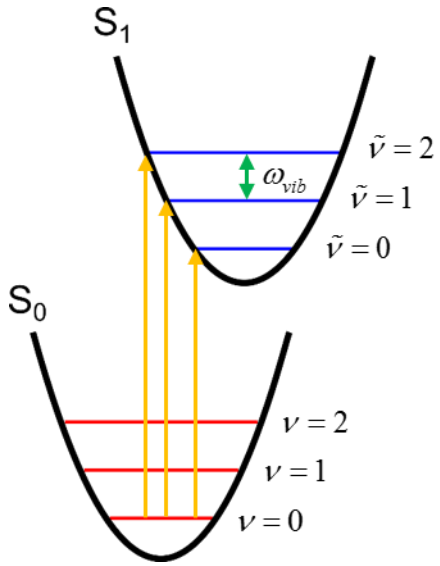

Figure 5.6 Nuclear potential wells corresponding to the ground (S_0) and excited (S_1) electronic states of a pentacene molecule.

For better comparison, in Fig. 5.5B, the absorption spectra polarized parallel and perpendicular to the *b*-axis are replotted as a function of photon energy (cm^{-1}). Peaks in //*b* spectrum are labeled as b_1, b_2, b_3, in order of increasing photon energy, while those in $\perp b$ spectrum, that is mainly in the direction along the crystallographic long *a*-axis, are labeled as a_1, a_2, a_3, Considerable spectra changes between Fig. 5.5 A and B, such as the discrepancy in the vibronic structure, are the results of pentacene crystallization. The compact packing of pentacene molecules in a well-defined crystal structure gives rise to strong excitonic coupling which is not present in pentacene solution. In detail, the *b*-polarized spectral component shows the greatest deviation from that of pentacene monomers in solution: the first vibronic peak b_1 carries a far more dominant ratio of the total transition strength than that in the monomer spectrum, 0-0; the linewidth for each peak is significantly broadened, and the peak separation is distorted. For example, the first two peaks b_1 and b_2 are separated by 2200 cm^{-1}, 59% larger than the vibrational energy for a monomer, i.e. 1380 cm^{-1}. In contrast, as for the $\perp b$ spectrum, the linewidth of the first peak a_1 essentially matches that of the monomer, and the spectral separation between a_1 and a_2 is close to the vibrational energy. The ratio of a_1/a_2, however, is attenuated relative to that of a monomer. In addition, compared to b_1, a_1 is shifted higher in energy by about 1000 cm^{-1}. The significant energy gap between b_1 and a_1 is called Davydov splitting (DS).

To explain the peculiar polarized absorption spectra of pentacene single crystals, especially the role of excitons coupling in the photophysical behavior, we have collaborated with Dr. Spano and his coworkers, whose calculations did an excellent job in reproducing most of the spectral features. Details of the theoretical model and the calculation can be found in the literature.[28] Basically, under the pentacene dimer model,

both Frenkel-type exciton in which the electron and hole are confined to a given pentacene molecule, and charge-transfer (CT) exciton, in which the electron and hole spread on different molecules are considered. There are three basic types of basis states,[29-33] shown in Fig. 5.7: 1) Frenkel one-particle is the case in which one molecule is electronically excited to S_1 state with $\tilde{\nu}$ vibrational quanta, while the neighboring molecule stays both electronically and vibrationally unexcited; 2) Frenkel two-particle, on the other hand, have both molecules excited, but one is in the vibronic excited state, while the other is only vibrationally excited. 3) CT exciton has both molecules electronically excited, but it is the state that one hole resides in one cationic molecule with $\tilde{\nu}_+$ vibrational quanta while the electron resides at the adjacent anionic molecule with $\tilde{\nu}_-$ vibrational quanta. The spectral features of the polarized absorption spectra are calculated by solving the Hamiltonian that can be divided into a Frenkel-Holstein Hamiltonian and a CT-Holstein Hamiltonian. The former Hamiltonian accounts for mainly the Frenkel excitons and the Coulombic coupling between chromophores, while the latter Hamiltonian represents the CT excitation as well as the charge interaction responsible for the electron and hole movements.[34]

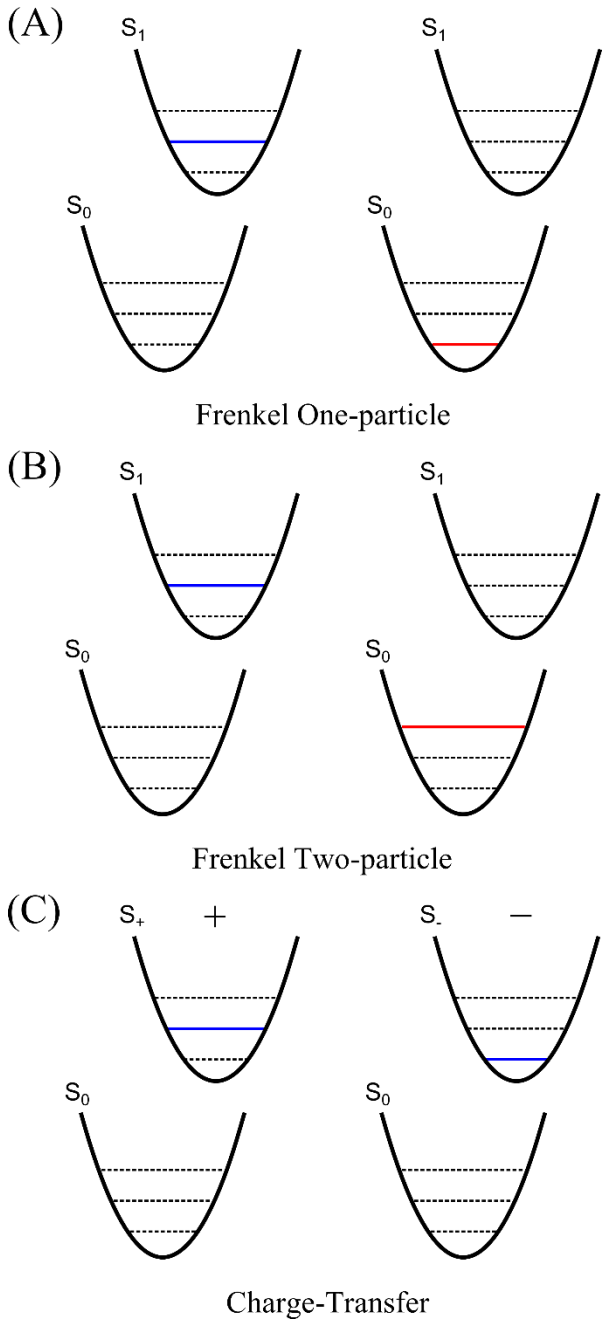

Figure 5.7 Schematic illustrations of basis states for a pentacene dimer: (A) Frenkel one-particle exciton, (B) Frenkel two-particle exciton, (C) Charge-transfer exciton. Dashed lines correspond to vibrational states, and solid lines account for the occupied states. The excited vibronic state is in blue color and the excited vibrational state is in red.

Based on the theoretical calculation, the various transitions observed in the polarized absorption spectra (a_1, a_2, a_3 and b_1, b_2, b_3) carry essentially different compositions of the three basis exciton states. The dominant components, b_1 in //*b* spectrum as well as a_1 and a_2 in $\perp b$ spectrum contain mainly the mixtures of the CT excitons and Frenkel one-particle excitons. In particular, b_1 transition, the lower Davydov component, has a large CT admixture, approximately 45%. As comparison, the first transition a_1 in $\perp b$ spectrum, the upper Davydov component, is from the excited state which is dominated by Frenkel one-particle exciton, involving a much smaller amount of CT admixture for less than 15%. As for the higher energy transitions, such as b_2, b_3, and a_3, the compositions become more complex, in which contributions from Frenckel two-particle excitons are not negligible.

The agreement between the polarized absorption spectra and the theoretical model indicates that CT excitons play an important role in the anisotropic nature of the low-energy excitons of pentacene single crystals, in accord with previous estimates.[35-36] The mechanism is shown schematically in Fig. 5.8. If the contribution of the CT excitons is removed from the total Hamiltonian and only the Frenkel excitons are retained, although the crystal structure still gives rise to the symmetric and antisymmetric Frenkel excitons that are along the //*b* and $\perp b$ directions, the weak splitting between the two Frenkel-alone exciton states, resulting from the Coulombic coupling, is less than 100 cm^{-1}. Furthermore, the ordering of the lowest excited states in the absence of the CT excitons are to be reversed, that is, a_1 has lower energy than b_1, opposite to our experimental observation. Activating Frenkel/CT mixing, on the other hand, reverses the energy levels of the lowest energy excitons. This mechanism can be understood as follows. Similar to the Frenkel-alone case,

the CT excitons also split into symmetric and antisymmetric CT states due to the crystal structure. Despite the fact that the two CT states have negligible energy difference, they only couple to the Frenkel states that have the same symmetry. The coupling strengths between symmetric and antisymmetric CT/Frenkel mixing states are based on D_e+D_h, and D_e-D_h, respectively, where D_e and D_h are the exciton dissociation integrals responsible for electron and hole hopping. When D_e and D_h have the same sign such as in tetracene and pentacene,[37] the coupling between the symmetric states (D_e+D_h) is much stronger than that between the antisymmetric states (D_e-D_h). Therefore, as shown in Fig. 5.8, the symmetric states have much larger splitting than the antisymmetric states do, and hence the lower energy state of the symmetric Frenkel/CT mixing appears to be below that of the antisymmetric Frenkel/CT mixing, essentially matching the observed DS. This model agrees with the calculated compositions that the excited state accounting for the b_1 transition has higher CT exciton ratio than the a_1 transition does. In addition, as the analysis shows that the superexchange coupling leads to J-aggregate-like vibronic signature along the symmetric //*b* direction and H-aggregate-like vibronic signature along the $\perp b$ antisymmetric direction, the Frenkel/CT mixing also explains the enhancement of the ratio b_1/b_2 and the slight attenuation of the ratio a_1/a_2, compared to the pentacene monomer spectrum.[31]

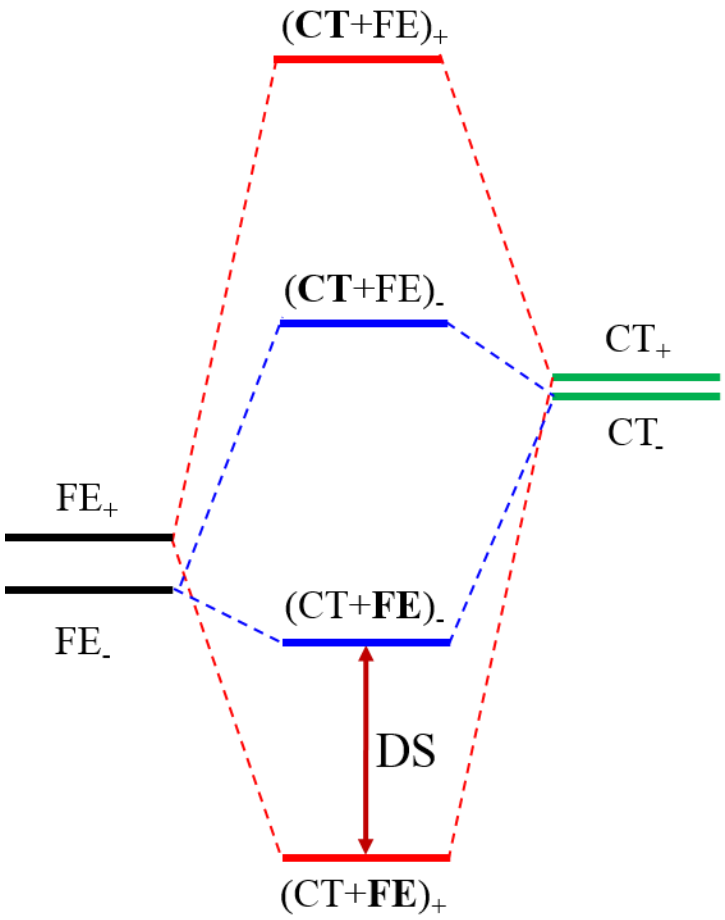

Figure 5.8 Schematic of the coupling between Frenkel exciton (left) and CT excitons (right). Davydov splitting (DS) is between the two lowest states corresponding to the couplings between symmetric (lower) and antisymmetric (higher) states.

5.4 Summary

In this chapter, we present polarized linear absorption spectra of ultrathin crystalline pentacene utilizing direct transmission measurements. Due to the small sizes of our crystals, we developed the experimental setup that combined an optical microscope and a UV-Vis spectrometer for positioning and irradiating pentacene single crystals normal to the *ab* herringbone plane that contains the most strongly coupled molecules. Compared to the unpolarized absorption spectrum of monomer pentacene in solution, the polarized spectra of crystalline pentacene illustrates dramatic spectral changes because of the intermolecular packing upon crystallization. In addition, significant deviations also exist between the spectral lineshapes for excitation polarized parallel and perpendicular to the crystallographic short *b*-axis. The two polarization-dependent components allows us to obtain detailed information on the anisotropic nature of the excitons responsible for the pronounced Davydov splitting (≈1000 cm^{-1}) as well as higher vibronically excited states.

The theoretical analysis was conducted using a Holstein-like Hamiltonian based on both Frenkel and charge transfer excitons. Agreement has been achieved between the theoretical calculation and the experimental results.[28] The model establishes the Frenkel/CT mixing nature of low-lying excitations: strong CT contribution (45%) is responsible for the *b*-polarized lower Davydov component, while far less CT content (15%) is found in the *a*-polarized upper Davydov component. Generally, the strong coupling between the Frenkel excitons and CT excitons accounts for the J-aggregate-like vibronic signatures in the *b*-polarized spectrum and H-aggregate-like vibronic signatures in the *a*-polarized spectrum.

5.5 Bibliography

1. Coropceanu, V.; Cornil, J.; da Silva, D. A.; Olivier, Y.; Silbey, R.; Bredas, J. L., Charge Transport in Organic Semiconductors. *Chem. Rev.* **2007,** *107* (4), 926-952.
2. Hains, A. W.; Liang, Z. Q.; Woodhouse, M. A.; Gregg, B. A., Molecular Semiconductors in Organic Photovoltaic Cells. *Chem. Rev.* **2010,** *110* (11), 6689-6735.
3. Murphy, A. R.; Frechet, J. M. J., Organic Semiconducting Oligomers for Use in Thin Film Transistors. *Chem. Rev.* **2007,** *107* (4), 1066-1096.
4. Samuel, I. D. W.; Turnbull, G. A., Organic Semiconductor Lasers. *Chem. Rev.* **2007,** *107* (4), 1272-1295.
5. Shirota, Y.; Kageyama, H., Charge Carrier Transporting Molecular Materials and Their Applications in Devices. *Chem. Rev.* **2007,** *107* (4), 953-1010.
6. Zahn, D. R. T.; Gavrila, G. N.; Salvan, G., Electronic and Vibrational Spectroscopies Applied to Organic/Inorganic Interfaces. *Chem. Rev.* **2007,** *107* (4), 1161-1232.
7. Kohler, A., Electronic Processes in Organic Semiconductors : An Introduction. Bässler, H., Ed.
8. Chernikov, A.; Yaffe, O.; Kumar, B.; Zhong, Y.; Nuckolls, C.; Heinz, T. F., Spectroscopic Study of Anisotropic Excitons in Single Crystal Hexacene. *J. Phys. Chem. Lett.* **2014,** *5* (21), 3632-3635.
9. Dimitrakopoulos, C. D.; Malenfant, P. R. L., Organic Thin Film Transistors for Large Area Electronics. *Adv. Mater.* **2002,** *14* (2), 99-+.

10. Jurchescu, O. D.; Baas, J.; Palstra, T. T. M., Effect of Impurities on the Mobility of Single Crystal Pentacene. *Appl. Phys. Lett.* **2004,** *84* (16), 3061-3063.

11. Smith, M. B.; Michl, J., Singlet Fission. *Chem. Rev.* **2010,** *110* (11), 6891-6936.

12. Burdett, J. J.; Bardeen, C. J., The Dynamics of Singlet Fission in Crystalline Tetracene and Covalent Analogs. *Acc. Chem. Res.* **2013,** *46* (6), 1312-1320.

13. Congreve, D. N.; Lee, J. Y.; Thompson, N. J.; Hontz, E.; Yost, S. R.; Reusswig, P. D.; Bahlke, M. E.; Reineke, S.; Van Voorhis, T.; Baldo, M. A., External Quantum Efficiency above 100% in a Singlet-Exciton-Fission-Based Organic Photovoltaic Cell. *Science* **2013,** *340* (6130), 334-337.

14. Smith, M. B.; Michl, J., Recent Advances in Singlet Fission. *Annu. Rev. Phys. Chem.* **2013,** *64*, 361-386.

15. Singh, S.; Jones, W. J.; Siebrand, W.; Stoichef.Bp; Schneide.Wg, Laser Generation of Excitons and Fluorescence in Anthracene Crystals. *J. Chem. Phys.* **1965,** *42* (1), 330.

16. Shockley, W.; Queisser, H. J., Detailed Balance Limit of Efficiency of P-N Junction Solar Cells. *J. Appl. Phys.* **1961,** *32* (3), 510.

17. Beljonne, D.; Yamagata, H.; Bredas, J. L.; Spano, F. C.; Olivier, Y., Charge-Transfer Excitations Steer the Davydov Splitting and Mediate Singlet Exciton Fission in Pentacene. *Phys. Rev. Lett.* **2013,** *110* (22), 5.

18. Thorsmolle, V. K.; Averitt, R. D.; Demsar, J.; Smith, D. L.; Tretiak, S.; Martin, R. L.; Chi, X.; Crone, B. K.; Ramirez, A. P.; Taylor, A. J., Morphology Effectively Controls Singlet-Triplet Exciton Relaxation and Charge Transport in Organic Semiconductors. *Phys. Rev. Lett.* **2009,** *102* (1).

19. Reese, C.; Bao, Z., Organic Single-Crystal Field-Effect Transistors. *Mater. Today* **2007,** *10* (3), 20-27.

20. Aoki-Matsumoto, T.; Furuta, K.; Yamada, T.; Moriya, H.; Mizuno, K.; Matsui, A. H., Excitonic Photoluminescence in Pentacene Single Crystal. *Int. J. Mod. Phys. B* **2001,** *15* (28-30), 3753-3756.

21. Prikhotk.Af; Tsikora, L. I., Spectral Investigations of Pentacene. *Opt. Spectrosc.* **1968,** *25* (3), 242.

22. Zanker, V.; Preuss, J., Microspectrometrical Measurements on Single Crystals of Tetracene and Pentacene in Depedence of Thickness and Temperature. *Z. Angew. Physik* **1969,** *27* (6), 363.

23. Dressel, M.; Gompf, B.; Faltermeier, D.; Tripathi, A. K.; Pflaum, J.; Schubert, M., Kramers-Kronig-Consistent Optical Functions of Anisotropic Crystals: Generalized Spectroscopic Ellipsometry on Pentacene. *Opt. Express* **2008,** *16* (24), 19770-19778.

24. Faltermeier, D.; Gompf, B.; Dressel, M.; Tripathi, A. K.; Pflaum, J., Optical Properties of Pentacene Thin Films and Single Crystals. *Phys. Rev. B* **2006,** *74* (12).

25. Grobosch, M.; Schuster, R.; Pichler, T.; Knupfer, M.; Berger, H., Analysis of the Anisotropy of Excitons in Pentacene Single Crystals Using Reflectivity Measurements and Electron Energy-Loss Spectroscopy. *Phys. Rev. B* **2006,** *74* (15).

26. Hinderhofer, A.; Heinemeyer, U.; Gerlach, A.; Kowarik, S.; Jacobs, R. M. J.; Sakamoto, Y.; Suzuki, T.; Schreiber, F., Optical Properties of Pentacene and Perfluoropentacene Thin Films. *J. Chem. Phys.* **2007,** *127* (19).

27. Laudise, R. A.; Kloc, C.; Simpkins, P. G.; Siegrist, T., Physical Vapor Growth of Organic Semiconductors. *J. Cryst. Growth* **1998,** *187* (3-4), 449-454.

28. Hestand, N. J.; Yamagata, H.; Xu, B. L.; Sun, D. Z.; Zhong, Y.; Harutyunyan, A. R.; Chen, G. G.; Dai, H. L.; Rao, Y.; Spano, F. C., Polarized Absorption in Crystalline Pentacene: Theory Vs Experiment. *J. Phys. Chem. C* **2015,** *119* (38), 22137-22147.

29. Spano, F. C., Absorption and Emission in Oligo-Phenylene Vinylene Nanoaggregates: The Role of Disorder and Structural Defects. *J. Chem. Phys.* **2002,** *116* (13), 5877-5891.

30. Spano, F. C., Excitons in Conjugated Oligomer Aggregates, Films, and Crystals. *Annu. Rev. Phys. Chem.* **2006,** *57*, 217-243.

31. Spano, F. C., The Spectral Signatures of Frenkel Polarons in H- and J-Aggregates. *Acc. Chem. Res.* **2010,** *43* (3), 429-439.

32. Philpott, M. R., Theory of Coupling of Electronic and Vibrational Excitations in Molecular Crystals and Helical Polymers. *J. Chem. Phys.* **1971,** *55* (5), 2039.

33. Stradomska, A.; Petelenz, P., Intermediate Vibronic Coupling in Sexithiophene Single Crystals. Ii. Three-Particle Contributions. *J. Chem. Phys.* **2009,** *131* (4).

34. Cudazzo, P.; Gatti, M.; Rubio, A.; Sottile, F., Frenkel Versus Charge-Transfer Exciton Dispersion in Molecular Crystals. *Phys. Rev. B* **2013,** *88* (19).

35. Beljonne, D.; Yamagata, H.; Bredas, J. L.; Spano, F. C.; Olivier, Y., Charge-Transfer Excitations Steer the Davydov Splitting and Mediate Singlet Exciton Fission in Pentacene. *Phys. Rev. Lett.* **2013,** *110* (22).

36. Yamagata, H.; Norton, J.; Hontz, E.; Olivier, Y.; Beljonne, D.; Bredas, J. L.; Silbey, R. J.; Spano, F. C., The Nature of Singlet Excitons in Oligoacene Molecular Crystals. *J. Chem. Phys.* **2011,** *134* (20).

37. Coropceanu, V.; Li, H.; Winget, P.; Zhu, L. Y.; Bredas, J. L., Electronic-Structure Theory of Organic Semiconductors: Charge-Transport Parameters and Metal/Organic Interfaces. *Annu. Rev. Mater. Res.* **2013,** *43*, 63-87.

CHAPTER 6

SINGLET FISSION IN MICRO-SIZED ULTRATHIN CRYSTALLINE HEXACENE

6.1 Introduction

Singlet fission (SF) is a spin-allowed process in which one singlet exciton generated by photoabsorption evolves into two triplet excitons as shown in Fig. 6.1B.[1] The fundamental differences between SF and the intersystem crossing (ISC) result from the fact that SF involves four electrons within two neighboring chromophores, while ISC in a classic Jablonski diagram takes place in an isolated molecule with two electrons.[2-3] Shown in Fig. 6.1A is a simplified diagram for the ISC between the singlet and triplet states. ISC is spin-forbidden as the spin of one electron flips through spin-orbit coupling, and consequently ISC often has a long lifetime (>10ns).[1-2] In contrast, as the system grows larger, the quantum states become complex. There would be 16 possible spin states that exist in a 4-electron 2-molecule system.[1, 3] SF is able to occur in a ultrafast time scale of sub-ps to ps, through a spin-allowed mechanism between two mixed states.

Since 2000, SF has been a subject of considerable research for both experimentalists[4-9] and theorists[10-13] as it has great potential for breaking the Shockley-Queisser limit, thereby leading to higher solar energy utilization. Recent studies have showed that SF occurs on a variety of materials, ranging from small molecules[14], thin films[15-18], solution[7], to polymers[4]. Despite those recent efforts, the SF mechanism still remains unclear. For example, does a multiexciton state exist? If so, what role does the multiexciton state play in SF? Is SF a one-dominant-step or two-step process? What is the

driving force for the SF process and what determines the reaction rate? A lack of knowledge for the SF mechanism is hindering a rationale design of new materials with more efficient solar energy conversion.

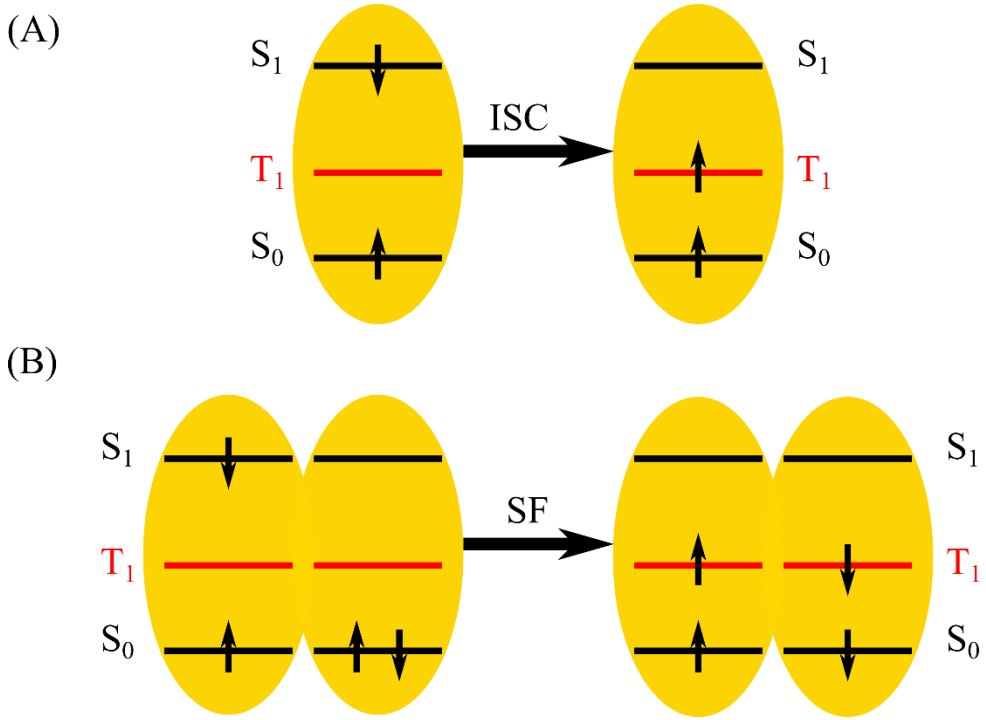

Figure 6.1 Energy diagrams of intersystem crossing ("ISC", A) and singlet fission ("SF", B)

A modified Merrifield model is commonly used to describe SF, given by[19],

$$[S_0 + S_1] \xrightarrow{k_1} {}^1[TT] \xrightarrow{k_2} [T_1 + T_1] \quad (6.1)$$

where k_1 and k_2 are the rates of the two consecutive steps, and ^{1}[TT], the correlated triplet pair, is also called multiexciton state that is a coherent superposition of two triplet states. Both [S_0+S_1] and ^{1}[TT] are the eigenfunctions of the total spin angular momentum operator for a two-chromophore system, which sum up as singlet states.[3] Therefore, the conversion in the first step is spin-allowed. Subsequently, the second step corresponds to the dissociation of the correlated triplet pair, forming two isolated triplet excitons. Two mechanisms have been invoked to rationalize the first step of the SF process: direct and charge-transfer (CT) mediated mechanisms[10]. In the direct SF mechanism, the excited singlet states convert directly to the ^{1}[TT] states in a scheme that can be seen as two electrons transfer simultaneously (Fig. 6.2A). The two-electron direct SF, however, was found to be too weak to explain the fast SF observed in the experiments.[20] On the other hand, in the CT mediated SF mechanism, the excited states relax through the CT states to ^{1}[TT] states, as displayed in Fig. 6.2B, where the CT states are transiently populated as virtual intermediate states (i.e. superexchange) [21]. All the models described above stress the importance of the first step in Eq. 6.1. In fact, it is often assumed that $k_1 << k_2$, and therefore, the first step is considered rate-determining.[19]

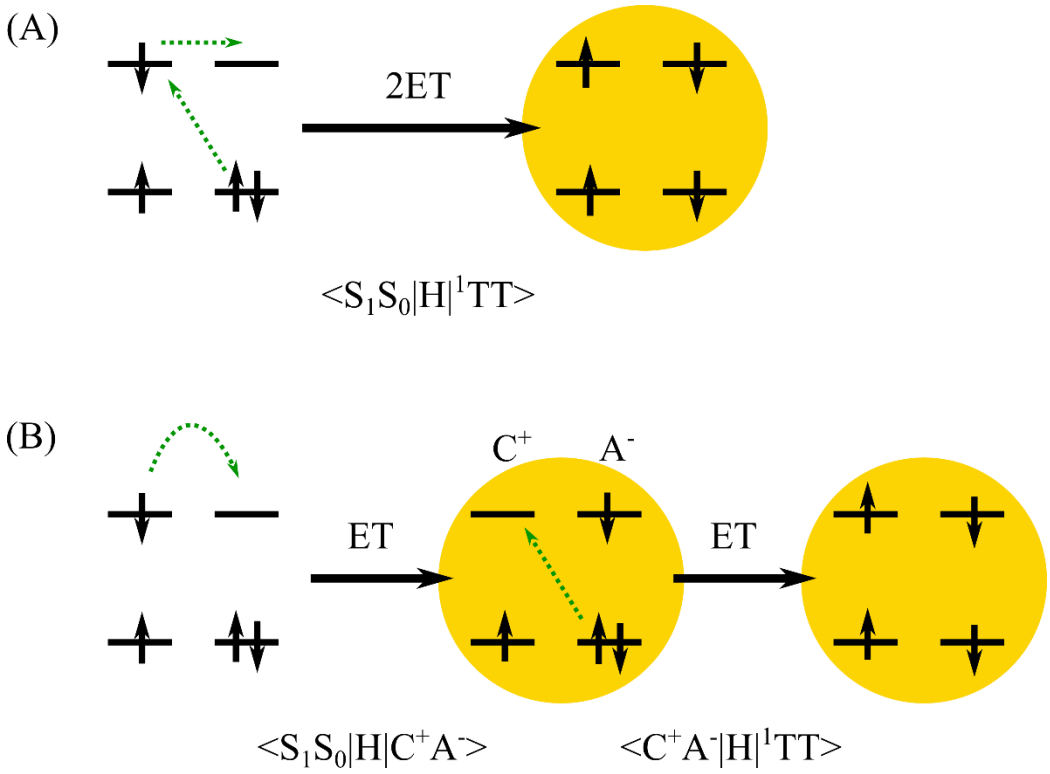

Figure 6.2 Schematic representations of the direct two-electron transfer (2ET) and the CT-mediated indirect mechanisms between the $[S_0+S_1]$ and $^1[TT]$ states.

Recent theoretical and experimental studies have showed that the intermolecular packing modulates the SF rate by electronic coupling, CT character as well as electron-vibration coupling[22-24]. In this chapter, we shall focus primarily on how the SF mechanism in hexacene single crystals is related to the CT character and the intermolecular packing. Crystalline hexacene is one of the model systems for studies of SF. Unlike amorphous or polycrystalline crystal, a single crystal has fewer defects and higher electron transport mobility.[25] Hexacene molecular crystals, like other organic molecular crystals, are made of weakly bound molecules. High quality hexacene single crystal can be grown with high charge carrier mobility,[26-27] enabling us to reveal the intrinsic mechanism of SF as well as its anisotropic properties resulted from the crystal structure. Polarized microscopic linear and transient absorption spectroscopies have been used to study anisotropic SF in hexacene single crystals. The one-step Merrifield model will be tested in this chapter.

6.2 Third-Order Nonlinear Spectroscopy: Transient Absorption

Ultrafast transient absorption (TA) spectroscopy has been proven to be a powerful tool to investigate ultrafast dynamics of SF in organic thin films.[28-30] Unlike the second-order nonlinear technology that was explained in Chapter 2, TA is a third-order nonlinear spectroscopy. Therefore, the majority of TA signal originates from the bulk, rather than the surface. In general, the third-order macroscopic polarization $\vec{P}^{(3)}$, follows[31],

$$\vec{P}^{(3)}(t_1,t_2,t_3) \propto \chi^{(3)}(t_1,t_2,t_3)\vec{E}_1(t)\vec{E}_2(t+t_1)\vec{E}_3(t+t_1+t_2) \tag{6.2}$$

where $\vec{E}_1, \vec{E}_2, \vec{E}_3$ are the three electric fields that interact with the system sequentially, t_1, t_2, t_3 are the temporal delay between the electric fields as well as the third-order signal, and $\chi^{(3)}$ is the third-order nonlinear susceptibility.

With respect to ultrafast TA experiment, a pump-probe configuration is often employed. Shown in Fig. 6.3A is the pump-probe pulse sequence, in which the first pulse, that excites the system of interest, serves as the pump pulse, and the second pulse, arriving in a temporal delay of t_2, is the probe pulse that is of coherent broadband. Compare to Eq. 6.2, the pump-probe configuration can be depicted as the case that $t_1 = 0$, in which the first pulse simultaneously interacts with the system twice. Subsequently, the third-order optical signal is generated after delay t_3, and the electric field strength is proportional to the third-order polarization, $\vec{P}^{(3)}$. The total signal measured in ultrafast TA experiment is a sum of the probe pulse and the third-order signal pulse. This can be realized by either optically filtering out the pump pulse in a collinear geometry, or physically blocking the pump pulse in a non-collinear geometry. The experimental observable is the ratio of the transmission variation, namely, $\frac{\Delta T}{T}$. The mathematical description, in the small signal approximation, can be expressed as,

$$\frac{\Delta T}{T} = \frac{|E_{pr} + E^{(3)}|^2 - |E_{pr}|^2}{|E_{pr}|^2} \approx \frac{2\,\mathrm{Re}(E_{pr} \cdot E^{(3)})}{|E_{pr}|^2} \propto 2\,\mathrm{Re}(\chi^{(3)} \cdot E_{pu}^2) \tag{6.3}$$

where *T* is the transmission light intensity, E_{pr}, E_{pu} are the electric field of the probe and pump pulses, respectively. As in TA spectroscopy, the generated third-order response is

heterodyned using the probe pulse as local oscillator. $\frac{\Delta T}{T}$ is proportional to the third-order susceptibility, $\chi^{(3)}$, as well as the intensity of the pump pulse.

In the case of SF, Fig. 6.3B illustrates a simplified model in which only the low energy excited states, such as S_1, S_2, T_1, and T_2, are considered. Because SF generally takes place on the time scale of ps, intersystem crossing and the non-radiative relaxation can be neglected as their temporal scales are on the order of ns. Three major contributions can be found in the TA spectra: 1) ground state bleaching (GSB) that accounts for the depletion of the ground states after photoexcitation of the pump pulse, 2) stimulated emission (SE) that occurs as the excited molecules emit the photons stimulated by the probe pulse, and can be Stokes shifted with respect to the pump pulse, 3) excited state absorption (ESA) which is responsible for the optical absorption of the photo-induced new species. The first two contributions result in more photons transmitted through the material, and therefore correspond to positive values of $\frac{\Delta T}{T}$. On the other hand, ESA is negative since an increased number of photons are absorbed by the newly-excited states. As for SF, the composition of ESA is complex. Aside from the singlet states generated by the pump pulse, the ultrafast SF conversion from singlet states to triplet states induces new ESA spectral features associated with the creation of triplet states, T_1. Hence, as shown in Fig. 6.3C, all possible Feynman diagrams can be categorized into at least four components, in which the SF process is represented by the dashed lines. As SF falls into the temporal regime of ps, ultrafast TA spectroscopy is capable of capturing the ultrafast temporal evolutions of all optical-transition-allowed species, and provides the information from which we can deduce the SF mechanism in organic materials.

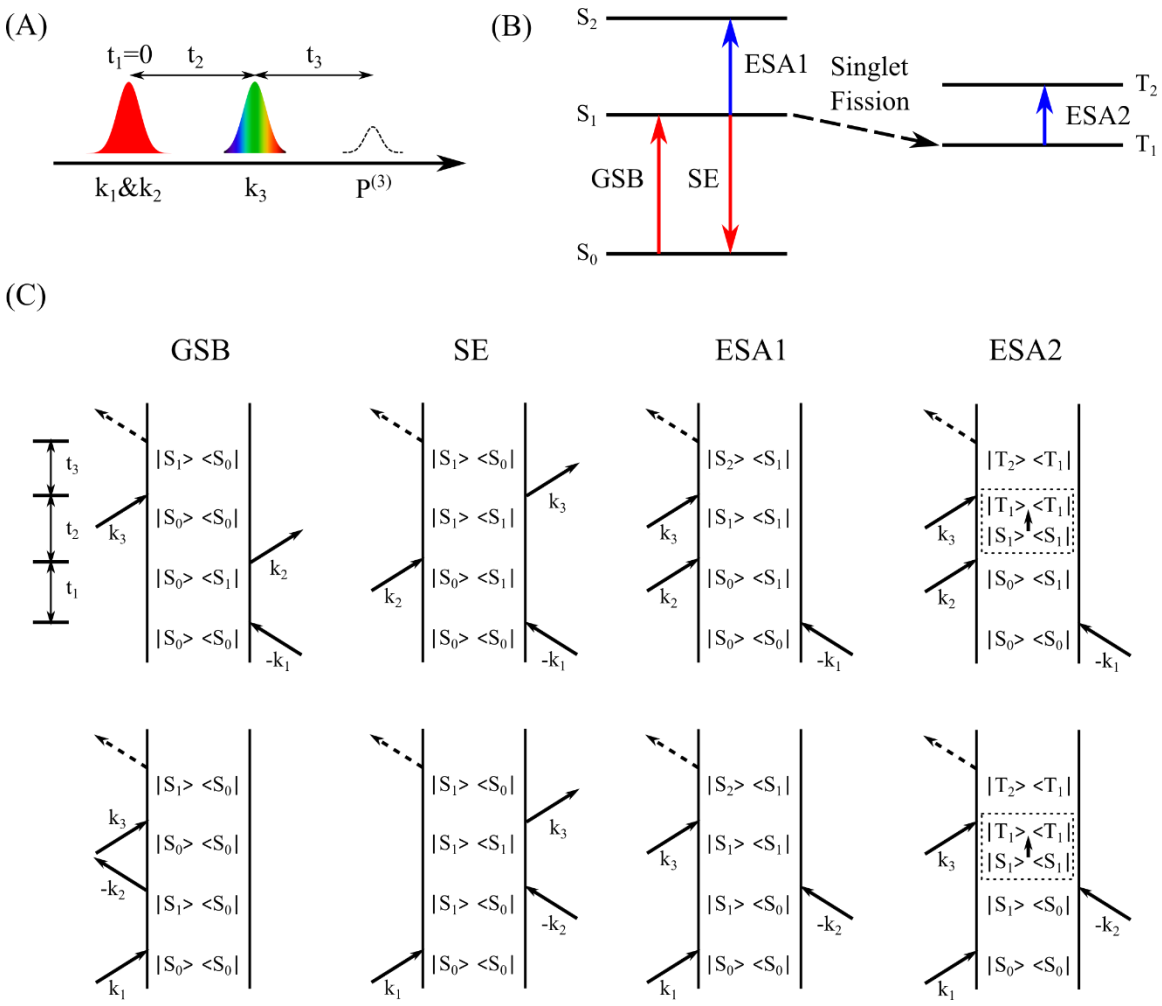

Figure 6.3 (A) Pulse sequence of TA spectroscopy in a pump-probe configuration. (B) Energy level diagram for SF. Four components are labelled associated with ground state bleaching (GSB), stimulated emission (SE), and excited state absorption (ESA). (C) Two-sided Feynman diagrams corresponding to GSB, SE, ESA1, and ESA2. The SF conversion is in the dotted region of ESA2.

6.3 Experiment

6.3.1 Sample Preparation

Hexacene single crystals for our experiments were grown in a physical vapor transport (PVT) furnace at atmospheric pressure. Hexacene precursor was synthesized according to a previously reported method[26-27]. ~1 mg hexacene powder was heated in a hot zone of the furnace (300 °C) for one week. 50 SCCM of ultrahigh purity argon gas (99.999%) served as purging gas as well as carrier gas. Hexacene single crystals were collected in the crystallization zone, in which their faces tend to grow parallel to the substrate, namely (001).[32] A typical size of a hexacene single crystal was on the order of ca. 20 μm × 40 μm × 0.5 μm.

Crystalline hexacene grown in this manner was first spread on a quartz substrate. Subsequently, the quartz substrate was sealed inside a gasket container assembled in a N_2 box to protect the single crystals from oxygen during optical experiments. All experiments were performed at room temperature.

Table 6.1 Unit cell parameters of hexacene single crystal[27]

Parameters	Value
a	7.673 Å
b	6.292 Å
c	16.424 Å
α	91.16°
β	98.66°
γ	95.71°

6.3.2 Microscopic Polarized Linear Absorption Experiment

The polarized linear absorption measurements of hexacene single crystals were conducted on a home-built microscope as discussed in Chapter 5. Briefly, an intensity-tunable halogen-lamp (Lumina-I) and a LED pen light were chosen as the unpolarized incoherent broadband light source for the UV-Vis transmission measurements as well as the illumination light for the microscope, respectively. A polarizer was placed between the lamp and the objective to select the polarization of the excitation light. The selected polarized light was focused onto a hexacene single crystal at normal incident angle by an objective with x10 magnification. The transmitted light was collected by a condenser and subsequently focused into a grating spectrometer (Andor Shamrock 500 with a grating blazed at 500nm, 150 groove/mm), that is equipped with a thermo-cooled CCD (Andor Newton). Only a few of crystallites met the requirements of the optical measurements on each substrate, even though small single crystals have been intentionally prepared. The thicknesses of the chosen hexacene samples were estimated to be ca. 520 nm according to the absorption coefficient of hexacene thin films reported in the literature.[33] All experiments were performed at room temperature.

6.3.3 Microscopic Polarized Transient Absorption Experiment

A regular transient absorption setup fails to work for small samples like hexancene single crystals in our experiments, because their size are about 100 μm^2. Thus we built a polarized transient absorption microscope to study the anisotropic SF in crystalline hexacene. The fundamental femtosecond light source was a 1 KHz regeneratively amplified Ti-Sapphire laser system seeded by a 78 MHz Ti-Sapphire oscillator. The output

laser with 800 nm center wavelength and 100 fs pulse duration was splited into two beams: one that remained at 800 nm center wavelength worked for pumping the sample, and the other that was converted to the supercontinuum (coherent white light) operated for probing the sample. In detail, the pump pulse went through an optical chopper and a motorized delay stage (Klinger) that controlled the optical length of the pump beam, namely, the delay between the pump and probe pulses. A selected neutral density filter (ND filter) was placed in the pump alignment to adjust the pump power, and a half-wave plate (HWP, Thorlabs) was used to tune the polarization of the pump pulse. As for the probe beam, a pair of HWP and polarizer (Thorlabs) was first employed to control both the power and the polarization of the fundamental light that was later focused in a sapphire crystal, where the supercontinuum light was generated. The pulse-by-pulse stability of the supercontinuum was optimized by the power of the incident fundamental light as well as the focus spot size. Subsequently, the supercontinuum probe pulse was collected by another 1-inch lens. Its polarization was adjusted by a broadband HWP (Thorlabs), and an 808nm notch filter (NF03-808E, Semrock) was used to remove the residual 800nm fundamental light. Before feeding into the microscope, the pump and probe pulses were recombined into a collinear alignment by a pellicle beam splitter. In the microscope setup, they were focused onto the sample perpendicularly in a way that the focus spot size of the pump light was about twice larger than that of the probe light. The transmitted light, both the pump and probe, were later filtered by a bandpass filter (Thorlabs) and only the probe light at wavelength between 400 nm and 800 nm was sent into the spectrometer. The acquisition of transient absorption spectra requires switching on/off of the pump pulses sequentially. This was achieved by setting the working frequency of the optical chopper and the sampling rate of the CCD at

100 Hz and 200 Hz, respectively. They were both synchronized to the 1 KHz laser system. The exposure time of the fast acquisition CCD was set at 1 ms, so that only one pulse was recorded each time. A labview program was written to control the translational stage that scanned the temporal delay between the pump and probe pulses and to record the transmission light as a function of wavelength (λ). The ratio of the transmission variation ($\frac{\Delta T}{T}(\lambda)$) was calculated simultaneously by the labview program following,

$$\frac{\Delta T}{T}(\lambda) = \frac{I_{on}(\lambda) - I_{off}(\lambda)}{I_{off}(\lambda) - I_{bg}(\lambda)} \tag{6.4}$$

where $I_{on}(\lambda)$ and $I_{off}(\lambda)$ are the transmitted probe light when the pump pulses are on and off, respectively, and $I_{bg}(\lambda)$ is the background signal that is mainly from the CCD detector itself. All data were collected using the labview program at the same settings. The polarized transient absorption measurements were performed by varying the polarization combinations of the pump and the probe lights. The detection sensitivity of about 5×10^{-4} was reached in our setup.

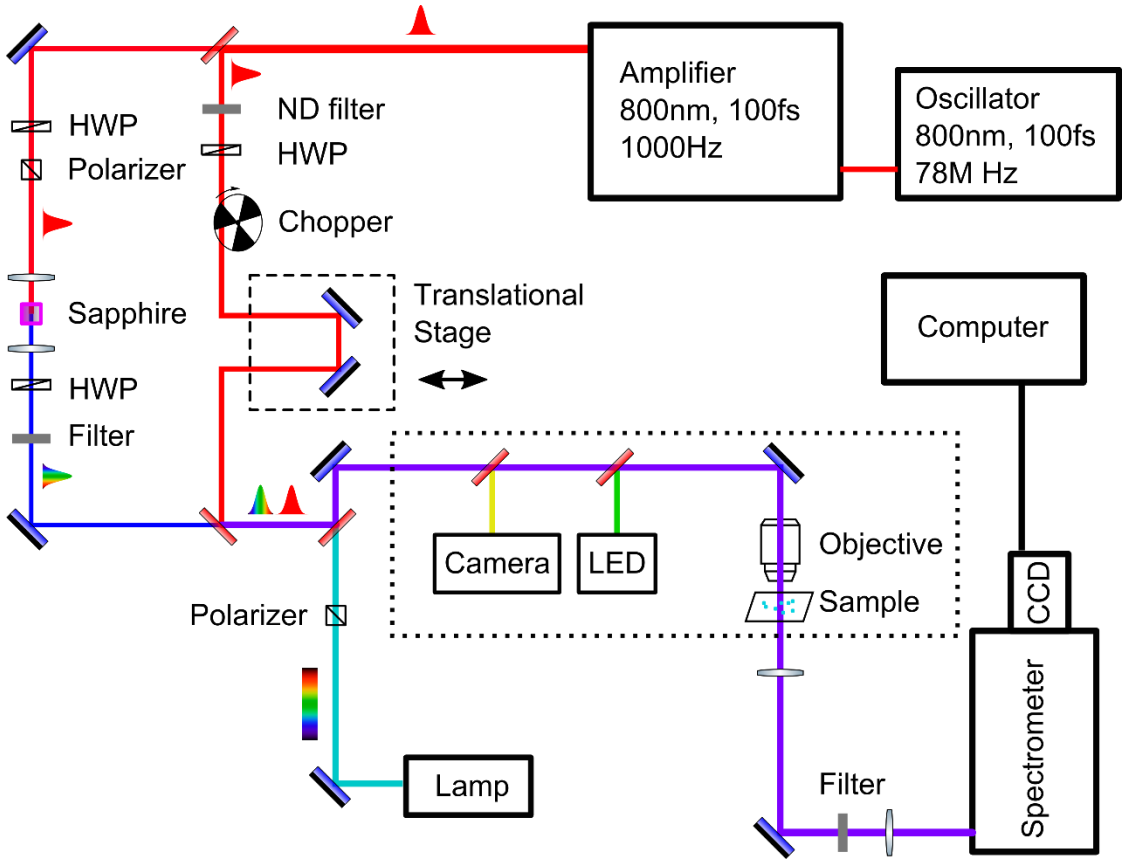

Figure 6.4 Schematic of the microscopic transient absorption setup

6.4 Results and Analysis

A photographic image of one of the hexcene single crystals used in the experiments is shown in Fig. 6.5B. The hexacene unit cell of triclinic crystal system is defined as in Fig. 6.5C with in-plane crystal lattice constants of a=7.673 Å and b=6.292 Å, respectively. The anisotropic properties in the *ab* plane are supported by the polarized linear absorption experiments. Fig. 6.5A displays polarization-resolved linear absorption spectra of the hexacene single crystal. The linear absorption measurements along the polarization of 0°

and 90° exhibit different spectral features. For the 90° polarization, the peak at 838 nm is assigned to the lowest transition along the short *b*-axis of the crystal, called b1. On the other hand, for the 0° polarization, the transition at 760 nm is assigned to the lowest transition along the long *a*-axis of the crystal, called a1. It is seen that the b1 transition is blue-shifted by an energy difference of 1250 cm^{-1} with respect to a1. The energy gap between the two lowest transitions is related to the splitting of the ground state excitations, so-called singlet Davydov splitting (DS). This large DS originates from two inequivalent molecular pairs in a unit cell. The broadening and redshift of b1 for the single crystal with respect to isolated molecules (such as hexcence dissolved in solution) are often considered as a signature of the CT mixing.[34]

To explore the anisotropic SF, polarized transient absorption measurements were performed by controlling the polarizations of the pump and the probe beams. Under the lowest photo-excitation of 800 nm, the single crystal sample was probed along the long *a*-axis and the short *b*-axis. Fig. 6.6 shows two-dimensional pseudo color plots of the transient absorption spectra ($\Delta T/T$) as functions of the probe wavelength (λ) and the pump-probe delay (t) that were pumped and probed along different axes. We chose two different scales to highlight the differences in evolutions of the perturbed ground state and newly populated excited states. The strong positive values in $\Delta T/T$ between 640 nm and 720 nm are mainly attributed to the GSB. As expected, these positive spectral responses in $\Delta T/T$ exhibit the same spectral response as the linear absorption spectra for the same polarizations. The negative changes in $\Delta T/T$ between 500 nm to 620 nm were attributed to be the photo-induced absorption (PIA) of the excited states. Both transient spectra have a broad featureless, short-lived peak in the range of 500 nm to 580 nm. The fast decay in the

spectral region was assigned to the excited state absorption from S_1 to a higher state S_n (S_1-S_n). On the other hand, the long-lived PIA peaks were assigned to the T_1-T_n transitions. In addition, the spectral features and dynamics of the *a*- and *b*- singlet excitons are independent of the polarization of the pump beam except for the magnitude in $\Delta T/T$ that results from the different cross sections along *a*- and *b*- axis. These results suggest that the excitation is delocalized over a few molecules in hexacene single crystals.

The most striking results in the ESA are that the long-lived PIAs along the *a*-axis and *b*-axis also exhibit distinct peak positions as the GSB does. The difference in the transitions along the *a*-axis and *b*-axis indicates that there exists triplet DS, which is on the order of 240 cm^{-1} in hexacene single crystals. This result indicates that there are two kinds of triplet states resulted from two axes of the intermolecular packing. We labeled the triplet states along the *a*-axis as T_1^a at 608 nm and that along the *b*-axis as T_1^b at 600 nm, respectively, leading to T_1^a - T_n and T_1^b - T_n transitions (we assume the triplet DS diminishes at higher level as it shows for the singlet DS in Fig. 6.5A). The energy level for T_1^b is closer to the ground state than that for T_1^a in hexacene. The order of energy levels for T_1^a and T_1^b is reversed in hexacene as compared with those for tetracene.[35] The large triplet DS and the reversal of T_1 suggest that the CT characters in hexacene are more prominent than those in other smaller oligoacene crystals.

As for the temporal evolution, Fig. 6.7 shows the kinetics traces of the three different transitions in $\Delta T/T$ by pumping along the *b*-axis: transition S_1-S_n at 525±5 nm (A, B), transition T_1^a - T_n at 608±5 nm (B) and transition T_1^b - T_n at 600±5 nm (A), respectively. It is important to note that the S_1-S_n and T_1-T_n transitions overlap with each

other spectrally. As such, we take the following into account our kinetic analyses: 1) transient behaviors at any wavelength are a sum of the S_1-S_n and T_1-T_n transitions; 2) SF is a two-step process rather than a one-step process since our data cannot be explained by the Merrifield model as the first step dominates. Specifically, we consider $\Delta T/T(\lambda, t)$ is a sum of the contributions from both the S_1-S_n and T_1-T_n transitions at a given wavelength:

$$\frac{\Delta T}{T}(\lambda,\ t) = c1 \cdot \sigma_{S_1-S_n}(\lambda) \cdot n_{S_1}(t)\ +\ c2 \cdot \sigma_{T_1-T_n}(\lambda) \cdot n_{T_1}(t) \tag{6.5}$$

where $n_{S_1}(t)$ and $n_{T_1}(t)$ are time-dependent populations of the singlet (S_1) and triplet (T_1) excitons, and $c1$ and $c2$ are negative weighted coefficients for the S_1-S_n and T_1-T_n transitions. A detailed fitting procedure can be found in Appendix B. Global fittings to the kinetic traces yield the generation and dissociation rate constants along the *a*-axis (k_1^a =5.0±0.2 ps^{-1}, k_2^a =3.3±0.2 ps^{-1}) and the *b*-axis (k_1^b =4.5±0.2 ps^{-1}, k_2^b =6.7±0.2 ps^{-1}), respectively. Our experimental results indicate that the SF in hexacene single crystals is a two-step and anisotropic process.

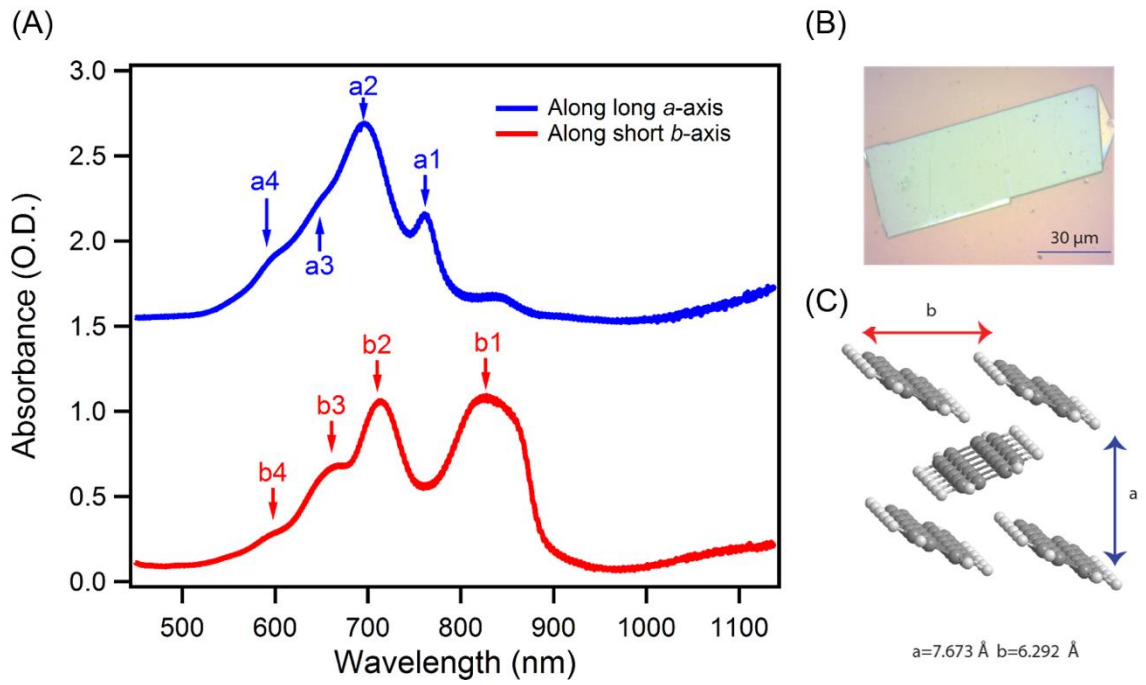

Figure 6.5 (A) Polarization-resolved linear absorption spectra of hexacene single crystal. Blue curve is the spectrum polarized along long *a*-axis (offset by 1.5 for better reading), and red curve is that polarized along short *b*-axis. Peaks are labelled from 1 to 4 as the transitions blue-shift. (B) Photographic image of one of the hexacene single crystals. C) Structure of triclinic hexcence single crystal viewed down the *c*-axis.

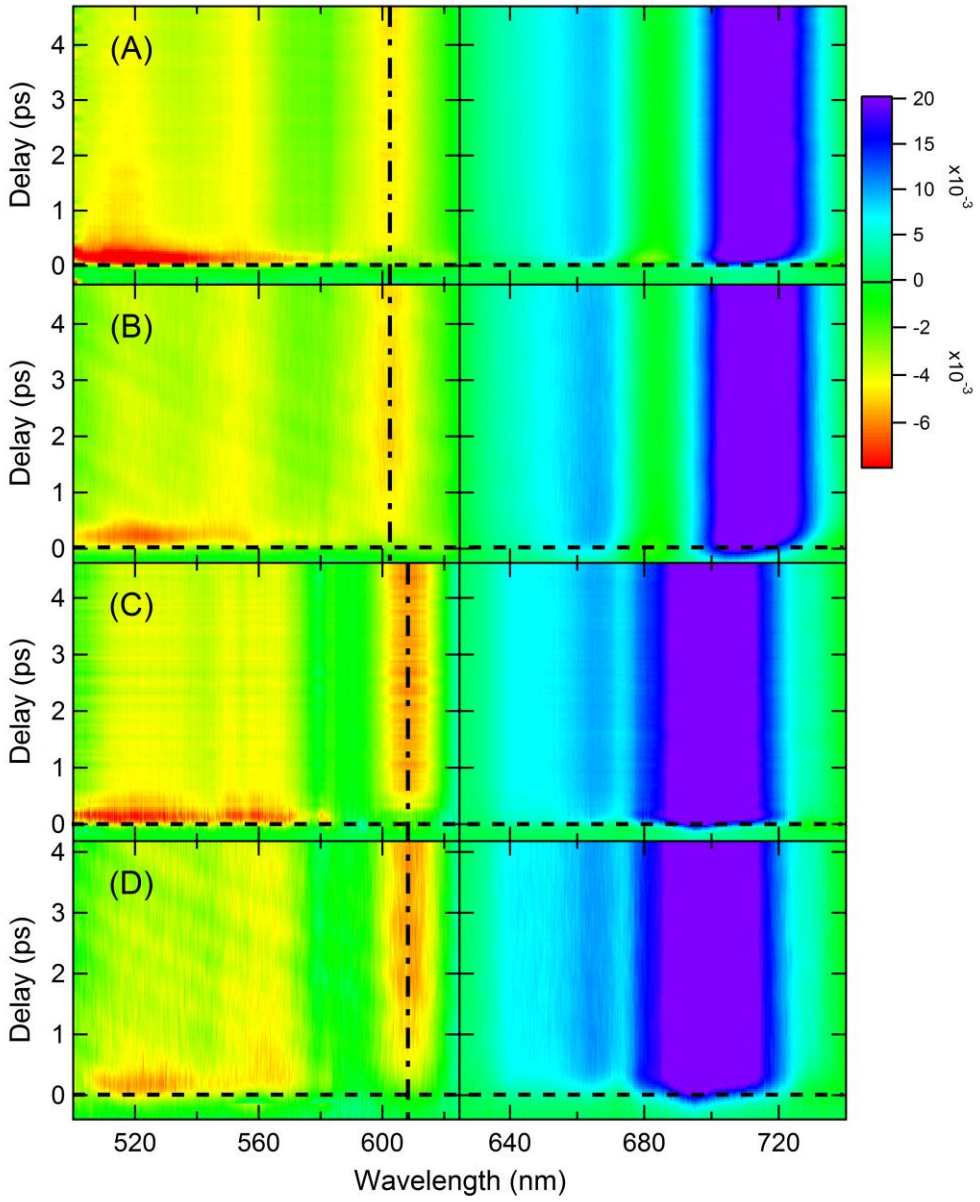

Figure 6.6 Pseudo-color plots of polarized transient absorption spectra from hexacence single crystal: (A) pumped along *b*-axis and probed along *b*-axis, (B) pumped along *a*-axis and probed along *b*-axis, (C) pumped along *b*-axis and probed along *a*-axis, (D) pumped along the *a*-axis and probed along the *a*-axis. For better contrast, the color scale for (A, D) is scaled up by a factor of 1.75. The horizontal dashed lines label t=0 between the pump and probe pulses, and the vertical dot dashed lines label the peaks of long-lived PIA.

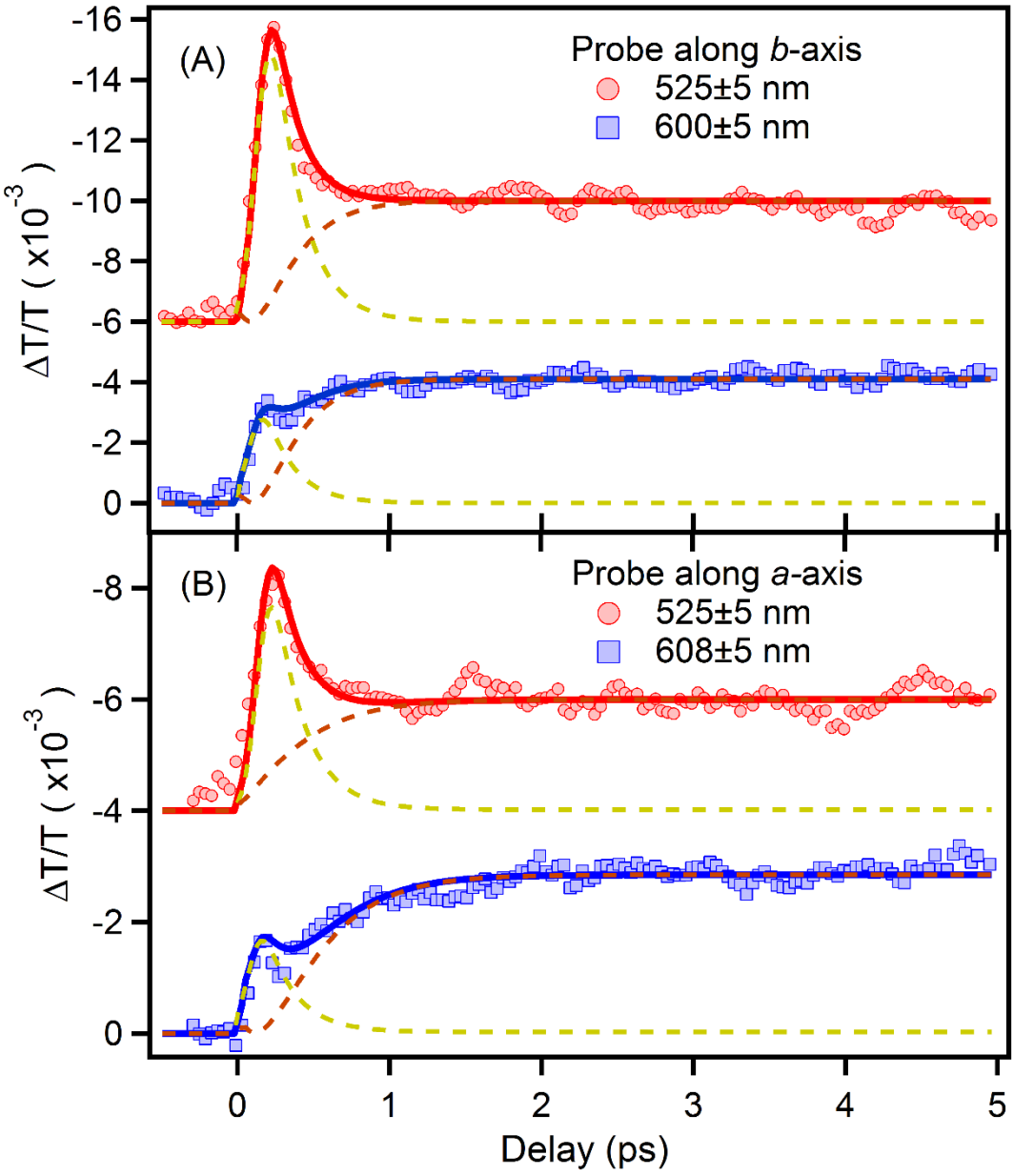

Figure 6.7 Kinetic traces at two different wavelengths under photoexcitation of 800 nm polarized along the *b*-axis.: (A) at 525±5 nm and 600±5 nm probing along the *b*-axis, and (B) 525±5 nm and 608±5 nm probing along the *a*-axis. The solid curves are the global fittings with the SF model described in the Appendix B. Yellow dashed lines are the components of singlet state, and the brown dashed lines are that of triplet state.

6.5 Discussion

The main findings in this chapter include the anisotropic SF rates and the triplet DS of hexacence single crystals. The anisotropic properties in SF are substantially mediated by the CT excitons that are close to the lowest excited state of hexacene. Both the singlet and triplet DSs in hexacene indicate that the CT excitons modulate the generation and dissociation of the ^{1}[TT] states through the entire SF process.

6.5.1 Anisotropic Multiexciton States in Hexacence Single Crystal

The anisotropic rates and triplet DS of hexacene single crystals strongly support our hypothesis that there exist two different ^{1}[TT] states along the *a*- and *b*- axes, namely, ^{1}[TT]^a and ^{1}[TT]^b. The energy level for the ^{1}[TT]^a state is 480 cm^{-1} higher than that of the ^{1}[TT]^b, corresponding to two triplet DS. Although the triplet DS is several times smaller than the singlet DS in hexacence single crystals, the anisotropic nature of the dissociated triplet states is still kept before diffusion. There is increasing evidence about the existence of the ^{1}[TT] state found in solution and solids.[8, 36] Recent studies based on the two-photon photoemission (TPPE) demonstrated the nature of the ^{1}[TT] state in pentacene, exhibiting the singlet and triplet characteristics.[21] Our anisotropic results not only demonstrate the existence of an intermediate ^{1}[TT] state in the SF process, but also provide strong evidence that the ^{1}[TT] states are anisotropic in hexacene as well.

6.5.2 Charge Transfer Excitons and Delocalized Excitation

The stacking and distance between molecules in a single crystal determine the ground state excitation as well as the SF rates. In other words, geometrical arrangements

of molecules in a unit cell determine if it is more favorable for the mixed CT and Frenkel excitons to decompose into their constituent triplet states or to remain in the correlated state. For the CT states close to the Frenkel S_1 states, efficient mixing of the Frenkel and CT excitons leads to a coupled wave function of the lowest adiabatic state. The coupling strength of the Frenkel and CT states arises as the ring number increases from anthracene to hexacene.[38-39] CT character, defined as the electron and hole residing on nearest-neighboring molecules, accounts for ca. 65% for the lowest lying exciton in hexacene based on the trend from anthracene, tetracene, to pentacene (See Appendix C). The energy difference between the CT state and the lowest Frenkel state in hexacene is much smaller compared to that in other shorter oligoacenes, which is approximately 1700 cm^{-1}.[40-41] Therefore, the Frenkel excitons along the *b*- and *a*- axes can be strongly coupled with the CT states. First-principles calculations of oligoacene crystals have shown that CT characters persist in the nearest neighbors up to four singlets.[21, 37] As a consequence, photo-generated carriers along the short *b*-axis can generate excitons along the long *a*-axis via CT excitons, or vice versa.

The contributions of the CT states to SF are more prominent in hexacene as compared to other oligoacenes. A strongly-coupled CT state in hexacene gives rise to the anisotropic property for both the multiexciton states and the dissociated triplet states. The participation of the CT states results in the reversal of the energy levels of the multiexciton states as well as the individual triplet states. Both the singlet and triplet excitons in hexacene are of CT character. As a result, the CT states in hexacene manipulate the delocalized excitations as well as the anisotropic generation and dissociation of the ^{1}[TT] states.

6.5.3 Anisotropic Singlet Fission Rates in Hexacence Single Crystals

Our polarization-dependent kinetic results reveal the anisotropic SF rates in hexacene single crystals. Along the short *b*-axis, the rate k_1^b (4.5±0.2 ps^{-1}) for the first step is slower than k_2^b (6.7±0.2 ps^{-1}) for the second step, while the rate k_1^a (5.0±0.2 ps^{-1}) is faster than the rate k_2^a (3.3±0.2 ps^{-1}) along the long *a*-axis. Different from the one-dominant-step model, our experimental results indicate that the two consecutive steps occur at comparable rates. As described in last section, it is the CT character in hexacene single crystal that highlights the anisotropic rates and the coupling in the process of SF. Generally, energy levels, electronic coupling, and electron-vibration couplings are considered as the main factors for the rates of SF in organic semiconductors.

In the first step, the driving force ΔG for the SF of hexacene is on the order of -4800 cm^{-1}. The electronic coupling strength V was calculated to be 320 cm^{-1} .[10] The strong electronic couplings of the Frenkel, CT, and multiexciton states drive electron transfer into the adiabatic regime on a classical Marcus model, accounting for the comparable rate constants in the first step along the *a*- and *b*-axes. On the other hand, ΔG in the second step appears to be zero from the ^{1}[TT] state to the two isolated T_1 states along the same crystallographic axis. The electronic coupling for the second step is much weaker than that for the first step. Nevertheless, the driving force ΔG from $^1[TT]^a$ to $^1[TT]^b$ can be as large as 480 cm^{-1}. Electron-vibration coupling is likely to be responsible for the anisotropic rates in the second step of SF in hexacene single crystals. Due to the intrinsic properties of intermolecular interactions, we exclude the possibility of the Holstein local electron-vibration coupling in the second step of SF.[10] Hence we invoke the nonlocal electron-

vibration coupling, namely, Peierls interaction, to explain the dissociation mechanism from a coherent ^{1}[TT] state to two adiabatic T_1 states. To decouple the electronic correlations of the multiexction state, different reorganization energies from ^{1}[TT] entities to isolated triplets are lost to Peierls interactions between the exciton and the intermolecular vibrational modes.[42] The dissociation of ^{1}[TT] in hexacene are likely to fall in the Marcus non-adiabatic limit, in which the electronic coupling strength determines the dissociation rate of the dissociation. The Peierls interactions induce fluctuations of the intermolecular couplings between the neighboring molecules in hexacene single crystals. Thus, the disentangled T_1 states are not purely localized. Instead, they are delocalized over more than one molecule due to the intermolecular interactions. The anisotropic dissociation rates of the multiexciton states originate from the anisotropic environment in the hexacene single crystals.

Early transient absorption studies of hexacene thin films attributed a slower SF to multi-phonon relaxations, as compared to pentacene and tetracene.[16] Ultrafast vibronic spectroscopies of pentacene and its derivatives showed that the SF process is similar to single-molecular internal conversion via a conical intersection due to the strong coupling between the nuclear and electronic motions.[5] On the theoretical side, the calculations in a crystalline environment face technical challenges. A dimer or trimer model cannot accurately describe the anisotropic rate and triplet DS in the hexacence single crystals. Previous theoretical calculations of hexacene derivatives concluded that the SF of hexacene is in the Marcus inverted region and is slower than that of pentacene, which is in qualitative agreement with our experimental results for the first step of SF. Although these

experimental results need more sophisticated theoretical support, they initiate a need to re-check the explanations for the SF mechanisms on tetracene and pentacene.

Taken together, we propose a unified model for the anisotropic SF in hexacene as depicted in Fig. 6.8. The energy level for the CT state is close to those of the Frenkel states in hexacene. As such, the CT state mediates both the singlet photoexcitation and the generation of the multiexciton states and triplet states. Photoexcitation close to the lowest transition populates molecules in hexacene single crystal, leading to the delocalized photogeneration of the triplet states. The generation rate constants from the mixed Frenkel and CT excitons to $^1[TT]^a$ and $^1[TT]^b$ are comparable along the *a*- and *b*- axes. In the second step, the rate from $^1[TT]^b$ to T_1^b is twice faster than that from $^1[TT]^a$ to T_1^a, originating from the different nonlocal electron-vibration coupling.

6.6 Summary

In summary, we have presented direct observations of the anisotropic SF in hexacene single crystals. Singlet and triplet DSs indicate strong CT characters for the crystal sites in hexacene. As compared with tetracene, the energy levels of the triplet states are reversed, namely, $E_{T_1^b} < E_{T_1^a}$ with respect to the ground state. Polarized kinetic experiments showed that SF in hexacene is a two-step process, different from the traditional one-step-dominant picture. The anisotropic rates of SF along two crystallographic axes reveal strong dependence on the intermolecular packing. Our findings provide new insights in the SF mechanism for both theory and applications.

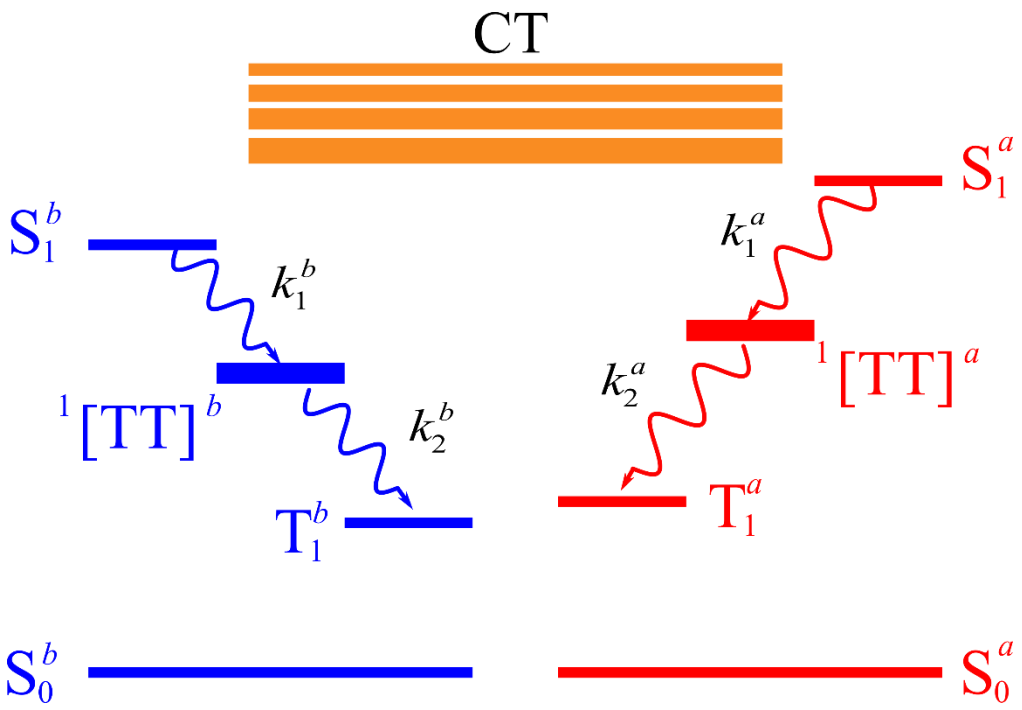

Figure 6.8 Energy diagram for the anisotropic SF in hexacene single crystal. A mixing of Frenkel and CT is excited, orange in color denoting CT contributions. $^1[TT]^a$ and $^1[TT]^b$ represent multiexciton states along the *a*- and *b*- axes. T_1^a and T_1^b are localized triplet states along the *a*- and *b*- axes, with a DS energy of 240 cm^{-1}. The rates k_1 and k_2 along the *a*- and *b*- axes for SF are different, denoted by k_1^a, k_2^a, k_1^b and k_2^b.

6.7 Bibliography

1. Smith, M. B.; Michl, J., Singlet Fission. *Chem. Rev.* **2010,** *110* (11), 6891-6936.
2. Lakowicz, J. R., Principles of Fluorescence Spectroscopy. 2nd ed. ed.; Kluwer Academic/Plenum: New York :, 1999.
3. Piland, G. B.; Burdett, J. J.; Dillon, R. J.; Bardeen, C. J., Singlet Fission: From Coherences to Kinetics. *J. Phys. Chem. Lett.* **2014,** *5* (13), 2312-2319.
4. Busby, E.; Xia, J.; Wu, Q.; Low, J. Z.; Song, R.; Miller, J. R.; Zhu, X. Y.; Campos, L. M.; Sfeir, M. Y., A Design Strategy for Intramolecular Singlet Fission Mediated by Charge-Transfer States in Donor-Acceptor Organic Materials. *Nat. Mater.* **2015,** *14* (4), 426-33.
5. Musser, A. J.; Liebel, M.; Schnedermann, C.; Wende, T.; Kehoe, T. B.; Rao, A.; Kukura, P., Evidence for Conical Intersection Dynamics Mediating Ultrafast Singlet Exciton Fission. *Nat. Phys.* **2015,** *11* (4), 352-357.
6. Chan, W. L.; Ligges, M.; Zhu, X. Y., The Energy Barrier in Singlet Fission Can Be Overcome through Coherent Coupling and Entropic Gain. *Nat. Chem.* **2012,** *4* (10), 840-845.
7. Walker, B. J.; Musser, A. J.; Beljonne, D.; Friend, R. H., Singlet Exciton Fission in Solution. *Nat. Chem.* **2013,** *5* (12), 1019-1024.
8. Chan, W. L.; Ligges, M.; Jailaubekov, A.; Kaake, L.; Miaja-Avila, L.; Zhu, X. Y., Observing the Multiexciton State in Singlet Fission and Ensuing Ultrafast Multielectron Transfer. *Science* **2011,** *334* (6062), 1541-1545.
9. Congreve, D. N.; Lee, J.; Thompson, N. J.; Hontz, E.; Yost, S. R.; Reusswig, P. D.; Bahlke, M. E.; Reineke, S.; Van Voorhis, T.; Baldo, M. A., External Quantum

Efficiency above 100% in a Singlet-Exciton-Fission–Based Organic Photovoltaic Cell. *Science* **2013,** *340* (6130), 334-337.

10. Yost, S. R.; Lee, J.; Wilson, M. W. B.; Wu, T.; McMahon, D. P.; Parkhurst, R. R.; Thompson, N. J.; Congreve, D. N.; Rao, A.; Johnson, K.; Sfeir, M. Y.; Bawendi, M. G.; Swager, T. M.; Friend, R. H.; Baldo, M. A.; Van Voorhis, T., A Transferable Model for Singlet-Fission Kinetics. *Nat. Chem.* **2014,** *6* (6), 492-497.
11. Zimmerman, P. M.; Zhang, Z. Y.; Musgrave, C. B., Singlet Fission in Pentacene through Multi-Exciton Quantum States. *Nat. Chem.* **2010,** *2* (8), 648-652.
12. Tiago, M. L.; Northrup, J. E.; Louie, S. G., Ab Initio Calculation of the Electronic and Optical Properties of Solid Pentacene. *Phys. Rev. B* **2003,** *67* (11), 115212.
13. Zirzlmeier, J.; Lehnherr, D.; Coto, P. B.; Chernick, E. T.; Casillas, R.; Basel, B. S.; Thoss, M.; Tykwinski, R. R.; Guldi, D. M., Singlet Fission in Pentacene Dimers. *Proc. Natl. Acad. Sci. USA* **2015,** *112* (17), 5325-5330.
14. Johnson, J. C.; Nozik, A. J.; Michl, J., High Triplet Yield from Singlet Fission in a Thin Film of 1,3-Diphenylisobenzofuran. *J. Am. Chem. Soc.* **2010,** *132* (46), 16302-16303.
15. Jundt, C.; Klein, G.; Sipp, B.; Lemoigne, J.; Joucla, M.; Villaeys, A. A., Exciton Dynamics in Pentacene Thin Films Studied by Pump-Probe Spectroscopy. *Chem. Phys. Lett.* **1995,** *241* (1-2), 84-88.
16. Busby, E.; Berkelbach, T. C.; Kumar, B.; Chernikov, A.; Zhong, Y.; Hlaing, H.; Zhu, X. Y.; Heinz, T. F.; Hybertsen, M. S.; Sfeir, M. Y.; Reichman, D. R.; Nuckolls, C.; Yaffe, O., Multiphonon Relaxation Slows Singlet Fission in Crystalline Hexacene. *J. Am. Chem. Soc.* **2014,** *136* (30), 10654-10660.

17. Tayebjee, M. J. Y.; Clady, R.; Schmidt, T. W., The Exciton Dynamics in Tetracene Thin Films. *Phys. Chem. Chem. Phys.* **2013,** *15* (35), 14797-14805.

18. Marciniak, H.; Pugliesi, I.; Nickel, B.; Lochbrunner, S., Ultrafast Singlet and Triplet Dynamics in Microcrystalline Pentacene Films. *Phys. Rev. B* **2009,** *79* (23).

19. Merrifield, R. E.; Avakian, P.; Groff, R. P., Fission of Singlet Excitons into Pairs of Triplet Excitons in Tetracene Crystals. *Chem. Phys. Lett.* **1969,** *3* (3), 155-157.

20. Englman, R.; Jortner, J., The Energy Gap Law for Radiationless Transitions in Large Molecules. *Mol. Phys.* **1970,** *18* (2), 145-164.

21. Monahan, N.; Zhu, X. Y., Charge Transfer-Mediated Singlet Fission. *Annu. Rev. Phys. Chem.* **2015,** *66*, 601-18.

22. Kolata, K.; Breuer, T.; Witte, G.; Chatterjee, S., Molecular Packing Determines Singlet Exciton Fission in Organic Semiconductors. *ACS Nano* **2014,** *8* (7), 7377-7383.

23. Wang, L. J.; Olivier, Y.; Prezhdo, O. V.; Beljonne, D., Maximizing Singlet Fission by Intermolecular Packing. *J. Phys. Chem. Lett.* **2014,** *5* (19), 3345-3353.

24. Wu, Y. S.; Liu, K.; Liu, H. Y.; Zhang, Y.; Zhang, H. L.; Yao, J. N.; Fu, H. B., Impact of Intermolecular Distance on Singlet Fission in a Series of Tips Pentacene Compounds. *J. Phys. Chem. Lett.* **2014,** *5* (20), 3451-3455.

25. Reese, C.; Bao, Z., Organic Single-Crystal Field-Effect Transistors. *Mater. Today* **2007,** *10* (3), 20-27.

26. Laudise, R. A.; Kloc, C.; Simpkins, P. G.; Siegrist, T., Physical Vapor Growth of Organic Semiconductors. *J. Cryst. Growth.* **1998,** *187* (3–4), 449-454.

27. Watanabe, M.; Chang, Y. J.; Liu, S.-W.; Chao, T.-H.; Goto, K.; Islam, M. M.; Yuan, C.-H.; Tao, Y.-T.; Shinmyozu, T.; Chow, T. J., The Synthesis, Crystal Structure and Charge-Transport Properties of Hexacene. *Nat. Chem.* **2012,** *4* (7), 574-578.

28. Wilson, M. W. B.; Rao, A.; Ehrler, B.; Friends, R. H., Singlet Exciton Fission in Polycrystalline Pentacene: From Photophysics toward Devices. *Acc. Chem. Res.* **2013,** *46* (6), 1330-1338.

29. Wilson, M. W. B.; Rao, A.; Clark, J.; Kumar, R. S. S.; Brida, D.; Cerullo, G.; Friend, R. H., Ultrafast Dynamics of Exciton Fission in Polycrystalline Pentacene. *J. Am. Chem. Soc.* **2011,** *133* (31), 11830-11833.

30. Wilson, M. W. B.; Rao, A.; Johnson, K.; Gelinas, S.; di Pietro, R.; Clark, J.; Friend, R. H., Temperature-Independent Singlet Exciton Fission in Tetracene. *J. Am. Chem. Soc.* **2013,** *135* (44), 16680-16688.

31. Boyd, R. W., Nonlinear Optics. 3rd ed. ed.; Academic Press: Burlington, MA :, 2008.

32. Faltermeier, D.; Gompf, B.; Dressel, M.; Tripathi, A. K.; Pflaum, J., Optical Properties of Pentacene Thin Films and Single Crystals. *Phys. Rev. B* **2006,** *74* (12).

33. Chernikov, A.; Yaffe, O.; Kumar, B.; Zhong, Y.; Nuckolls, C.; Heinz, T. F., Spectroscopic Study of Anisotropic Excitons in Single Crystal Hexacene. *J. Phys. Chem. Lett.* **2014,** *5* (21), 3632-3635.

34. Yamagata, H.; Norton, J.; Hontz, E.; Olivier, Y.; Beljonne, D.; Bredas, J. L.; Silbey, R. J.; Spano, F. C., The Nature of Singlet Excitons in Oligoacene Molecular Crystals. *J. Chem. Phys.* **2011,** *134* (20), 204703.

35. Schwoerer, H.; Birech, Z. In *Davydov Splitting in Triplet Excitons of Tetracene Single Crystals*, Frontiers in Optics 2014, Tucson, Arizona, 2014/10/19; Optical Society of America: Tucson, Arizona, 2014; p FTu1G.8.

36. Stern, H. L.; Musser, A. J.; Gelinas, S.; Parkinson, P.; Herz, L. M.; Bruzek, M. J.; Anthony, J.; Friend, R. H.; Walker, B. J., Identification of a Triplet Pair Intermediate in Singlet Exciton Fission in Solution. *Proc. Natl. Acad. Sci. USA* **2015,** *112* (25), 7656-7661.

37. Kolomeisky, A. B.; Feng, X. T.; Krylov, A. I., A Simple Kinetic Model for Singlet Fission: A Role of Electronic and Entropic Contributions to Macroscopic Rates. *J. Phys. Chem. C* **2014,** *118* (10), 5188-5195.

38. Birech, Z.; Schwoerer, M.; Schmeiler, T.; Pflaum, J.; Schwoerer, H., Ultrafast Dynamics of Excitons in Tetracene Single Crystals. *J. Chem. Phys.* **2014,** *140* (11), 9.

39. Beljonne, D.; Yamagata, H.; Bredas, J. L.; Spano, F. C.; Olivier, Y., Charge-Transfer Excitations Steer the Davydov Splitting and Mediate Singlet Exciton Fission in Pentacene. *Phys. Rev. Lett.* **2013,** *110* (22), 5.

40. Sebastian, L.; Weiser, G., Charge-Transfer Transitions in Crystalline Anthracene and Their Role in Photoconductivity. *Chem. Phys.* **1983,** *75*, 103-114.

41. Sebastian, L.; Weiser, G.; Bassler, H., Charge Transfer Transitions in Solid Tetracene and Pentacene Studied by Electroabsorption. *Chem. Phys. Lett.* **1981,** *61*, 125-135.

42. Girlando, A.; Grisanti, L.; Masino, M.; Bilotti, I.; Brillante, A.; Della Valle, R. G.; Venuti, E., Peierls and Holstein Carrier-Phonon Coupling in Crystalline Rubrene. *Phys. Rev. B* **2010,** *82* (3), 035208.

CHAPTER 7

CONCLUSIONS AND PERSPECTIVES

7.1 Study of Noble Metal Nanoparticles

In this dissertation, second harmonic scattering (SHS) has been employed to probe the adsorption and reactions of thiol molecules at the surface of silver nanoparticles with 80 nm average diameter. It has been experimentally demonstrated that the free energy change, activation energy as well as adsorption density of the reactions of a variety of neutral and anionic thiols at the particle surface can be measured. The reaction mechanisms at the molecular level have been deduced, and the neutral vs charged thiols have qualitatively different reactions mechanisms that reflect the effect of molecular interactions at the surface.

The same methodology can be applied to other important noble metal nanoparticles. In fact, a few groups have already started using SHS to study gold nanoparticles.[1-4] In contrast to silver nanoparticle, gold nanoparticles with similar particle size has the localized surface plasmon that is red shifted.[5] Therefore, the commonly-used 800 nm Ti-Sapphire laser and its second harmonic light (400 nm) are not in resonance with gold nanoparticles. To overcome this disadvantage, one possible solution is to tune the wavelength of the fundamental light by means of optical parametric oscillator (OPO) or optical parametric amplifier (OPA).[6]

Molecular adsorption and reactions at the interface of colloidal system involves both the dispersing phase (solvent) and the dispersed phase (nanoparticles). In this work, SHS is used to monitor the surface response of silver nanoparticles, namely, the second-

order susceptibility originated from the particle surface. Another scheme for the interfacial study, on the other hand, is to directly monitor the adsobate itself. This can be achieved by using Sum Frequency Scattering (SFS), another second-order nonlinear light scattering technique based on Sum Frequency Generation (SFG). As for SFS, two lasers carrying different frequencies (ω_1 and ω_2) generate the SFS signal whose frequency equals to the sum of ω_1 and ω_2.[7-8] With one of the incident light be resonant to the vibrational mode of the adsobate, resonant SFS signal can be observed. Roke and her coworkers have reported SFS signal from lipid bilayers and emulsions suspended in water.[9-10] The major challenge, however, is the relatively weak signal due to the small second-order susceptibility of alkanethiol molecules. To extend the capability of SFS requires some signal amplification techniques. One of the candidates is the heterodyne detection technology, which has long been applied in the fields of laser spectroscopies and radio technologies.[11-15] An easy-to-implement method of heterodyne SFG was developed in our group that adopted a collinear geometry.[16] The collinear heterodyne SFG has been proved to not only enhance the SFG signal, but also provide the ability to exact the phase information, and therefore can be applicable in the SFS study of nanoparticles.

7.2 Study of Micro-Sized Ultrathin Oligoacene Single Crystals

In this dissertation, micrometer-sized ultrathin oligoacene single crystals, such as pentacene and hexacene, have been chosen as model systems for the studies of excitonic properties as well as the singlet fission mechanism. Due to the small sizes of ultrathin single crystals ($< 100\ \mu m^2$), we modified the regular linear and transient absorption spectroscopies

by combining them with an optical microscope. The dramatic spectral change between isolated molecules and single crystals of pentacene illustrates the effect of molecular interaction upon crystallization. The anisotropic spectral features also uncover the dependence of the excitons (Frenkel/CT) compositions on the molecular ordering along different crystallographic axes. With respect to the crystalline hexacene, polarized transient absorption spectra demonstrate that both singlet and triplet excitons are manipulated by the strong CT characters which lead to the Davydov splittings. In addition, a two-step mechanism of singlet fission has been directly observed in the polarized kinetic experiment of hexacene single crystals. The fact that singlet fission occurs at different rates along two crystallographic axes indicates strong dependence on the intermolecular packing, in agreement with the linear absorption results of crystalline pentacene.

It has to be noticed that pentacene is also intensively studied for singlet fission.[17-21] Further investigation can be conducted by performing transient absorption measurement on pentacene single crystals. Compared to hexacene single crystals in which the lowest excitation states along two axes can be both excited by the 800 nm pump light, as for pentacene, the pumping wavelength need to be adjusted to 627 nm and 672 nm, respectively. This can be achieved by introducing another laser beam from a femtosecond OPA to the current microscopic transient absorption setup.

7.3 Bibliography

1. Haber, L. H.; Kwok, S. J. J.; Semeraro, M.; Eisenthal, K. B., Probing the Colloidal Gold Nanoparticle/Aqueous Interface with Second Harmonic Generation. *Chem. Phys. Lett.* **2011,** *507* (1-3), 11-14.
2. Karam, T. E.; Haber, L. H., Molecular Adsorption and Resonance Coupling at the Colloidal Gold Nanoparticle Interface. *J. Phys. Chem. C* **2014,** *118* (1), 642-649.
3. Kumal, R. R.; Landry, C. R.; Abu-Laban, M.; Hayes, D. J.; Haber, L. H., Monitoring the Photocleaving Dynamics of Colloidal Microrna-Functionalized Gold Nanoparticles Using Second Harmonic Generation. *Langmuir* **2015,** *31* (36), 9983-9990.
4. Capretti, A.; Pecora, E. F.; Forestiere, C.; Dal Negro, L.; Miano, G., Size-Dependent Second-Harmonic Generation from Gold Nanoparticles. *Phys. Rev. B* **2014,** *89* (12).
5. Mayer, K. M.; Hafner, J. H., Localized Surface Plasmon Resonance Sensors. *Chem. Rev.* **2011,** *111* (6), 3828-3857.
6. Cerullo, G.; De Silvestri, S., Ultrafast Optical Parametric Amplifiers. *Rev. Sci. Instrum.* **2003,** *74* (1), 1-18.
7. Boyd, R. W., Nonlinear Optics. 3rd ed. ed.; Academic Press: Burlington, MA :, 2008.
8. Shen, Y. R., The Principles of Nonlinear Optics. Wiley: New York :, 1984.
9. Roke, S.; Gonella, G., Nonlinear Light Scattering and Spectroscopy of Particles and Droplets in Liquids. *Annu. Rev. Phys. Chem.* **2012,** *63*, 353-378.

10. Samson, J. S.; Scheu, R.; Smolentsev, N.; Rick, S. W.; Roke, S., Sum Frequency Spectroscopy of the Hydrophobic Nanodroplet/Water Interface: Absence of Hydroxyl Ion and Dangling Oh Bond Signatures. *Chem. Phys. Lett.* **2014,** *615*, 124-131.

11. Brunner, F. D. J.; Johnson, J. A.; Grubel, S.; Ferrer, A.; Johnson, S. L.; Feurer, T., Distortion-Free Enhancement of Terahertz Signals Measured by Electro-Optic Sampling. I. Theory. *J. Opt. Soc. Am. B* **2014,** *31* (4), 904-910.

12. Griffith, J. A. R., Laser Heterodyne Spectroscopy. *Phil. Trans. R. Soc. A* **1982,** *307* (1500), 563-571.

13. Horowitz, P., The Art of Electronics. Third edition. ed.; Hill, W., Ed.

14. Veenstra, K. J.; Petukhov, A. V.; de Boer, A. P.; Rasing, T., Phase-Sensitive Detection Technique for Surface Nonlinear Optics. *Phys. Rev. B* **1998,** *58* (24), 16020-16023.

15. Wilson, P. T.; Jiang, Y.; Carriles, R.; Downer, M. C., Second-Harmonic Amplitude and Phase Spectroscopy by Use of Broad-Bandwidth Femtosecond Pulses. *J. Opt. Soc. Am. B* **2003,** *20* (12), 2548-2561.

16. Xu, B. L.; Wu, Y. J.; Sun, D. Z.; Dai, H. L.; Rao, Y., Stabilized Phase Detection of Heterodyne Sum Frequency Generation for Interfacial Studies. *Opt. Lett.* **2015,** *40* (19), 4472-4475.

17. Berkelbach, T. C.; Hybertsen, M. S.; Reichman, D. R., Microscopic Theory of Singlet Exciton Fission. Iii. Crystalline Pentacene. *J. Chem. Phys.* **2014,** *141* (7).

18. Smith, M. B.; Michl, J., Singlet Fission. *Chem. Rev.* **2010,** *110* (11), 6891-6936.

19. Wilson, M. W. B.; Rao, A.; Ehrler, B.; Friends, R. H., Singlet Exciton Fission in Polycrystalline Pentacene: From Photophysics toward Devices. *Acc. Chem. Res.* **2013,** *46* (6), 1330-1338.

20. Zimmerman, P. M.; Bell, F.; Casanova, D.; Head-Gordon, M., Mechanism for Singlet Fission in Pentacene and Tetracene: From Single Exciton to Two Triplets. *J. Am. Chem. Soc.* **2011,** *133* (49), 19944-19952.

21. Zirzlmeier, J.; Lehnherr, D.; Coto, P. B.; Chernick, E. T.; Casillas, R.; Basel, B. S.; Thoss, M.; Tykwinski, R. R.; Guldi, D. M., Singlet Fission in Pentacene Dimers. *Proc. Natl. Acad. Sci. USA* **2015,** *112* (17), 5325-5330.

APPENDIX A

ESTIMATION OF THE PHOTOEXCITED CARRIER DENSITY

The photoexcited carrier density can be estimated as follows:

(a) By using a known extinction coefficient for hexacene at 730 nm (0.25×10^5 cm^{-1}), the crystal thickness can be calculated:

$$l = \frac{-\log(T)}{\alpha} = \frac{\log(20)}{0.25\times10^5} = 5.2\times10^{-5}\text{cm} = 520\text{nm}$$

(b) For 0.58 μW 800 nm femtosecond laser pulse with focus spot radius 4.5 μm, laser fluence is,

$$\frac{\text{Pulse Energy}}{\text{Spot Size}} = \frac{0.58\times10^{-3}}{\pi\cdot(4.5\times10^{-4})^2} = 170\,\mu\text{J/cm}^2$$

(c) Excitation volume is,

$$V_{ext} = \text{Area}\cdot\text{Thickness} = \pi\cdot(4.5)^2\cdot0.52 = 33\,\mu\text{m}^3$$

(d) The number of photons per volume is given by pulse energy/photon energy/volume, i.e.

$$\frac{0.58\times10^{-6}}{10^3}\cdot(0.12\times10^5\cdot5.2\times10^{-5})\cdot\frac{1}{1240/800\cdot1.6\times10^{-19}}\cdot\frac{1}{\pi\cdot(4.5\times10^{-4})^2\cdot5.2\times10^{-5}}$$
$$= 8.0\times10^{18}\text{cm}^{-3}$$

(e) Assuming that each absorbed photon generates one singlet exciton, the initial singlet exciton density is 8.0×10^{18} cm^{-3}.

(f) Volume of hexacene is,

a=7.673 Å, b=6.292 Å, c=16.242 Å

$V = abc = 784.13\text{Å}^3$

Since there are two molecules in a unit cell, the volume of each molecule is 392.06 Å^3

(g) The ratio of excited molecule density vs. total molecule density is,

$$\frac{D_{ext}}{D_{tot}} = \frac{8.0\times10^{-6}}{1/392.06} = 3.1\times10^{-3}$$

(h) The expected pump probe signal ($\frac{\Delta T}{T}$) without considering singlet fission is,

$$\frac{\Delta T}{T} = \frac{\alpha(\lambda)\cdot l\cdot N}{N_0} = 1\cdot 3.1\times10^{-3} = 3.1\times10^{-3}$$

APPENDIX B

FITTING METHODS FOR KINETICS OF SINGLET FISSION

B.1 Kinetics Model

Singlet fission along one axis (*a* or *b*) is a sequential bimolecular reaction:

$$S_0 + S_1 \xrightarrow{k_1} {}^1[TT] \xrightarrow{k_2} T_1 + T_1 \tag{B1}$$

in which k_1 is the rate constant of the formation of $^1[TT]$ state, and k_2 is the dissociation rate of $^1[TT]$ state. Assuming the population of S_0 is constant, the coupled differential equations will be,

$$\begin{cases} \dfrac{dS_1}{dt} = -k_1 S_1 \\ \dfrac{d\,{}^1[TT]}{dt} = k_1 S_1 - k_2\,{}^1[TT] \\ \dfrac{dT_1}{dt} = 2k_2\,{}^1[TT] \end{cases} \tag{B2}$$

Solving Eq. B2 gives the population dynamics for the singlet, triplet excitons and $^1[TT]$ as,

$$\begin{cases} S_1(t) = A_0 e^{-k_1 t} \\ {}^1[TT](t) = \dfrac{k_1 A_0}{k_1 - k_2}(e^{-k_1 t} - e^{-k_2 t}) \\ T_1(t) = A_0\left(1 + \dfrac{1}{k_1 - k_2}(k_2 e^{-k_1 t} - k_1 e^{-k_2 t})\right) \end{cases} \tag{B3}$$

B.2 Spectrotemporal Model

The observable in transient absorption measurement is proportional to their absorption cross sections σ_{i} as functions of wavelength λ, as well as to the population of each species N_i as functions of delay *t*, where *i*=S_0, S_1, and T_1, respectively.

$$\begin{cases} \dfrac{\Delta T}{T}(\mathrm{S_1}-\mathrm{S_n}) = -\sigma_{\mathrm{S_1}}(\lambda)\cdot N_{\mathrm{S_1}}(t) \\ \dfrac{\Delta T}{T}(\mathrm{T_1}-\mathrm{T_n}) = -\sigma_{\mathrm{T_1}}(\lambda)\cdot N_{\mathrm{T_1}}(t) \\ \dfrac{\Delta T}{T}(\mathrm{S_0}-\mathrm{S_1}) = \sigma_{\mathrm{S_0}}(\lambda)\cdot \Delta N_{\mathrm{S_0}}(t) = \sigma_{\mathrm{S_0}}(\lambda)\cdot (N_{\mathrm{S_0}}(t) - N_{\mathrm{S_0}}(0)) \end{cases} \quad \text{(B4)}$$

As a molecule can only be at one of the states, S_0, S_1, and T_1, the population of all species follows,

$$\Delta N_{\mathrm{S_0}}(t) = N_{\mathrm{S_1}}(t) + N_{\mathrm{T_1}}(t) \quad \text{(B5)}$$

B.3 Analytical Solution for Global Fitting

Combining Eq. B3 and B4, we are able to apply global fittings to our transient absorption data as functions of temporal delays. Since the time-dependent spectra for the three transitions are highly overlapped, we here treat any spectral region as a mixture of singlet and triplet excitons. This is valid based on Eq. B5, in which ground state bleach (GSB) can be decoupled into a combination of the temporal profiles of singlet and triplet excitons.

An analytical fitting function was used for global fittings in Igor Pro (WaveMetrics), that is,

$$\frac{\Delta T}{T} = \frac{Erf(c1\cdot(t-c2))+1}{2}\cdot c3\cdot e^{-k_1 t} + c4\cdot\left(1+\frac{1}{k_1-k_2}(k_2 e^{-k_1 t} - k_1 e^{-k_2 t})\right) \quad \text{(B6)}$$

where an error function, *Erf*(), is applied to estimate the instrumental response function (IRF), $c1$ is the pulse duration of pump pulse, $c2$ is the temporal error induced by chirp correction, and $c3$ as well as $c4$ respond to the cross sections of singlet and triplet excitons mixed with GSB contributions, respectively.

APPENDIX C

ESTIMATION OF CT EXCITON BINDING ENERGY AND CONTRIBUTION

C.1 Estimation of CT Exciton Binding Energy and Percentage of CT Contribution in Singlet Exciton for Hexacene Single Crytal.

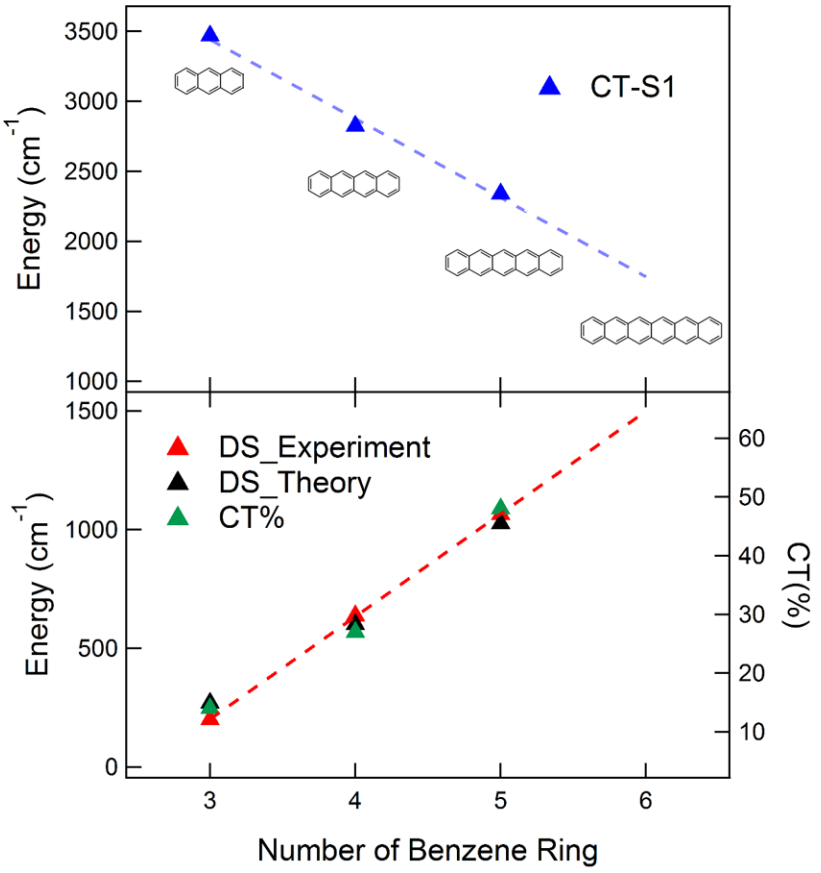

Figure C.1 (upper) Energy difference between CT and S_1 for different oligoacene single crystals. The data were retrieved from the literatures.[1-2] (lower) Comparisons of the experimental measurements (red) and the theoretical calculations (black) for Davydov splitting (DS) in different oligoacene single crystals. The right y axis corresponds to the percentage of the CT character (green) in the singlet exciton based on the theoretical calculations from the literatures.[3-4] The dash line is an empirical linear fit for better reading.

C.2 Bibliography

1. Sebastian, L.; Weiser, G., Charge-Transfer Transitions in Crystalline Anthracene and Their Role in Photoconductivity. *Chem. Phys.* **1983,** *75*, 103-114.
2. Sebastian, L.; Weiser, G.; Bassler, H., Charge Transfer Transitions in Solid Tetracene and Pentacene Studied by Electroabsorption. *Chem. Phys. Lett.* **1981,** *61*, 125-135.
3. Beljonne, D.; Yamagata, H.; Bredas, J. L.; Spano, F. C.; Olivier, Y., Charge-Transfer Excitations Steer the Davydov Splitting and Mediate Singlet Exciton Fission in Pentacene. *Phys. Rev. Lett.* **2013,** *110* (22), 5.
4. Yamagata, H.; Norton, J.; Hontz, E.; Olivier, Y.; Beljonne, D.; Bredas, J. L.; Silbey, R. J.; Spano, F. C., The Nature of Singlet Excitons in Oligoacene Molecular Crystals. *J. Chem. Phys.* **2011,** *134* (20), 204703.